The Dissertation Committee for Isaac G. Boxx Certifies that this is the approved version of the following dissertation:

THE EFFECTS OF BUOYANCY ON TURBULENT NONPREMIXED JET FLAMES IN CROSSFLOW

Committee:

Noel T. Clemens, Supervisor

David S. Dolling

Ofodike A. Ezekoye

Laxminarayan L. Raja

Philip L. Varghese

THE EFFECTS OF BUOYANCY ON TURBULENT NONPREMIXED JET FLAMES IN CROSSFLOW

by

Isaac G. Boxx, B.S.E.

Dissertation

Presented to the Faculty of the Graduate School of
The University of Texas at Austin
in Partial Fulfillment
of the Requirements
for the Degree of

Doctor of Philosophy

The University of Texas at Austin
May, 2005

Dedication

To Esther

Acknowledgements

It is with great pleasure that I acknowledge the contributions and support of all those who helped make this work possible. I extend heartfelt appreciation to my advisor, Dr. Noel T. Clemens for his efforts to guide and direct my labors in this effort and for his ability to obtain the resources needed to make the University of Texas Drop Tower Facility all that it turned out to be. I thank my former colleague Cherian A. Idicheria for his important contributions to the design of the drop-rig computer and pressurized gas system and his many helpful comments on the design of the fiber-optic system. I acknowledge the input of Dr. Zengguan Yaun, of the staff of the NASA Goddard Research Center in overseeing this project. The funding provided by the NASA Microgravity Sciences Division is also gratefully acknowledged. I am deeply indebted to my colleague Mirko Gamba for his extensive assistance in running the experiments during the crucial final phase of the project. I also thank my (current and former) fellow graduate students Pablo Bueno, Michael Ryan, Michael Tsurikov, Yongxi Hou, Prashanth Kothnur and Guanghua Wang for their numerous insights, suggestions and moral support. Many thanks to my dear old friends Dilum, Kristi, Ken and Bobbi and to my family for all their support during the five and a half years of my graduate student career. Finally, my deepest thanks to Lizz for helping me get through the hard times.

THE EFFECTS OF BUOYANCY ON TURBULENT NONPREMIXED JET FLAMES IN CROSSFLOW

Publication No._____________

Isaac G. Boxx, Ph.D.
The University of Texas at Austin, 2005

Supervisor: Noel T. Clemens

An experimental research study was conducted to investigate what effect buoyancy had on the mean and instantaneous flow-field characteristics of turbulent jet-flames in crossflow (JFICF). The study used an experimental technique wherein a series of normal-gravity, hydrogen-diluted propane JFICF were compared with otherwise identical ones in low-gravity. Experiments were conducted at the University of Texas Drop Tower Facility, a new microgravity science laboratory built for this study at the University of Texas at Austin. Two different diagnostic techniques were employed, high frame-rate digital cinematographic imaging and planar laser Mie scattering (PLMS).

The flame-luminosity imaging revealed significant elongation and distortion of the large-scale luminous structure of the JFICF. This was seen to affect the flametip oscillation and burnout characteristics. Mean and root-mean-square (RMS) images of flame-luminosity were computed from the flame-luminosity image sequences. These were used to compare visible flame-shapes, flame chord-lengths and jet centerline-trajectories of the normal- and low-gravity flames. In all cases the jet-centerline

penetration and mean luminous flame-width were seen to increase with decreasing buoyancy. The jet-centerline trajectories for the normal-gravity flames were seen to behave differently to those of the low-gravity flames. This difference led to the conclusion that the jet transitions from a momentum-dominated forced convection limit to a buoyancy-influenced regime when it reaches $\xi_C \approx 3$, where ξ_C is the Becker and Yamazaki (1978) buoyancy parameter based on local flame chord-length. The mean luminous flame-lengths showed little sensitivity to buoyancy or momentum flux ratio.

Consistent with the flame-luminosity imaging experiments, comparison of the instantaneous PLMS flow-visualization images revealed substantial buoyancy-induced elongation and distortion of the large-scale shear-layer vortices in the flow. This effect became apparent in the JFICF at around $\xi_y = 3.1$ and grew in influence to become a dominant flow-field characteristic approximately $\xi_y = 4.3$. The PLMS images also yielded physical-insight into the nature of the fore-aft asymmetry of JFICF characteristics noted by previous researchers.

Ensemble-averages of PLMS images were used to investigate centerline mixture fraction decay. Consistent with previous studies of non-reacting JICF studies, the mixture-fraction of the JFICF showed a power-law decay profile which scaled with $(rd)^{-0.66}$. Over the region these measurements were made ($\xi_y = 0 - 1.9$), the mixture fraction decay scaling showed little sensitivity to buoyancy.

Taken as a whole, these measurements show that buoyancy has the potential to significantly modify both the mean and instantaneous flow-field of a turbulent JFICF, even at relatively modest length-scales.

Table of Contents

List of Tables

List of Figures

NOMENCLATURE

Roman Symbols

A_{cs}	Cross-sectional area of jet
C	Concentration of jet-fluid
C_0	Concentration of jet-fluid at initial location
d	Jet-exit diameter
d_p	Seed-particle diameter
D_s	Round jet source diameter
D^+	Round jet extended momentum diameter
F_B	Buoyant force
F_x	Force in the x-direction
F_y	Force in the y-direction
Fr_j	Froude number
g	Gravity
I	Measured Mie scattering signal
I_0	Measured Mie scattering signal at jet-exit
Kn	Knudsen number
L	Visible flame length
L_t	Thermal flame length
$\dot{m}$	Mass flux
$\dot{m}_e$	Mass flux of entrained fluid
$\dot{m}_{out}$	Mass flux of fluid across exit plane of control volume
$\dot{m}_0$	Mass flux at jet-exit
M_x	Momentum flux in the x-direction
M_y	Momentum flux in the y-direction
M_0	Molecular mass of jet-fluid
M_∞	Molecular mass of ambient fluid
r	Momentum flux ratio
R	Velocity ratio
Re	Reynolds number
Re_δ	Local Reynolds number
S	Downstream distance in curvilinear coordinates
St	Stokes number
T	Temperature
u_c	Centerline velocity
u_{cf}	Crossflow velocity
u_j	Jet-exit velocity
u_x	x-component of velocity
u_y	y-component of velocity
x	Axis aligned with initial jet direction
y	Axis aligned with initial crossflow direction
z	Axis perpendicular to xy plane

Greek Symbols

δ	Local jet full-width
$\delta_{1/2}$	Local jet half-width at half-maximum velocity
δ_j	Initial jet-penetration angle
λ	Mean free path
ρ	Fluid density
ρ_{cf}	Crossflow fluid density
(ρ_{eff})	Effective fluid density
ρ_j	Jet-fluid density
ρ_p	Seed-particle density
τ_p	Particle stop time
τ_f	Large scale flow time
μ	Dynamic viscosity
υ	Kinematic viscosity
ζ	Mixture fraction along jet-centerline
$\mathrm{\zeta}$	Coordinate perpendicular to ξ-η plane
η	Radial coordinate
ξ	Buoyancy parameter
$\mathrm{\xi}$	Coordinate aligned with jet-centerline
ξ_c	Buoyancy parameter based on flame chord length
ξ_L	Buoyancy parameter based on visible flame length
ξ_y	Buoyancy parameter based on distance in y-direction
ξ_s	Buoyancy paremeter based on curvilinear distance
χ	Jet-fluid mole fraction

Chapter One: INTRODUCTION

MOTIVATION

Combustion of hydrocarbon fuels is among the most important chemical processes in use today. Hydrocarbon combustion drives our cars, trucks, ships and airplanes. It heats our homes and drives our electric generators. It is also generates some of society's most vexing problems. For example, hydrocarbon combustion is associated with the production of nitric-oxide emissions, which cause human health problems when breathed and contribute to ozone depletion in the upper atmosphere. Particulate emission or "soot" poses a serious health and environment hazard in cities. The massive emission of the greenhouse gas CO_2 caused by fossil fuel combustion is fundamentally altering the global atmosphere and perhaps warming the earth. A thorough understanding of hydrocarbon combustion is essential if we are to efficiently and responsibly utilize it.

Gaseous combustion takes place in one of a variety of ways. It may be premixed, wherein all the fuel and oxidizer are mixed at a molecular level prior to chemical reaction. This sort of combustion is intrinsically dangerous and prone to uncontrolled reaction and explosions. A safer combustion mode is non-premixed, i.e. the fuel and oxidizer are initially unmixed and the reaction only takes place in areas near the interface where diffusion has mixed the reactants at a molecular level. Separating the fuel and oxidizer in this manner results in a safer combustion system but one limited by the rate at which the two gases diffuse into one another. One common way to overcome this bottleneck is to induce turbulent mixing of the fuel and oxidizer.

One common method of accomplishing this is to inject a jet of fuel into a crossflowing stream of oxidizer. The jet-in-crossflow (JICF) has long been known to be a more efficient mixer than a free jet (Bosanquet *et al.*, 1936, Broadwell and Briedenthal, 1984). Unfortunately, this fuel injection technique also has the effect of increasing the complexity of the fluid dynamics and by extension, the design and analysis of the combustor. A thorough fundamental understanding of the JICF is essential to realize its full potential as a mixer and thereby maximize the efficiency and minimize the pollutant emissions of combustors which employ them.

The JICF is also a canonical flowfield, serving as a simplified model for a wide range of applications and as such, has been the focus of a great deal of research. Theoretical studies of a JICF appeared as early at 1936, when Bosanquet *et al*. (1936) developed a model based on dimensional analysis for the diffusion of smoke from chimneys. The 1950s, 60s and 70s saw extensive research on the JICF for military applications such as vertical/short takeoff and landing aircraft, control jet rockets and missile applications. Environmental JICF research for such applications as smokestack dispersion, volcano plumes and suboceanic effluent discharge also continued during this period. An excellent review of the literature for this period may be found in Margason (1993). The JICF has been studied extensively in relation to gas turbine engines, both as a means of cooling combustors (Kamotani and Greber, 1972) and as fuel injection systems (Schluter and Schonfeld, 2000). The oil industry has conducted extensive research on jet-flames in crossflow (JFICF) as a result of its "flaring" unwanted gas leftover from oil production (Brzustowski, 1976).

Although a great deal of research has focused on unraveling the complexities of both the JICF and hydrocarbon combustion, much remains to be done. As will be shown later, one area which remains poorly understood is the effect of buoyancy on the large-scale structure of the jet-flame in crossflow (JFICF) and how it affects such parameters as mixing and entrainment. This is largely due to previous researchers inability to isolate buoyancy effects in a JFICF without a simultaneous alteration of other parameters of the system. The objective of the research study presented in this dissertation was to, for the first time, experimentally isolate and investigate buoyancy effects in turbulent hydrogen JFICF. A secondary objective was to develop and advance the state of the art in high frame-rate planar laser flow-field diagnostics for use in microgravity drop-towers.

LITERATURE REVIEW

The JICF has been the focus of extensive research over the past century. Numerous theoretical, computational and experimental studies have yielded extensive insight on the characteristics of the JICF (Margason, 1993). The following literature survey is broken down into two categories. The first section focuses on the trajectory of a JICF, i.e. the path the jet takes as it penetrates the crossflow. The second section will focus on the topology of the JICF.

Figure 1.1 shows the coordinate system used in this study. The jet-exit is aligned with the x-axis. The initial crossflow-direction is aligned with the y-axis. u_{cf} is the velocity of the crossflow fluid. u_j is the jet-exit velocity.

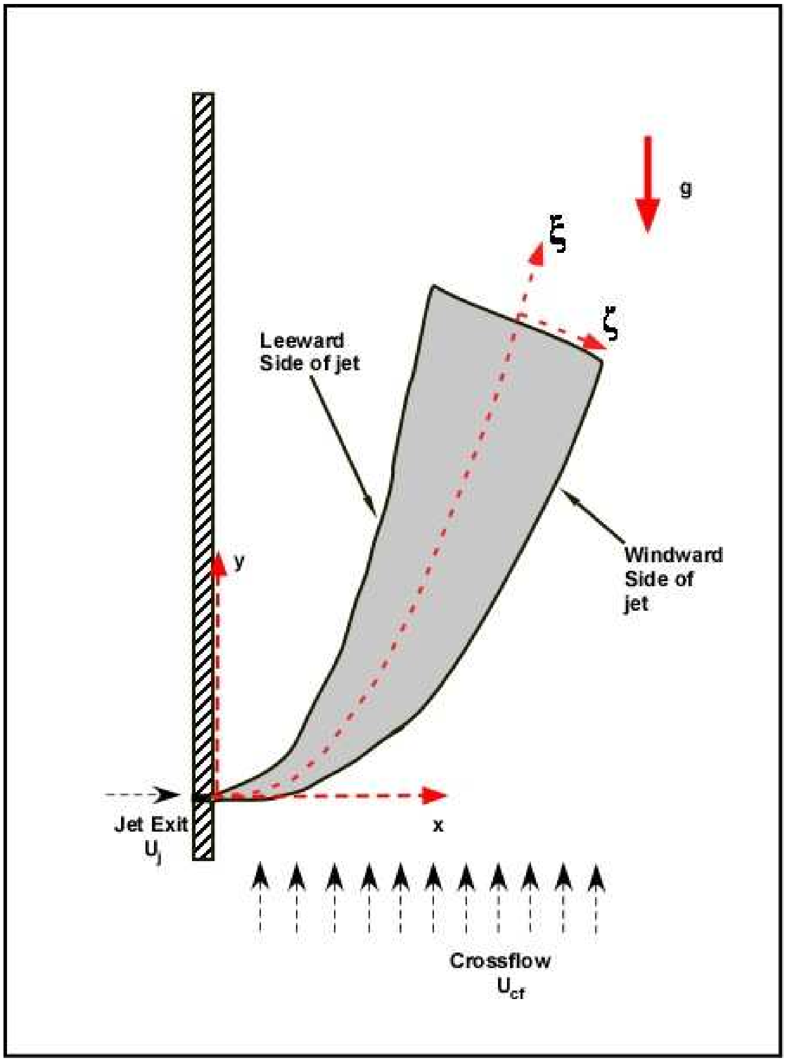

Figure 1.1 Coordinate system used in this study

Trajectories - JICF

One feature of considerable interest in JICF research is the trajectory of the jet as it penetrates into the crossflow. Keffer and Baines (1963) defined the centerline of the JICF as the locus of points where the velocity is a maximum and used this as the basis of a “natural” coordinate system that was used to derive a simplified set of mass and momentum balance equations. Using dimensional analysis, Pratte and Baines (1967) proposed that the trajectory of a JICF (air-jet in air crossflow) follows the general form

$$\frac{x}{rd} = f\left(\frac{y}{rd}\right)$$

where r (the momentum flux ratio) is defined as

$$r = \sqrt{\frac{\rho_j u_j^2}{\rho_{cf} u_{cf}^2}}$$

and ρ_j and ρ_{cf} are the densities of the jet and the crossflow respectively. The momentum flux ratio simplifies to the velocity ratio for fluids of equal density.

One published centerline trajectory correlation (Margason, 1993) takes the form

$$\frac{y}{d} = F\left(\frac{1}{r}\right)^n \left(\frac{x}{d}\right)^m + \frac{x}{d} G \cot\left(\delta_j\right)$$

where δ_j is the angle of the jet with respect to the crossflow. For jets entering a crossflow perpendicularly (i.e. with $\delta_j = 90^0$), studies have reported (Margason, 1993) $0.85<n<3.18$, $1.58<m<3.3$. This correlation reduces to the previous form for cases where $\delta_j = 90^0$. For such cases (including each study described below) the correlation of Pratte and Baines (1967) is the standard form used in the literature.

One reason for the broad spread in the measured power-law exponents is the fact that the JICF trajectory is now known to have not one but two distinct scalings. Using flow visualization (photography of an aerosol oil fog seeded into a jet issuing from an orifice mounted flush with a flat plate into a wind tunnel flow), Pratte and Baines (1967) obtained the power-law correlation for the jet centerline trajectory,

$$\frac{x}{rd} = 2.05\left(\frac{y}{rd}\right)^{0.28}$$

This result was closely matched by Smith and Mungal (1998) who used acetone PLIF to find a max-concentration centerline trajectory of the same form, with an exponent of 0.28 and multiplicative factor of 1.5. However, when plotting centerline penetration along the "natural" coordinate system (ξ,η,ζ) defined by Keffer and Baines (1963), Pratte and Baines observed near-field and far-field regimes wherein the jet centerline trajectory followed a linear and power-law scaling, respectively. Their correlation was as follows

$$\begin{aligned} \frac{x}{rd} &= \left(\frac{\xi}{rd}\right) \qquad && for \qquad \frac{\xi}{rd} \le 2 \\ \frac{x}{rd} &= 1.63\left(\frac{\xi}{rd}\right)^{\frac{1}{3}} \qquad && for \qquad \frac{\xi}{rd} \ge 2 \end{aligned}$$

Although the two regimes are more clearly identifiable when the centerline data are plotted in the natural coordinate system defined by Keffer and Baines (1963), they are also apparent in data plotted in (*x,y,z*) coordinates. Huang and Chang (1994), confirmed this dual power-law scaling behavior using long-time exposure schlieren photographs of a non-reacting, propane JICF to obtain a centerline scalar trajectory power-law correlation of

$$\frac{x}{rd} = 0.65\left(\frac{y}{rd}\right)^{0.33} \qquad for \qquad \frac{y}{rd} \geq 2$$

$$\frac{x}{rd} = 0.66\left(\frac{y}{rd}\right)^{0.61} \qquad for \qquad \frac{y}{rd} \leq 2$$

Rao and Brzustowski (1982) used trace amounts of SO_2 as a molecular marker to study turbulent JICF and found far-field centerline correlation (based on concentration) of

$$\frac{x}{rd} = 1.74\left(\frac{\xi}{rd}\right)^{0.31} \qquad with \qquad \frac{y}{rd} \geq 2$$

confirming again the far-field behavior of a non-reacting JICF.

Besides the observation that there are two regions with different scaling laws, another reason for the spread in exponent-values in these correlations is the difference in the definition of the centerline trajectory. For example, whereas the previously mentioned studies used concentration data to obtain jet trajectory correlations, others use the locus of maximum velocity (Kamotani and Greber,1972) or the center streamline (Hasselbrink, 1999). These trajectories, while similar in form, do not overlap. Kamotani and Greber (1972) found that trajectories based on the locus of maximum velocity penetrate deeper than those based on the concentration profile (in the same flow).

Trajectory - JFICF

The presence of a flame has been seen to alter the trajectory of a JICF. Kadota *et al*. (1990) observed the presence of combustion consistently reduced the deflection of a turbulent propane jet in a uniform crossflow; i.e. the presence of the flame increased the penetration of the JICF. This observation was confirmed by Huang and Chang (1994) and Hasselbrink (1999).

The presence of a flame does not appear to change the basic power-law form of the jet trajectory but it does change the magnitude of the exponent. Rao and Brzustowski (1982) found the power-law exponent in the JFICF trajectory scaling is strongly coupled to the jet-exit Froude number. Brzustowski *et al*. (1975) used long-time (3 sec) exposure photographs to find the centerline of a turbulent hydrogen jet-flame issuing from a tube into a uniform crossflow and obtained the far-field correlation

$$\frac{x}{rd} = 2.05\left(\frac{y}{rd}\right)^{0.28}$$

Huang and Chang (1994) found a correlation of

$$\frac{x}{rd} = 1.07\left(\frac{y}{rd}\right)^{0.21} \qquad for \qquad \frac{y}{rd} \geq 2$$

$$\frac{x}{rd} = 0.86\left(\frac{y}{rd}\right)^{0.37} \qquad for \qquad \frac{y}{rd} \leq 2$$

for a propane JFICF based on a centerline density profile defined on long-exposure schlieren photographs.

Topology of JICF

Figures 1.2 and 1.3 illustrate the basic topology of a JICF. The flowfield is marked by a set of four interacting vortex systems. Dominant among these is the counter-rotating vortex pair, which forms within the core of the JICF. A horseshoe vortex system forms at the interface of the jet and the crossflowing stream and folds around the jet. Shear layer vortices develop on the windward and leeward side of the jet and wake vortices form in region behind the jet. Each of these vortex systems have been extensively studied, both individually and in relation to each other. The following section will provide a brief introduction/overview of each vortex system, their characteristics and the current state of understanding about them.

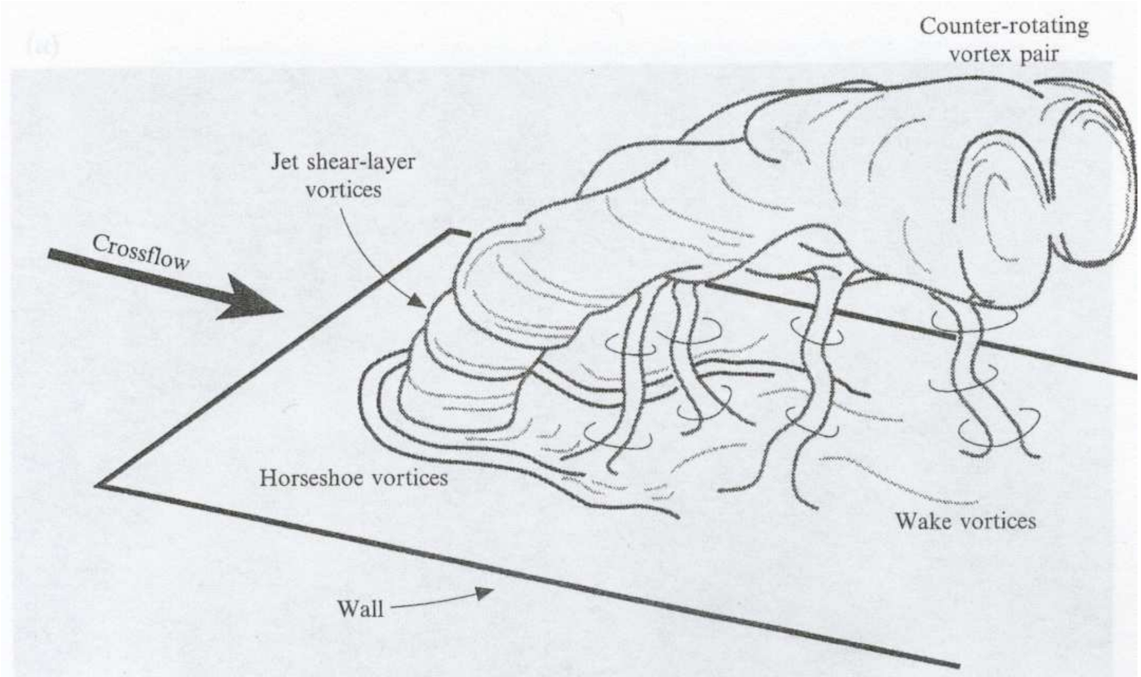

Figure 1.2 – Topology of the JICF. (Fric and Roshko, 1994), Reproduced with permission of the publisher.

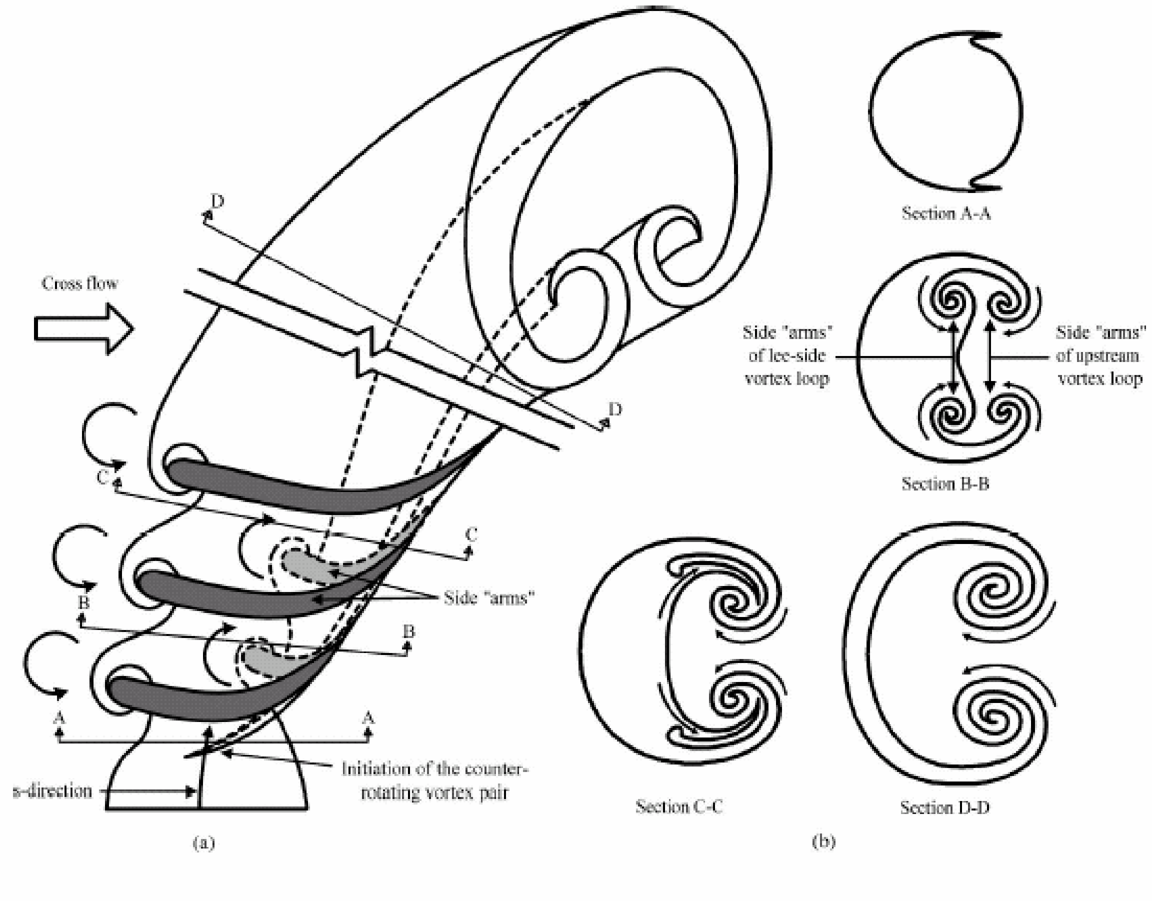

Figure 1.3 – Detailed diagram of the shear-layer loop-vortices of the JICF. Reproduced from Lim *et al*. (2001) with permission of the publisher.

Counter-rotating Vortex Pair

The dominant vortex system in the JICF is the counter-rotating vortex pair (CVP), which forms in the core of the jet as it penetrates the crossflow. As can be seen from Figure 1.2, viewed in the plane perpendicular to the jet trajectory, the CVP appears kidney-shaped. It exhibits two lobes that grow in diameter with downstream distance. The CVP is commonly assumed to be symmetric about the z-axis.

Owing to its dominance of the far-field structure of the JICF and the extensive experimental data available on this region, the CVP has been the focus of a great deal of theoretical work. Such models have yielded significant insight into such phenomena as vortex trajectory and core half-spacing (Karagozian, 1986) and vortex-strength and mixing (LeGrives, 1978).

The origin of the CVP has received much less attention and is an area of current research. Its origins have been conclusively linked with the near field of the JICF. Yuan *et al*. (1999) contend that the origin of the CVP is a pair of quasi-steady ‘hanging’ vortices which form in the skewed mixing layer that develops between the jet and crossflow fluid on the lateral edges of the jet. This is consistent with the observations of Kelso *et al*. (1996) and Lim *et al*. (2001).

Shear Layer Vortices

The penetration of a circular jet into a uniform crossflowing stream creates a cylindrical shear-layer. The cylindrical shear-layer induces a Kelvin-Helmholtz instability, which in turn leads to the formation of a series of vortices near the base of the

JICF. These shed periodically and move downstream with the JICF, contributing to the mixing and entrainment of the system.

The shear-layer vortex of a JICF system has been extensively studied and remains an area of active research. Until recently, the shear-layer vortex was thought to consist of ring vortices, which form around the perimeter of the JICF and then bend and fold into vortex loops as they propagate downstream (Andreopoulos, 1985, Sykes *et al*., 1986, Kelso *et al*., 1996). More recently however, researchers (Yuan *et al*., 1999, Lim *et al*., 2000) have shown both experimentally and computationally that that the shear-layer vortices actually form as two rows of loop vortices, without the intermediate formation (and subsequent deformation) of ring vortices. As shown in Figure 1.3, these loop vortices form on the windward side and leeward side of the jet and are rolled up into the CVP as they move downstream. Yuan et al. (1999) contend that axial flow through these loop vortices sweeps vortical fluid from the near-wall region of the incoming jet-fluid to the back side of the jet and leads to the formation of the CVP.

Horseshoe Vortices

The penetration of a jet into a uniform crossflowing stream induces a region of boundary layer separation upstream of the jet-exit, resulting in a "horseshoe" or "necklace" vortex upstream of the jet/crossflow interface. This vortex is similar in some ways to the horseshoe vortex which forms around a surface mounted cylinder but is not identical. The key differences between the two are the absence of a no-slip condition around the crossflow disturbance and the flexibility of the jet/crossflow coupling compared to that of a bluff-body in a crossflow.

The horseshoe vortex has not received nearly the attention of the CVP and remains an area of active research. The behavior of the horseshoe vortex falls into one of three different regimes: steady, oscillating or coalescing (Kelso *et al*., 1995), depending on jet-exit Reynolds number and momentum flux ratio. As their names suggest, in these regimes the vortex is either quasi-steady (maintaining a static location in space) or oscillating in space. This vortex system has been linked to phenomena in the wake of a JICF.

Wake Vortices

The wake of a JICF bears some similarity to that of a cylinder in crossflow, particularly in terms of vortex shedding frequency (McMahon *et al*. 1971, Kelso *et al*., 1995). However, researchers have shown conclusively that the wake-vortex formation mechanism of a JICF is fundamentally different to that of a bluff-body in a variety of ways.

Whereas the interaction of a bluff-body with a uniform crossflow is characterized by the pressure drag arising from the rigid interface, the jet/crossflow interface is free to flex and conform in an inter-dependent manner. Coelho and Hunt (1989) showed that while pressure drag is one parameter influencing a JICF wake, its effect is negligible compared to the exchange of streamwise momentum arising from entrainment of the crossflow into the jet. They also showed that the momentum deficit in the wake of a JICF is lower than that of flow over a bluff body of similar size and shape. Unlike in the case of flow over a cylinder, where the wake-vorticity is generated at the cylinder surface, Fric and Roshko (1993) have shown experimentally that the wake-vorticity of a JICF originates in the boundary layer of the wall from which the jet issues. No vorticity is shed from the jet itself. They also found that the streamlines of the flow around a cylinder are far less conformal than those around a jet, resulting in a more open near-wall wake.

One characteristic wake-vortex is the unsteady upright (or ‘tornado’) vortex, which extends from the wall downwind of the jet exit, to the core of the JICF. First observed by Fric and Roshko (1994), the existence of these vortices was soon confirmed by Kelso *et al*. (1996) and Yuan *et al*. (1999). The exact mechanism by which these vortices form is an area of active research. Kelso and Smits (1995) noted that the wake becomes intermittently coupled to the motion of the horseshoe vortex. Yuan *et al*. (1999) suggest the upright vortices arise directly from the interaction of the horseshoe vortices and the vertical jet flow.

Thermo-chemical Structure of the JFICF

The structure of a JFICF is fundamentally similar to that of a non-reacting JICF. All four vortex systems described in the previous section are still present in JFICF. The primary difference between the reacting and non-reacting JICF is the presence in one of heat-release and the associated effects.

Previous researchers have noted a fore-aft asymmetry in the structure of the JFICF. Kadota *et al*. (1990) used gas chromatography to measure the major species concentrations in a turbulent propane JFICF. It showed the mean concentration profiles of major species (propane, CO, CO_2, O_2) evolved into kidney shaped profiles similar to that of the CVP. The peak concentration contours of the CO and CO_2 profiles were seen to reside on lee-ward side of the jet. Peak concentrations of unburned propane were found on the jet-centerline. Similar kidney-shaped concentration profiles were measured by Tsue *et al*. (2000), also using gas chromatography.

Kadota *et al.* (1990) scanned a thermocouple probe through a turbulent propane JFICF and found that its isotherms had a kidney-shaped profile similar to that of the CVP. This study also noted a fore-aft asymmetry in the kidney-shaped profile of the isotherms, with the peak temperature lying on the leeward side of the jet-centerline. Similar temperature profiles, also with a leeward-side peak in temperature, were measured by Tsue *et al*. (2000, 2002) using thermocouples and Rayleigh scattering thermometry, respectively. This fore-aft asymmetry is also seen in lifted JFICF. Birch *et al*. (1989) used a linear rake of ten thermocouples to measure the isotherms of a lifted natural gas jet JFCIF and also found a kidney-shape temperature profile with a leeward-side peak.

The fore-aft asymmetry of the mean temperature and concentration profiles was interpreted by Kadota *et al* (1990) and Tsue *et al*., (2000) as being indicative of enhanced mixing caused by the counter-rotating vortex pair in the flame. The flame was said to be "more active" on the leeward side due to the action of the CVP.

Heat Release Effects

Many studies have examined the effect of heat-release on flow-field characteristics of gaseous turbulent jets and mixing layers. These effects include a modification of the turbulent fluctuations, downstream mixture fraction and centerline velocity decay, near-field shear-layer stability and the buoyant acceleration of hot combustion products. Although there have been far fewer studies specifically examining heat-release effects in turbulent JFICF, much of the aforementioned research is directly applicable to this flowfield. The following section provides a brief summary of the most relevant prior work.

Turbulent Fluctuations

It has long been known that the kinematic viscosity of a gas scales with $T^{3/2}$. Thus, the large temperature rise caused by a flame results in a corresponding increase in kinematic viscosity and reduced local Reynolds number. Studies have concluded that this reduction in local Reynolds number has a substantial effect on the turbulence intensities and mixing characteristics of gaseous jets and shear-layers.

Chigier and Strokin (1974) used a gas tracer diffusion method to compare methane jets and jet-flames and found higher turbulence intensities and mixing in the non-reacting methane jets for the same exit conditions. They attributed this to increased viscous damping and re-laminarization of the flow caused by an order-of-magnitude increase in kinematic viscosity associated with the presence of the flame.

Takagi *et al*. (1980, 1981) conducted a series of experiments to study the effect of heat-release on turbulent (Re = 4200 – 18,000, based on jet-exit conditions) H_2/N_2 jets and jet-flames. Using instantaneous ($2\mu s$) schlieren images, they found the structure of the turbulent flow-field was significantly influenced by the presence of a flame. In particular they noted that the outer layer of the near-exit region appeared to be locally laminarized while the core of the jet remained turbulent. They used laser Doppler velocimetry (LDV) to measure mean and fluctuating velocity components in the H_2/N_2 jets and jet-flames and found that in the near-exit region, the jet-flames had lower turbulence intensities than their non-reacting counterparts. They attributed this to the local increase in kinematic viscosity caused by the temperature rise associated with the presence of a flame. This study also found that, whereas the turbulence intensities of the non-reacting H_2/N_2 jets peaked near the jet-exit and decayed with downstream distance, in the flames the opposite occurs. They found that in the flames turbulence intensities grew with downstream distance and reached a peak near the flame-tip. They suggest this is the result of decreased centerline velocity decay (characteristic of flames) maintaining a higher turbulence-inducing velocity gradient with the surrounding flow in the downstream region of the jet.

Muniz and Mungal (2001) used particle image velocimetry (PIV) to study heat-release effects in a pair of hydrogen-piloted, turbulent, nitrogen-diluted natural gas jets and jet-flames in a co-flowing air-stream. Consistent with the work of Takagi *et al.* (1980, 1981) they found that the presence of a flame resulted in the suppression of near-exit turbulence intensity. Also consistent with Takagi *et al.* (1980, 1981), they observed a growth in turbulence intensity with downstream distance in the jet-flames. They concluded that the near-exit suppression of turbulence intensity was a result of heat-release and the subsequent rise was associated with buoyancy. This study also found that the heat-release reduced the local Reynolds number ($Re_x = u_c 2\delta_{1/2}/\upsilon_c$, where $2\delta_{1/2}$ is the full width at half maximum velocity and υ_c is the local centerline kinematic viscosity) by a factor of ten.

Differences in kinematic viscosity and local Reynolds number alone however, do not appear to fully explain the modifications to the large-scale structure of the jets brought about by heat-release. Rehm and Clemens (1999) used planar laser Mie scattering (PLMS) to compare a planar jet flame with several non-reacting planar jets. Rather than comparing flows with identical exit conditions, this study compared jets and jet flames with the same local Reynolds numbers (Re_δ) and different jet-to-ambient fluid density ratios. Density ratios for the nonreacting planar jets ranged from 0.14 (helium into air) to 4.8 (Halocarbon 116 into air). In this study they compared the large-scale turbulent fluctuations of the planar jets and jet-flames using the RMS jet-to-ambient fluid intermittency. They found that despite having locally matched Reynolds numbers, the non-reacting planar jets had substantially greater large-scale turbulent fluctuations in the far-field region. They also found the RMS intermittency profile (normalized with the local jet width) of the planar jet flame was substantially narrower than that of the non-reacting cases, which overlapped with each other. They concluded that the differences in turbulent flow-structure were not due to either global laminarization or global density changes resulting from heat-release.

Density Effects

High levels of heat-release from a flame alter both the local and the global density profiles of a gaseous turbulent jet. Conservation of momentum dictates that a modification of the global density profile necessitates a corresponding modification of the velocity characteristics of the jet. Numerous studies have examined what effect the density modification caused by a flame has on the velocity, mixture fraction and entrainment characteristics of a jet.

Centerline Decay in Straight Jets

Thring and Newby (1953) found that the mixing and entrainment characteristics of a turbulent jet scaled with the "equivalent nozzle radius" $r' = r\,(\rho_o\,/\rho_\infty)^{1/2}$, (more commonly known today as the "modified source diameter" $D_s = d\,(\rho_o\,/\rho_\infty)^{1/2}$). Riccou and Spalding (1961) experimentally measured the entrainment of a turbulent, isothermal free-jet and found that

$$\frac{\dot{m}}{\dot{m}_0} = 0.32\frac{x}{D_s}$$

Thus, in a jet with lower jet-to-surrounding density ratio, one would expect greater entrainment and more rapid mean centerline velocity decay with downstream distance.

Perhaps counter-intuitively, studies have shown that velocity, concentration and entrainment profiles of a gaseous turbulent jet-flame scale similarly to an isothermal, non-reacting jet with a higher jet-to-ambient density ratio. Chigier and Strokin (1974) measured faster decays of mean centerline velocity and concentration in non-reacting jets than in corresponding jet-flames. Takagi *et al.* (1980, 1981) also found jet-flames had a lower rate of mean centerline velocity decay than non-reacting jets of similar exit-conditions, a characteristic they attributed an acceleration of the flow caused by the volumetric expansion associated with the flame. The PLMS study of Rehm and Clemens (1999) found reduced mixture fraction decay in turbulent planar-jet flames compared to non-reacting planar jets of equivalent local Reynolds number, indicating the reduced centerline decay is unrelated to local Reynolds number. Muniz and Mungal (2001) also measured decreased mean centerline velocity decay in jet-flames compared to non-reacting jets with the same exit conditions. In this study, heat-release was seen to reduce global entrainment by ~50%. Han and Mungal (2001) used PIV to directly measure entrainment in turbulent jets and found heat-release suppressed entrainment in jet-flames by a factor of 2.5 for a typical hydrocarbon fuel in air. The study also found that buoyancy acted to compensate for the reduced entrainment further downstream.

Tacina and Dahm (2000) developed a general equivalence principle which they then applied to both axisymmetric and planar turbulent jets in order to more rigorously extend the isothermal scaling relations of Thring and Newby (1953) and Riccou and Spalding (1961) to the case of turbulent flows with heat-release. Their model was limited to those cases where the relative influence of buoyancy is negligible and the flows have sufficiently high initial (room-temperature) Reynolds numbers to remain turbulent even after the aforementioned increase in kinematic viscosity and the associated reduction in local Reynolds number. In this study they derive a set of scaling laws based on what they call the “extended momentum diameter” D^+, which is defined as

$$D^{+} = \begin{cases} \left(\dfrac{\rho_0}{(\rho_\infty)_{eff}} \right)^{1/2} D_0 & for \quad \mathrm{X} > \mathrm{X}_s \\ \left(\dfrac{(\rho_0)_{eff}}{\rho_\infty} \right)^{1/2} D_0 & for \quad \mathrm{X} < \mathrm{X}_s \end{cases}$$

where X_s is the stoichiometric mole fraction, D_0 is the jet-exit diameter and $(\rho_0)_{eff}$ and $(\rho_\infty)_{eff}$ refer to modified (or "effective") densities of the jet and ambient fluids, respectively. The effective densities are based on the assumption that local fluid temperature is a piecewise linear function of the mole fraction X at that location. Their D^+-based scaling law shows good agreement with the measured velocity and conserved scalar decay profiles for a wide range of planar and axisymmetric turbulent jet-flames meeting the model's assumptions (high *Re* with negligible buoyancy).

Centerline Decay Profiles in JFICF

Although the studies described above were conducted with straight jets and jet-flames, similar mean centerline decay characteristics have been observed in turbulent JFICF. Kadota *et al.* (1990) used LDV to measure velocity profiles of turbulent propane JFICF. That study showed slower centerline velocity decay in the (reacting) JFICF compared to a non-reacting JICF of similar exit conditions. This study also found that the presence of a flame in the JICF inhibits the development of the CVP in the core of the jet causing it to form further downstream.

In a study by Hasselbrink and Mungal (2001b) PIV was used to study the mean and fluctuating velocity profiles of two turbulent ($r = 10$, $Re = 6000$ and $r = 21$, $Re = 12{,}800$ respectively) methane jets and jet-flames in a crossflow. This study used a horizontal jet issuing into a vertical crossflow. Consistent with the observation of Kadota *et al.* (1990) and the previously mentioned studies on heat-release in straight jet flames, they found that heat release in a turbulent JFICF resulted in reduced mean centerline velocity decay. They also found (perhaps unsurprisingly, given the highly directional nature of the JICF) that the heat-release of the flame affected the u' and v' velocity fluctuations differently. They found that the v'_{rms} field was affected by the flame to a greater degree than the u'_{rms} field, with the contours of v'_{rms} being highest in the region of the flame envelope. The loci of maximum u' and v' were seen to fall very close to the center streamline of the jet.

The v'_{rms} data in Hasselbrink and Mungal (2001b) displayed a dual-peak profile in the far-field region for the $r = 10$ flame case. A similarly bifurcated profile was not seen in either the $r = 21$ flame or non-reacting JICF they studied. They attributed the bifurcation to buoyancy. The values of the Becker and Yamazaki (1978) buoyancy parameter (to be discussed in greater detail shortly) for the $r = 10$ and $r = 21$ flames were 2.7 and 1.8, respectively.

Flow Stability

Local density modifications (caused by the presence of a flame) in the near-field of a gaseous turbulent jet are known to significantly influence its downstream mixing and entrainment processes.

Savas and Gollahalli (1986) used short time-exposure ($2.5\,\mu s$) schlieren photography to compare the near-exit flow structure of a propane jet, jet-flame and lifted jet flame of equal jet-exit Reynolds number ($Re = 13000$). They found that the presence of a flame delayed the formation, rollup and coalescence of the near-exit shear-layer vortices considerably. They also noted that the flame severely inhibited the secondary instability responsible for distortion of the shear-layer vortices. They concluded that the effect was caused by decreased density and increased viscosity associated with the flame and that the behavior of the shear-layer is controlled by the presence of the flame.

Ellzey and Oran (1990) conducted a computational study to examine the effect of heat-release on the stability of transitional (Re_j = 2100) jet-flames. In this study, they simulated laboratory-scale (D = 5 *mm,* u_j = 10 *m/s*) nitrogen-diluted hydrogen jets and jet-flames. By holding the viscosity constant in their numerical scheme (rather than allowing it to vary with temperature, as would be physically realistic) and comparing the reacting and non-reacting jets they were able to conclude that it is volumetric expansion, rather than the modification of kinematic viscosity, that causes the stabilization of the flow in the near-field of turbulent jet-flames.

Clemens and Paul (1995) used laser-induced fluorescence (LIF) to study the effect of heat-release on the near-field flow structure of turbulent (Re = 2500 - 50,000), co-flowing jets and jet-flames. Their jet fluids were H_2/N_2, H_2/He and pure hydrogen. They found that the dominant parameter governing the growth of the shear-layer in turbulent jet-flames is the density ratio between the jet and the surrounding fluid. The growth rate of the near-field shear layer was found to be significantly higher in jets with lower jet-to-ambient density ratios. Comparing reacting and non-reacting jets of similar exit-conditions, they also noted that the growth of shear-layer vortices was substantially reduced by the presence of the flame. In effect, the presence of the flame caused the jet to behave as if it had a higher jet-to-ambient density ratio.

Buoyancy Effects

A key implication of density modification caused by the presence of a flame in a turbulent jet is the addition of a buoyant acceleration to the flow. It has long been known that the buoyant acceleration of fluid in a turbulent jet can, in certain circumstances, significantly alter such parameters as the entrainment rate and centerline velocity decay. Buoyancy is also known to affect the coherence and stability of the large-scale flow structure of a gaseous turbulent jet flame.

Noting that previous scaling laws for entrainment in turbulent jets did not adequately account for the effect of buoyancy, Becker and Yamazaki (1978) conducted an experimental study using a series of vertical turbulent nonpremixed propane jet-flames. The study was designed to examine the effect of buoyancy on the mean entrainment, growth rate and temperature profiles of vertical, turbulent jet-flames and establish a universal scaling parameter to quantify the effect. They determined that a local Richardson number ($Ri_s = gD_s/u_0^2$, where for the case of a jet with a uniform exit-velocity profile U_0 is the jet-exit velocity) is the dominant governing parameter relating buoyancy and entrainment characteristics. This rescaled Richardson number, hereafter referred to as the Becker and Yamazaki buoyancy parameter is defined as

$$\xi_L = \left(Ri_s\right)^{1/3} \frac{L}{D_s}$$

or

$$\xi_L = \left(\frac{gD_s}{U_0^2}\right)^{1/3} \frac{L}{D_s}$$

In this definition, *L* refers to the flame-length.

In this study, Becker and Yamazaki (1978) used a thermocouple and a pitot-tube to measure mean temperature and impact pressure respectively. They also used still-photography to examine the instantaneous luminous structure of their propane jet-flames. Based on their measurements, they determined that in flames with ξ_L values of less than unity the flow reaches a momentum-dominated (forced convection) limit and scales with

D_s only. In this regime buoyancy effects become negligible. Based on their measurements, they concluded that downstream entrainment in turbulent jet flames scaled as

$$\frac{\dot{m}}{\dot{m}_0} \cong \begin{cases} 0.16 \dfrac{x}{D_s} & for \quad \xi_L < 1 \\ 0.08\, \xi_L^{3/2} \dfrac{x}{D_s} & for \quad \xi_L > 2.5 \end{cases}$$

Since the work of Becker and Yamazaki (1978) studies have reexamined the value of ξ_L beyond which a flow may be considered momentum-dominated. Idicheria *et al.* (2004) used high-speed digital imaging of natural flame luminosity to examine the effect of buoyancy on a series of turbulent nonpremixed hydrocarbon jet flames issuing into quiescent air. Based on analysis of mean and RMS flame-luminosity, flame length fluctuations and volume rendering of time-resolved image sequences of flame luminosity, this study concluded the large-scale turbulent structure reaches a momentum-dominated, asymptotic limit for ξ_L less than 2 – 3. The same study also found that convection velocity of large-scale luminous structures (i.e. the celerity) normalized with jet-exit velocity was constant for $\xi_L < 6$ but scaled with $\xi_L^{3/2}$ when $\xi_L > 8$. The study isolated the effect of the ξ_L parameter from Reynolds-number effects by conducting imaging experiments on similar flames in normal and low-gravity.

In addition to the effect it has on entrainment and mean centerline velocity decay profiles, buoyancy is also known to affect the stability and coherence of the large-scale flow-structure of transitional and turbulent jet-flames. Katta and Roquemore (1993) performed a computational study of the time-dependent characteristics of the inner and outer vortex structures of a straight, vertical transitional propane jet-flame. In that study, buoyancy was seen to play a significant role in maintaining the coherence of the inner-vortices of the transitional flames and retarding their transition to turbulence. In their previously mentioned computational study Ellzey and Oran (1990) discovered that buoyancy led to the formation of large structures outside the reaction zone which had the effect of distorting the temperature field of the jet-flame as they moved downstream.

Bahadori *et al.* (1993) studied the effect of buoyancy on laminar and transitional jet-flames by comparing a series of flames in normal-gravity with otherwise similar ones in the low-gravity environment of a drop-tower. They used video rate imaging, thermocouples, gas sampling probes and a radiometer to examine methane, propane and propylene jet-flames issuing into a closed chamber filled with 15-50% O_2 in N_2 and pressurized between 0.5 and 1.5 *atm*. They found that whereas in normal-gravity jet-flames the transition to turbulence begins with disturbances forming near the flame-tip and moving down through the flow toward the jet-exit, in low-gravity disturbances form near the base and convect downstream. They attributed this difference to the strong influence of buoyancy on the flow-field under normal-gravity conditions. They also found the transition to turbulence in normal-gravity flames was accelerated due to buoyancy-generated turbulence.

In the related work of Hegde *et al.* (1994), similar effects were seen. In this paper, the authors also noted intermittency in the disturbances observed near the base of the flame which gave way to a continuous train of structures with increasing Reynolds number. From this they concluded that transition in their microgravity flames originated in the fuel line prior to the jet-exit, rather than from buoyancy-induced instability of the shear-layer of the jet.

The aforementioned imaging study by Idicheria *et al.* (2004) revealed that the large-scale luminous structures of a turbulent hydrocarbon jet-flame appear more organized and coherent in the momentum-dominated regime than when they were significantly influenced by buoyancy. Based in part on this (and in part on flame length fluctuation measurements and volume rendering of image sequences), they concluded that buoyancy acts to disrupt the Kelvin-Helmholtz instability in the jet and thus decrease the coherence of the turbulent structures.

Compared to the amount of research devoted to the study of buoyancy in straight turbulent jet-flames, there has been comparatively little attention paid to the parameter in turbulent JFICF. In fact, there appears to have been virtually no systematic effort to rigorously analyze buoyancy as an independent parameter affecting the velocity decay, entrainment and large-scale flow-stability of turbulent JFICF.

A search of the literature on turbulent JFICF revealed no universal scaling parameter comparable to ξ_L for quantifying buoyancy in these flows. Becker *et al.* (1981) use ξ_L as a measure of comparison between horizontal, turbulent non-premixed propane flames in still air, though with little rigorous justification. Rao and Brzustowski (1982) use the Froude number ($Fr_j = v^2(\rho_\infty/\Delta\rho) / (gd)$, where $\Delta\rho$ is the difference between a characteristic fluid density in the luminous flame and that of the crossflow fluid) to quantify buoyancy effects on the power-law exponent of the jet-centerline trajectory scaling. Hasselbrink and Mungal (2001b) use ξ_L to estimate the relative influence of buoyancy in their lifted, horizontal methane JFICF. Indeed, given the number of possible configurations of the JFICF (e.g. vertical jet in horizontal crossflow, horizontal jet in vertical crossflow, perpendicular vs. non-perpendicular jet-to-crossflow injection angle etc.), it is not clear there exists a single, universal scaling parameter comparable to ξ_L with which to quantify the effect of buoyancy in turbulent JFICF. It is possible however, to examine the applicability of ξ_L to the examination of certain specific cases of the turbulent JFICF. Naturally, one should not expect the JFICF to scale with ξ_L in exactly the same manner as a vertical turbulent jet-flame.

Preliminary work in the current study, reported in Boxx *et al.* (2003) and Boxx *et al.* (2004) showed evidence that, consistent with the observations of Idicheria *et al.* (2004) for the case of a straight jet-flame, buoyancy affects the coherence and stability of large-scale luminous structure of turbulent JFICF. Boxx *et al.* (2003) also showed differences in centerline trajectory, mean luminous flamewidth and shear-layer vortex coherence and spacing with increasing levels of buoyancy. The preliminary observations outlined in that paper illustrate the important, though little examined role buoyancy plays in determining the mean and instantaneous characteristics of turbulent JFICF.

OBJECTIVES AND APPROACH

As shown in the previous section, the heat-release associated with the presence of a flame is responsible for a multitude of flow-field modifications. The volumetric expansion caused by the heat-release is seen to alter mean entrainment and centerline velocity decay, turbulence intensities (in both the near-exit and downstream locations) and the growth and stability of the near-exit shear layer. The relatively few studies on heat-release in turbulent JFICF identify similar effects in that flow-field. The buoyancy associated with the volumetric expansion is seen to affect the mean entrainment and influence the large-scale stability and coherence of straight turbulent jet-flames. No previous study appears to have decoupled the volumetric expansion caused by a flame in a turbulent JICF from the buoyancy-force induced by that expansion. This work will begin to fill that gap.

The objective of the present work is to experimentally isolate buoyancy in turbulent, hydrogen-diluted hydrocarbon JFICF and investigate its influence upon a range of flow-field characteristics. The primary interest is in how buoyancy affects the large-scale structure of the turbulent flow-field, its vortex systems and ultimately, the mixing, entrainment and penetration characteristics. Each of these characteristics is dependent upon a range of related parameters, including momentum flux ratio *r*, jet-exit Reynolds number, chemistry and jet-exit diameter. Although it would be possible to eliminate buoyancy effects by simply driving jet-exit and crossflow velocities high enough to reach a forced-convection limit, doing so would change the Reynolds number and thus make comparison to a buoyant JFICF difficult. A more effective way to study buoyancy effects is to compare two otherwise identical flames in normal- and low-gravity. This study uses a microgravity drop-tower facility to do just that.

This study focuses on a series of hydrogen-diluted propane JFICF with momentum flux ratios ranging from 7 to 11.5 and Reynolds numbers (based on room-temperature, jet-exit conditions) between 3350 and 5500. The flames are unpiloted and fully attached (non-lifted) throughout. The reduced gravity environment was produced in the University of Texas Drop-Tower Facility (UT-DTF). High frame-rate, cinematographic imaging of flame luminosity was used to study the large-scale structure, trajectory, flame-length and flame-tip dynamics. High frame-rate, cinematographic PLMS was used to characterize the large-scale structure, mixture fraction decay and jet-to-crossflow intermittency fields.

One important component of this study was to develop and advance the state-of-the-art in planar laser imaging combustion diagnostics in low-gravity facilities. Although such tools as PLMS and particle image velocimetry (PIV) are well developed and widely applied in the field of combustion research, their use in microgravity combustion research has been very limited. As part of this study, an advanced, fiber-optic based, multi-kHz frame-rate PIV/PLMS system for use in a microgravity drop-tower was developed. This system is the first (and only) multi-kHz framerate planar laser scattering/imaging system designed for use in a microgravity droptower and constitutes a major advance in droptower combustion diagnostics.

Chapter Two: EXPERIMENTAL DETAILS

The research study described in this dissertation was conducted in the Microgravity Combustion and Laser Diagnostics Laboratory at the University of Texas at Austin. The experiments were conducted in the University of Texas Drop Tower Facility. The following chapter provides a detailed description of the experiment apparatus, facilities, diagnostic techniques and experimental procedure used in this study.

DROP RIG

The experiments were conducted in a drop-rig that was built at the University of Texas at Austin in collaboration with the NASA-Glenn Research Center (NASA-GRC). The drop-rig is shown schematically in Figure 2.1a. This three-dimensional schematic is significantly over-simplified in order to improve displayability. Figure 2.1b shows a more complete view of the rig from the exterior. Figure 2.2 shows the interior layout. The experiment was housed in an aluminum frame (provided by the NASA-GRC), which measures 965 *mm* long by 406 *mm* wide and stands 914 *mm* tall and contains several subsystems. These subsystems include a blow-through jet-flame-in-crossflow facility, pressurized gas and electrical systems, automation system and laser diagnostics system. Each of these subsystems will be described in detail in the following sections. Fully loaded, the drop rig has a mass of 115 *kg*.

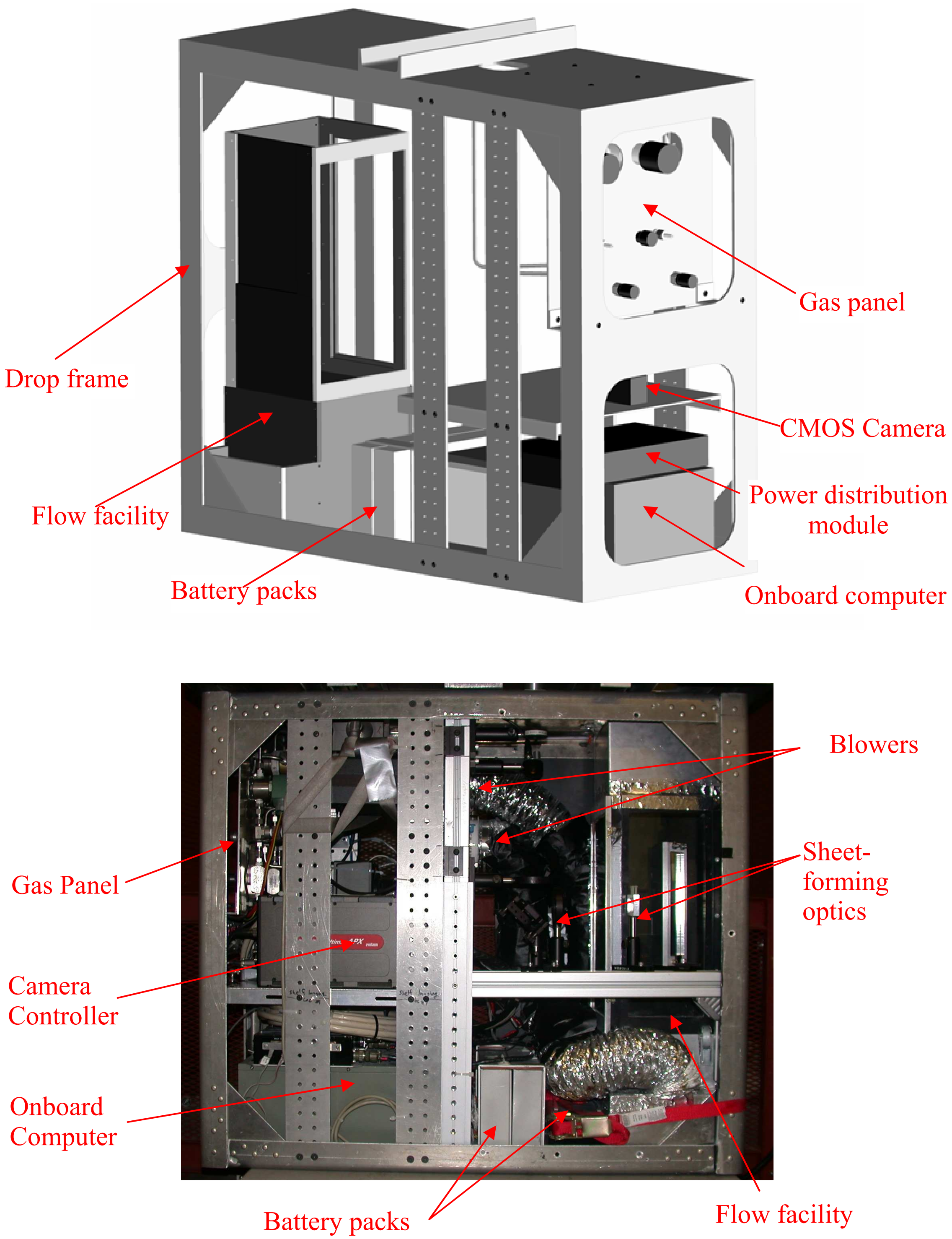

Figure 2.1 (a) Simplified schematic diagram of the drop-rig (b) Photograph of the drop-rig.

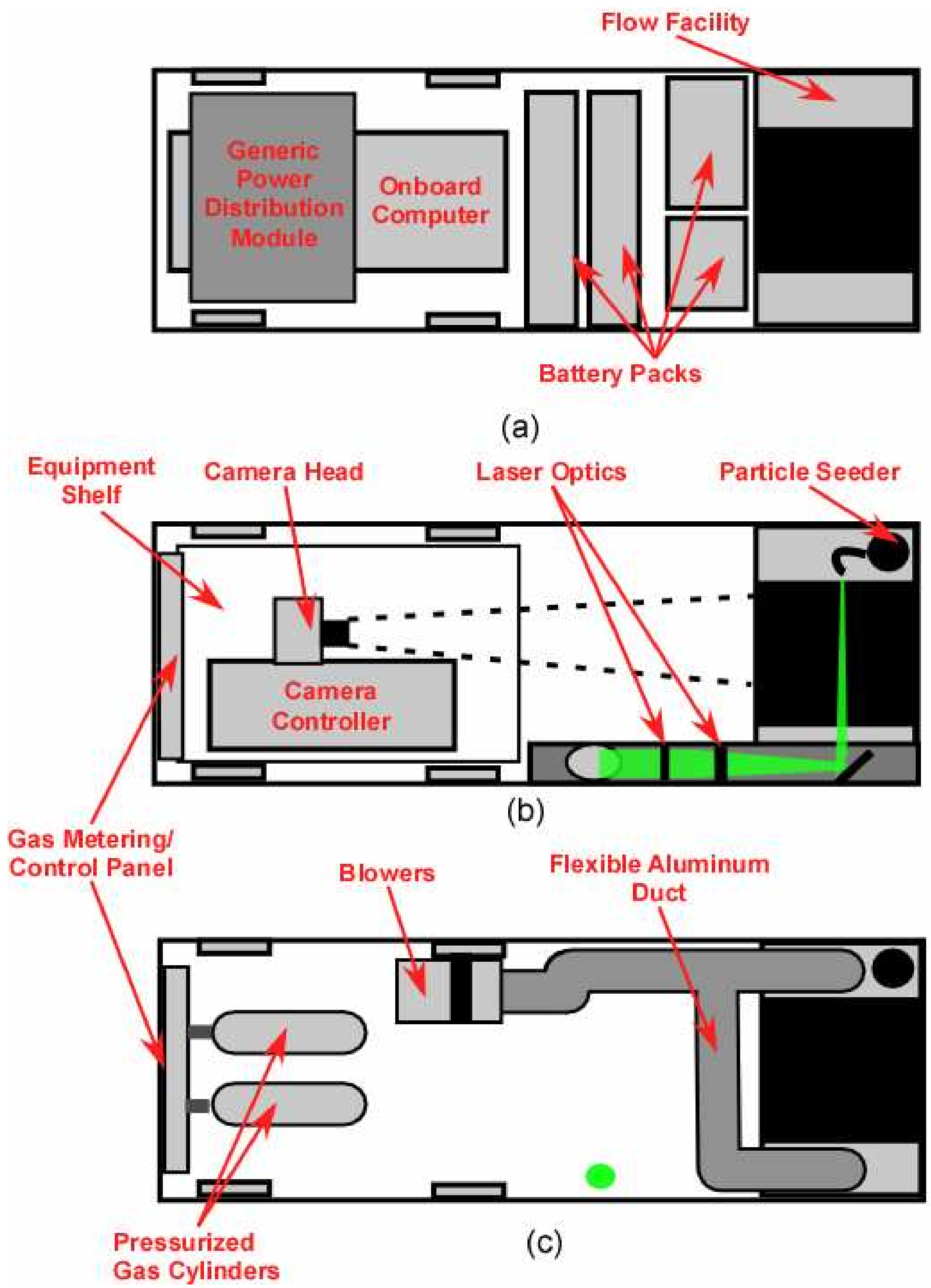

Figure 2.2 Schematic diagram showing locations of key subsystems inside the rig. (a) Floor of rig. (b) Camera / optical shelf level. (c) Upper / roof section (Note: Only approximately to scale.)

Jet-Flame in Crossflow Facility

Mounted in the front of the drop-rig is a compact, self-contained, blow-through jet-flame in crossflow facility. The facility was designed in part based on the volumetric and electrical power constraints imposed by use in a microgravity drop-tower. The facility (to be described in detail in this section) was designed with the goal of maximizing volume and optical access in the test section while also generating jet and crossflow velocities comparable to those obtainable in larger stationary test facilities.

Flow Conditioning and Test Section

The flow-facility, shown in Figure 2.3, has a test section which measures 203 *mm* × 203 *mm* in cross-section and is 610 *mm* tall when mounted in the drop-rig. The test section has a 200 *mm* × 375 *mm* imaging window and a 140 *mm* × 368 *mm* laser access port. Flow is exhausted from a vent in the roof of the drop rig, which also serves as an entry point for insertion of an starter wick used to ignite the fuel jet prior to a test.

The flow-facility is driven by two Jabsco Model 30500-0024 DC powered, 102 *mm* diameter, axial, in-line blowers. The blowers are each rated for 0.11 m^3/s at zero downstream pressure drop. They are routed to a turning/settling chamber via 102 *mm* diameter, flexible aluminum duct. Following the settling chamber is a 25.4 *mm* deep section of 3.18 *mm* cell-size aluminum honeycomb, used as a flow straightener and de-swirling device. Following this are a layer of perforated plate and a wire-mesh flow-conditioning screen. The flow exits this flow-conditioning device directly into the test section of the flow-facility. Volumetric constraints imposed by the drop-rig prevent the use of a contraction between the two.

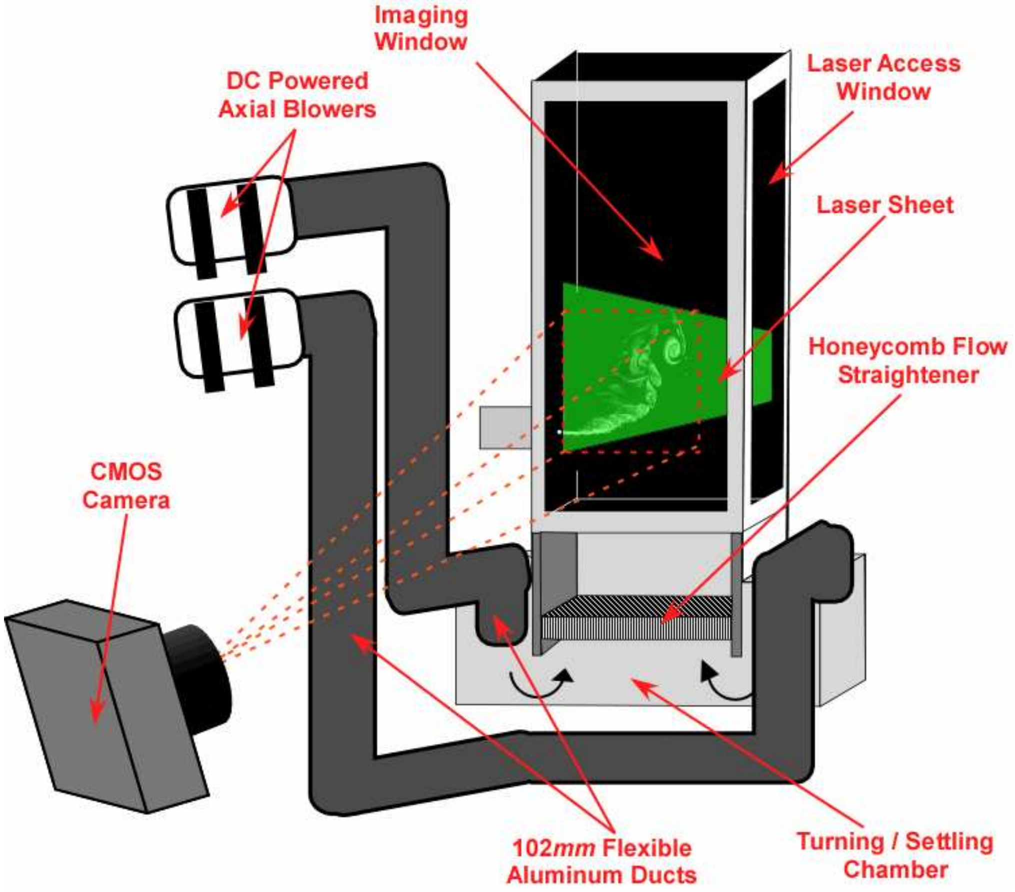

Figure 2.3 Schematic of jet flame in crossflow facility

The crossflow velocity with both blowers running is 1.3 *m/s*. Figure 2.4 shows a velocity profile across the crossflow taken 121 *mm* downstream of the flow-conditioning screen. This profile was measured with a hot film anemometer (TSI Model 1051-2 with a 1210 probe). Outside the boundary layer region at the walls, the flow has a peak-to-peak nonuniformity of less than 6% of the mean flow velocity. Lack of physical access made it impossible to measure a velocity profile in the perpendicular direction. Due to the symmetry of the air-inlet ducts and the flow-conditioning elements, it is reasonable to assume a similar velocity profile in the other direction.

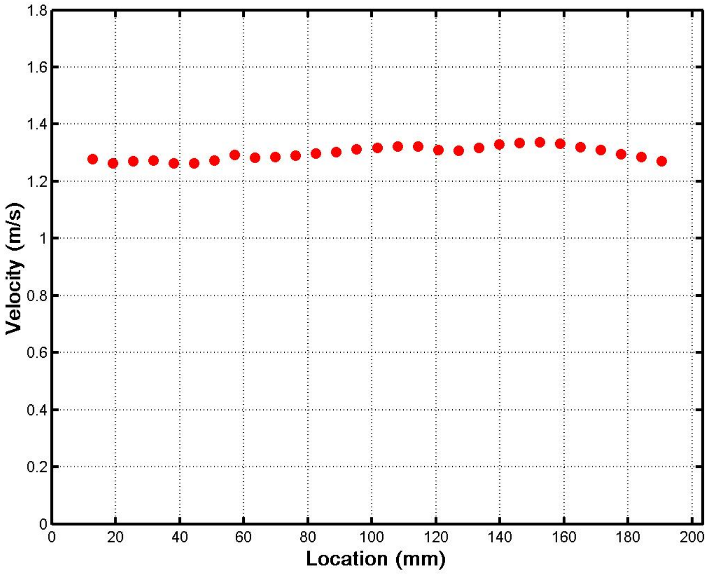

Figure 2.4 Velocity profile across test-section 121 mm downstream of flow-conditioning screens, at the level of the jet-exit.

Jet Nozzle

The jet issues from a 3.18 *mm* diameter, circular orifice mounted flush with one wall of the test section. Fuel for the jet flows from a 6.35 *mm* O.D. tube into a settling chamber before exiting through a axisymmetric contraction with a radius-of-curvature to exit-diameter ratio of 5. Figure 2.5 shows a typical velocity profile of across the injector nozzle taken approximately two jet diameters from the jet-exit.

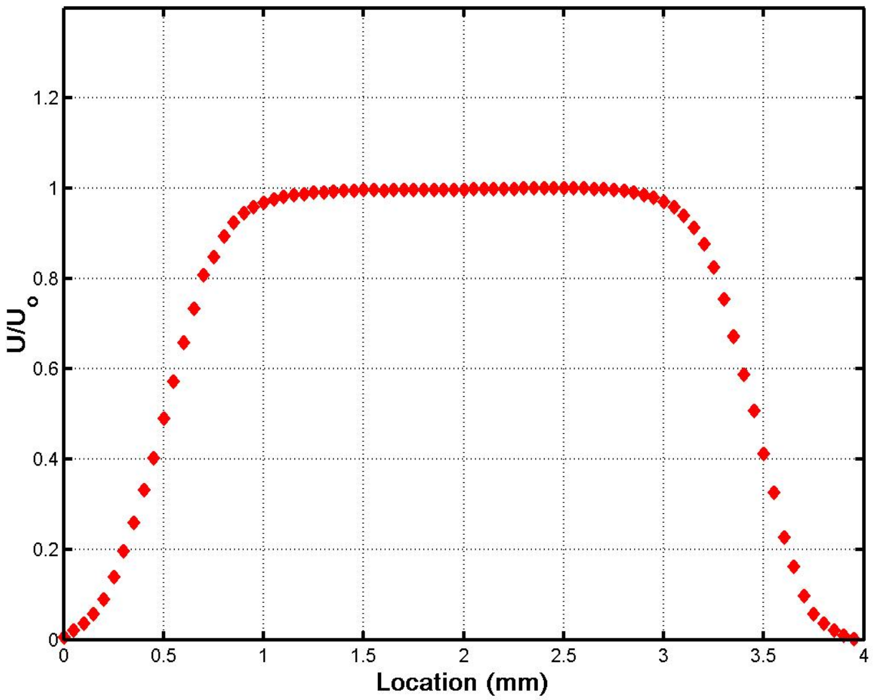

Figure 2.5 Velocity profile of fuel injector.

Pressurized Gas System

Fuel for the jet flame was stored in two 300 *ccm* stainless steel pressure vessels mounted on the (inside) roof of the drop-rig. Fuel flowed through 6.35 *mm* O.D. stainless steel tubing from each of these vessels to two separate, in-line pressure regulators and then to choked micro-metering valves, which regulated the mass flow rate of the system. Line-pressure was read by Omega PX-236 pressure transducers and stored in the memory of the on-board computer. Solenoid valves were used to turn the flow on and off. They were controlled via solid-state relays by the on-board computer system. The system had two manual on-off valves and adjustable, spring-loaded pressure relief valves. Each pressure vessel / flow control line could be used independently or in tandem with the other, depending on the goal of each experiment.

Accelerometers

The background acceleration felt in the drop-rig during freefall was monitored with a Kistler model 8304-B2 “K-beam” accelerometer. This accelerometer uses a silicon cantilever beam mounted in between two plates to measure acceleration via the associated change in capacitance of the system. It had a frequency response of 300Hz, resolution of $140\mu g_{rms}$ and a range of ±2*g*. Measured background acceleration levels (“g-gitter”) were in the range of 5-10milli-*g*. Deceleration caused by the impact of the drag-shield/drop-rig with airbag was measured with a Kistler Model 8303-A50 “K-Beam” capacitive accelerometer. Impact deceleration levels were measured to be approximately 15-*g*.

Automation System

An on-board computer was used to automate the drop-rig and control timing and sequencing of the experiment during a drop test. The computer was a custom-configured, passive back-plane type machine from CyberResearch Inc. It had an Intel Celeron 466MHz CPU card and 256MB of RAM. It was equipped with a 63.*5mm* profile, 1.2GB solid-state, IDE hard drive. The hard-drive was mounted in a shock-isolation chassis inside the computer to protect it from the force of impact. The computer ran the Windows NT operating system. Due to the space constraints of the drop-rig, the on-board computer was without a monitor, mouse or keyboard. Instead, it was controlled remotely from a desktop PC via a removable crossover cable using the “RealVNC” virtual network computing software package. Timing and control of the experiment rig during each drop was attained through the use of a program written in the National Instruments LabView software environment.

The computer controlled the pressurized gas and flow-facility blower systems using solid state relays connected to a National Instruments PCI-6023E analog/digital I/O data acquisition (DAQ) card via an SCD-68 breakout panel. It also read in and stored data from the Kistler model 8304-B2 "K-beam" capacitive accelerometer and Omega PX-236 pressure transducers mounted in the rig.

Electrical System

Power for the solenoid valves, blowers and on-board computer system came from two hardened, onboard 24 *V*, 5 amp-hour battery packs developed by NASA-GRC. The high frame-rate onboard camera system (to be described later) was powered by two 12 *V*, sealed lead-acid batteries. All batteries were mounted to the floor of the drop-rig, where they doubled as ballast to stabilize the rig during impact. Electricity is routed to different systems in the rig using a generic power distribution module also developed by NASA-GRC.

Drag Shield

During low-gravity experiments the rig was enclosed within an aerodynamic drag-shield. The drag-shield was designed to minimize the effect of wind-resistance felt by the drop-rig during a drop test and thus minimize background acceleration levels felt by the experiment. The drag shield was designed to be bottom-heavy for stability during impact. Its base was built from a 1.02 *m* long section of 0.51 *m* diameter, schedule-10 (6.35 *mm* wall thickness) steel pipe, which was cut down the middle to form a "half-pipe". The half-pipe was fitted with a rubber-lined, reinforced steel plate, which serves as the base upon which the drop-rig sat.

The remainder of the drag-shield was a light-weight rectangular shroud designed to totally enclose the drop-rig. The shroud was composed of an aluminum frame lined with 1.6 *mm* thick 6061-T6 aluminum sheet metal. It measured 0.51 *m* wide by 1.02 *m* and stood three inches taller than the drop-rig it was designed to shield. The sheet-metal liner of the shroud was hinged on four sides to allow easy access to the drop-rig. The shroud was attached to the base with four hardened steel cotter pins.

During a drop-test, the rig was suspended from the drop-tower release mechanism via a wire rope. The drag shield hung suspended upon the drop-rig. At the initiation of the drop, the rig was released. As there was no physical anchor between the rig and the shield, the two were free to move with respect to each other. Being on the outside, the drag shield began to decelerate due to the wind resistance and move relative to the drop rig. This effectively shielded the drop rig from the effects of wind-resistance induced deceleration. By the end of the drop test the drag-shield and the drop rig were almost in contact with each other.

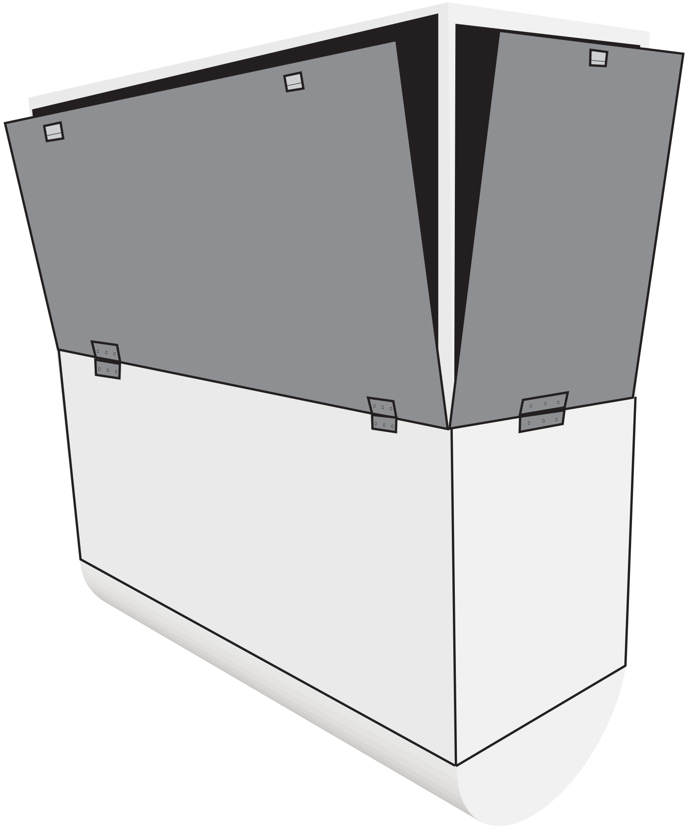

Figure 2.6   Schematic of aerodynamic drag shield.

UNIVERSITY OF TEXAS DROP TOWER FACILITY

The experiments were conducted in the University of Texas Drop Tower Facility (UT–DTF). The UT-DTF, shown in Figure 2.7, is located in Room 1 of the W.R. Woolrich Laboratories building. It stands 10.7 *m* tall in total, with a cross-section measuring 2.5 *m* × 2.5 *m*. It is equipped with a catwalk platform work area at the top and 2-ton capacity electric hoist, mounted on a roller trolley. Attached to the hoist's chain is an Eastman Aircraft Corporation, quick-release cargo hook. This is used to drop the rig from a height of approximately 9.1 *m*. The catwalk area is accessed from a door located at the top of the shaft.

At the bottom of the drop shaft was a deflatable-airbag type deceleration mechanism. This system was contained within a heavy frame of welded steel C-section channel of dimensions 1.83 *m* high by 1.7 *m* long by 1.12 *m* wide. The bottom third (approximately) of the frame was lined with 3.2 *mm* plate steel and the upper portion with expanded metal. Attached to the steel plate lining the lower part of the steel frame was an inflatable rectangular bladder. This bladder was made of a 22 *oz* nylon coated polyester material similar to that used in boat and trailer covers. The frame was bolted to the floor of the drop shaft and lined with a single 0.3 *m* thick slab of stiff, high-density (110 *lb*) polyurethane foam padding. The airbag was pressurized using a radial blower with a 0.27 *m* diameter cast aluminum blade. The blower was driven by a completely enclosed, drip-proof 3-phase, 220V 1.5HP motor. Upon impact of the drop-rig/drag-shield, the bladder deflated through four spring-loaded rectangular blast gates mounted in the steel liner of the base of the deceleration system. The blast gates were mechanically restricted in how wide they could open, so as to provide a measure of control of impact deceleration. It was found the deceleration mechanism slowed the experiment package with a deceleration of 10-15g, which was well within the survivability limits of the on-board equipment.

Taking the space required for the electric hoist, release mechanism and deceleration box into account, the low-gravity time available for the experimental rig was approximately one second per drop.

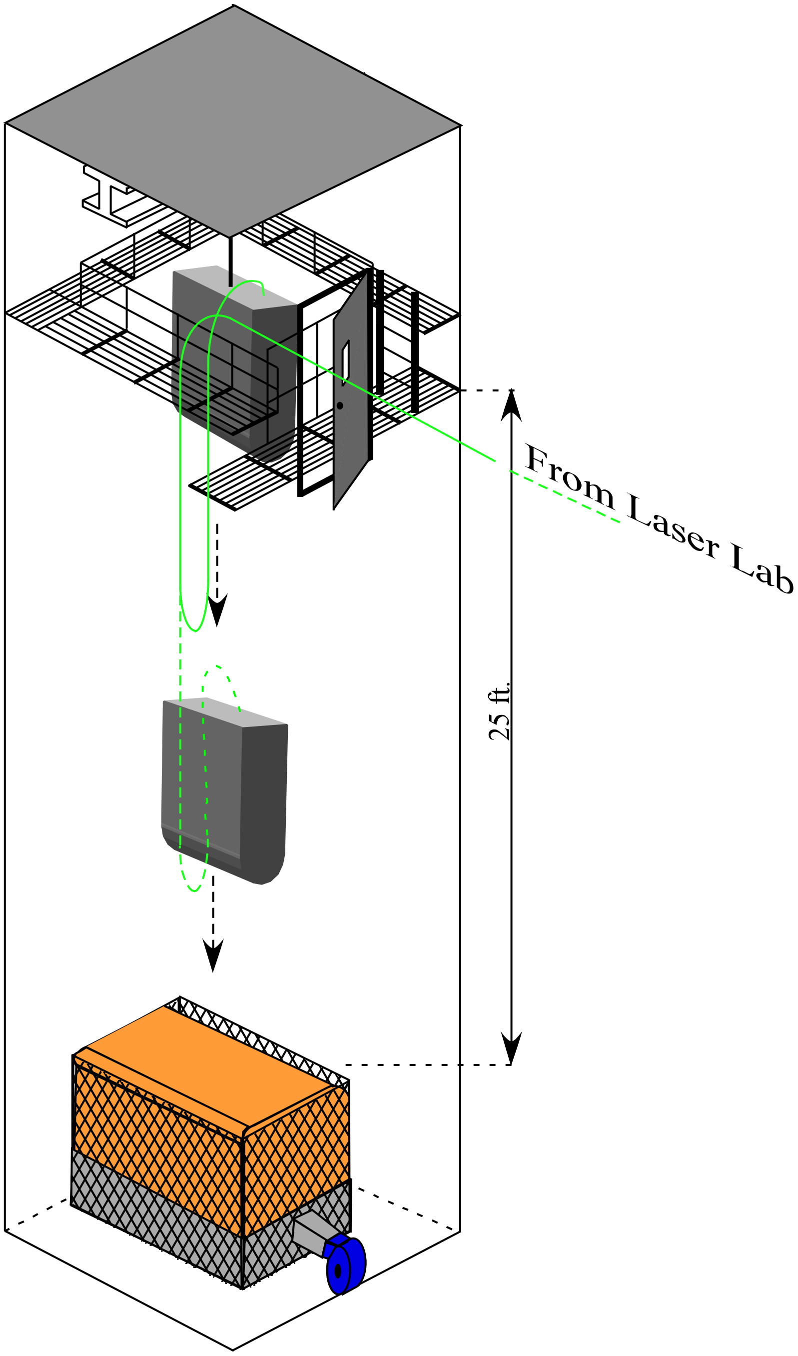

Figure 2.7 Schematic of University of Texas Drop Tower Facility

PLMS SYSTEM

The PLMS system designed and built for this study used a large core-diameter fiber-optic cable to deliver light from a diode-pumped Nd:YAG laser to the drop-rig during a drop. A set of optics in the drop-rig was used to shape the beam into a laser sheet, which was then directed into the test-section of the flow facility. The laser light would scatter from alumina particles seeded into the flow and the scattered light was imaged by a high-framerate CMOS camera system. Each of these components will be described in detail in this section.

Optical Fiber

The solid-core fiber optic cable was 39.6 *m* long, has a 1000 μm core-diameter and is made of "Optran-UV" fiber material (manufactured by Ceram Optec). Optran-UV fiber has a pure fused silica core with a fluorine doped fused silica cladding. The cladding diameter is 1060 μm. The fiber has a laser damage threshold of 5.4 J/mm^2 (based on an assumed 1 *ms* pulsewidth) at 1060 *nm* wavelength and a numerical aperture of 0.22. It is non-solarizing, meaning it can pass light in the ultraviolet spectrum. The cable is fitted on either end with SMA-905 adaptors.

Light from the laser was coupled into the fiber via a 25.4 *mm* diameter, 100 *mm* focal-length, planoconvex spherical lens. This lens is placed such that its focal point is located slightly in front of the fiber face. This is essential as placing the focal point behind the fiber face may result in a localized beam-intensity above the fibers damage threshold. Efficient laser/fiber coupling required highly accurate alignment. As such, the input end of the fiber was mounted on a three-axis translation stage. This arrangement resulted in a coupling efficiency of 60 – 75%, depending on the laser settings (power and repetition rate).

DPSS Laser

The PLMS system utilized a Q-switched, diode-pumped Nd:YAG laser (Corona, Coherent Inc). The laser operates at repetition rates of up to 25kHz and has a peak time-averaged power output of 75W at 532nm wavelength. Its peak time-average power output is reached only when operated at 10kHz repetition rate. During the experiments conducted in this study, the laser delivered a pulse-energy of 13.9mJ or 25W time averaged power at a 1800Hz repetition rate. The laser has a 4mm diameter beam. The beam is multimodal ($M^2 \approx 25$), with a 5mrad divergence. The pulsewidth of the laser is 160ns. The combination of long pulsewidth and low per-pulse energy output makes this laser ideal for use with the fiber-coupled PLMS system at it keeps the single-pulse laser intensity well below the damage threshold of the fiber.

Sheet-forming Optics

As shown in Figure 2.8, the fiber-optic cable is brought into the drop-rig vertically through a hole at the top. Outside the drop-rig, the fiber is supported on a lightweight aluminum structure with a rounded, 470 *mm* diameter bend radius. This rounded support prevents the fiber from exceeding its minimum bend radius prior to a drop-test and acts to prevent snagging, entanglement or whiplash damage to the cable during a test. In order to prevent damage to the fiber caused by the drag shield during impact and deceleration at the end of a drop, the fiber enters the rig through a 190 *mm* long, 38 *mm* diameter bored out aluminum rod.

The layout of the sheet-forming optics is shown schematically in Figure 2.9. Inside the rig the fiber is connected to an SMA-905 fiber-optic mount, which is used to rigidly support the fiber and maintain its position before and during the experiment. The beam leaving the fiber is highly multimodal as it has an M-squared value of over 200 (Idicheria, 2004), which leads to a high far-field divergence. This rapidly expanding beam is collimated using a 50.8 *mm* diameter, 300 *mm* focal length plano-convex spherical lens. The beam is then turned 90 *deg* using a 50.8 *mm* diameter dichroic mirror in order to align it with the horizontal axis of the rig. The beam is focused using a 50.4 *mm* diameter, 300 *mm* focal length, plano-convex spherical lens and expanded into a sheet using a 25.4 *mm* wide, -50.4 *mm* plano-concave cylindrical lens. The laser sheet is directed into the test-section using 190 *mm* × 50 *mm*, rectangular, first surface mirror. All optics are mounted on optical rails made of Bosch aluminum framing using 10 *mm* T-nuts and standard 12.7 *mm* optical post mounts.

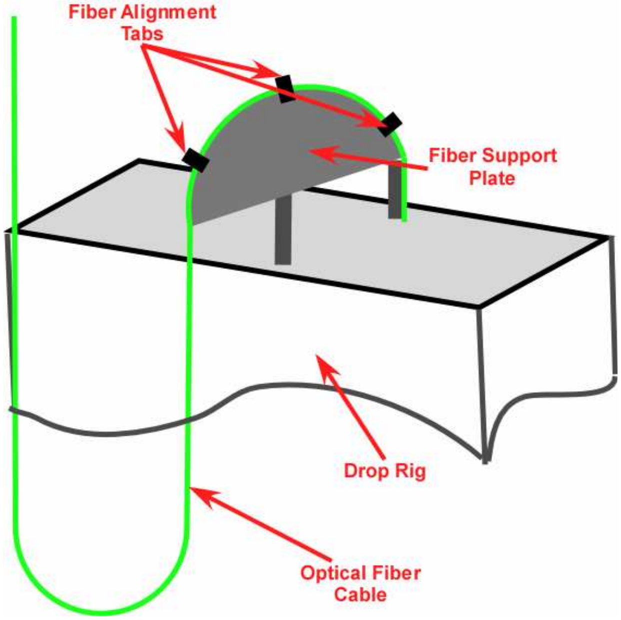

Figure 2.8 Optical fiber support and alignment structure.

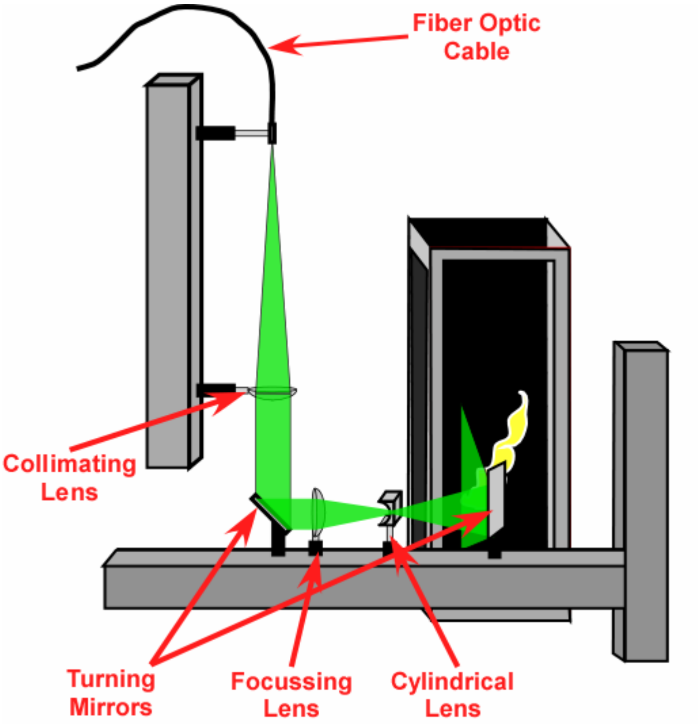

Figure 2.9 Sheet-forming optics setup.

Camera

The PLMS system uses a high-framerate camera (Fastcam-APX, Photron Inc.) for image acquisition. The camera has a 10-bit, 1024x1024 pixel, high-speed CMOS imaging array. Its pixels measure 17 *μm*, and have a 60% fill factor. When used in full-frame mode, it operates at up to 2000 *fps*. It is electronically shutterable, with an independently controllable exposure time of down to 4 *μs*. The camera was fitted with a 50 *mm*, f/1.4 Nikkor lens. Mounted in front of this lens was a 50 *mm* square colored glass filter (Schott Glass, VG-14. 1.0 *mm* thick) to reduce flame luminosity.

The camera is fully self-contained, with all electronics, memory and communications hardware mounted in small control box, which is attached to a remote head via a pair of cables. The control box is equipped with 2.6GB of on-board memory, which allows for the acquisition of up to 2048 full-frame images per run. The control box is operated from a Pentium III desktop PC located in the drop-tower via an IEEE-1394 Firewire^{TM} digital interface. Images are also downloaded from the ram memory in the control box via the Firewire^{TM} connection. The camera head and control box together weigh approximately 6.6 *kgs* and are designed to withstand a 100-g shock-acceleration for 10 *ms*, which far exceeds the requirements for use in the drop rig.

During combustion experiments the camera was electronically shuttered to 10 *μs* to reduce the background flame luminosity. This required synchronization of the camera-triggering with the laser pulses. This was accomplished by using a high-speed photodiode (DET 210, Thor Labs) to sense incoming laser pulses and to trigger a delay generator (Berkeley Nucleonics Corp. Model 500). The delay generator then sends a TTL trigger pulse to the camera approximately 5 *μs* prior to the arrival of the next pulse. The delay generator was powered by the on-board 12 *V* battery packs via a 60 *W* DC-to-AC inverter.

Seeding

In order to conduct PLMS, it is necessary to seed tracer particles into the flow. One common way to achieve this goal in the lab is through the use of a fluidized bed seeder. Unfortunately, in this and previous studies (Greenberg *et al.*, 2003) the traditional fluidized bed seeders have been seen to fail in the low-gravity environment. This was due to the particle column going unstable and producing uncontrolled and often grossly excessive particle seeding. The levels of seeding produced by a number of fluidized-bed seeders tested in the present and previous (Idicheria, 2003) studies generated particle-seeding sufficiently dense to cause image saturation and even clog the fuel lines and injectors. In order to obtain uniform, reliable seeding in micrgravity, a new type of particle-seeder had to be developed.

Shown in Figure 2.10 is a new particle-seeder designed as part of this study specifically for use in the microgravity environment. The seeder used a technique we call the impinging-jet injection (IJI) system. As its name suggests, the IJI seeder injected a jet of fuel downward into the particle column from above. The impinging jet penetrated the particle column, aerosolizing and homogenizing the upper part of it through forced recirculation. The particle-laden fuel stream exits the seeder horizontally through a fitting mounted in the side of the tube.

Although the IJI compared poorly to fluidized bed seeders in normal gravity, when used in low-gravity, it provided a much more uniform, controlled and repeatable particle-seeding. This is because the column is no longer dependent on its own weight to maintain its stability

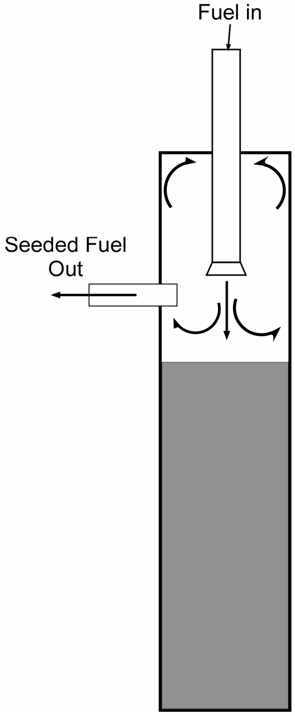

Figure 2.10 Counterflow-injection alumina particle seeder.

IMPLEMENTATION

The complexity of the experimental system required that the user carefully follow a specific procedure. A typical drop sequence in the tower went as follows. First, the on-board batteries are fully re-charged. Once this was complete, the on-board pressure vessels are charged with their respective fuels from a set of pressurized gas storage cylinders in the drop-tower. The appropriate flow-rates were set and checked with an electronic flow-meter. The seeder was then filled with alumina particles and then inserted into the fuel line. A small blast of fuel is sent into the seeder to clear any particles lodged in the lines during filling. Then the manual shut-off valves are closed and the on-board gas bottles are disconnected from the drop-tower fuel supply lines.

After a visual inspection of the optics and laser sheet is made, the on-board computer, delay generator, photodiode and camera are turned on. A toggle switch is inserted into the release-trigger circuit and set to the “ON” position. Once all systems are on, the LabView control program is initiated. Settings for the camera are input to the control-box from a desktop computer via an IEEE-1394 Firewire connection. After the Labview control program is initiated and the camera parameters set, the Firewire and Ethernet crossover cables were removed. The airbag deceleration mechanism was inflated and checked for tears. If none were found, the rig was hoisted to the top of the drop shaft.

At the top of the drop shaft, the laser is turned on and allowed to warm up and stabilize for several seconds. Next, a burning wick is inserted through a hole in the top of the rig (and drag-shield) into the test section of the flow facility. The toggle switch is then thrown from ON to OFF, initiating the first step of the drop sequence, which is to open the solenoid valves in the pressure system. The wick ignites the fuel jet and is then removed. The switch is then toggled back to the ‘ON’ position to activate the flow-facility blowers.

Finally, the cargo quick-release hook was activated and the drop-rig released. This pulls the toggle switch loose from its connector in the rig, breaking a circuit connected to the DAQ-board in the on-board computer. This signals the computer to send an output line on the DAQ-board high, activating the logic gate between the BNC timing box and the camera and thus triggering the camera. The on-board computer collects data from the pressure transducers and accelerometer for 1.3 seconds and stores the data in the RAM of the onboard computer. The program then closes both solenoid valves in order to extinguish the flame immediately after the impact. The blowers driving the flow-facility are also shut down at this point.

After the drop, the rig is removed from the airbag mechanism, its manual shutoff valves are closed and data from the pressure transducers and on-board accelerometer are downloaded from the on-board computer and checked for anomalies. The download of images from the camera into a desktop computer is then initiated. Next, the on-board computer, delay generator, photodiode and accelerometer are then turned off and the 24V battery packs are set to re-charge. The download of 2000 images from a single run takes approximately 28 to 30 minutes. After the download is complete, the camera is switched off and its batteries are set to recharge using a regulated 2A battery charger.

Chapter Three: LUMINOSITY IMAGING

Multi-kilohertz frame-rate cinematographic imaging of flame luminosity was used to study a series of transitional/turbulent jet-flames in a crossflow (JFICF) under normal- and low-gravity conditions. These time-resolved images were used to gain insight into the instantaneous large-scale behavior of the luminous regions of the JFICF. The images were also ensemble-averaged to identify average characteristics such as centerline trajectory (based on mean luminosity), spread rate and flame length.

EXPERIMENTAL CONSIDERATIONS

In this study, four JFICF cases were examined. Table 3.1 lists the flow conditions of each case studied. In all cases, the fuel jet was a mixture of 60% hydrogen to 40% propane by volume, or approximately 5% hydrogen by mass. The density of this fuel is 0.8kg/m^3. This fuel mixture produces a flame which is pale blue in the near field and a moderately bright yellow over most of the flame length. Visual inspection of each case studied revealed that the flame does not lift or detach.

Parameter	**Case** **1**	**2**	**3**	**4**
r	7	8.5	10	11.5
Re	3350	4070	4780	5500
$\mathbf{u_j}$ **(m/s)**	11.3	13.7	16.1	18.5
$\mathbf{u_{cf}}$ **(m/s)**	1.3	1.3	1.3	1.3
ξ_L **– 1g**	6.17	5.48	5.02	4.56
ξ_L **– 0.01g**	1.24	1.13	1.04	0.98

Table 3.1 Experimental conditions for cinematographic flame luminosity imaging

Fully time-resolved, cinematographic digital imaging was used to study each of the four flames in normal and low-gravity. The images were captured at 3000 *fps*, with a 50 μs exposure time. The resolution of the camera at this framerate was 1024 × 512 pixels. In order to capture the entire flame in a single image, it was necessary to use a short focal length (12 *mm*) C-mount CCTV lens. Although this lens caused some vignette effects because of its small aperture and its short focal length caused some barrel distortion, the net effect of these potential problems was minimized by using only the center region of the image. The aperture of the lens was fixed at f/8 for all cases.

Although the lens settings were locked in place by using locking screws on both the focusing ring and on the aperture, a set of ruler and calibration images were taken before and after each three-drop run. Comparison of these images confirmed the field of view and plane of focus in all four cases remained the same (to within one pixel) from drop to drop. The flow-rate of the fuel was measured before and after each drop with an Omega Model FVL-1608 laminar flow-element electronic flow-meter. These tests confirmed the repeatability of the initial jet-exit conditions from one run to the next.

INSTANTANEOUS IMAGES

Figures 3.1 and 3.2 show sample images taken from two low-gravity JFICF experiments. The images have been psuedo-colored to increase contrast and improve their display. The purpose of these figures is to familiarize the reader with the terminology that will be used in later sections when discussing the various characteristics of these flames.

Figure 3.1(a) shows a sample image from the low-gravity $r = 7$, $Re = 3350$ case. In this image, at least four large-scale luminous structures are visible, including the relatively dim one towards the near-exit region of the flame. From what we know of the flow-field of a JICF, it seems clear that these luminous structures correspond to the shear-layer structures discussed in the literature survey in Chapter 1. This figure also illustrates how the low relative-luminosity of the flame in the near-exit region affects this imaging experiment. To the eye this region is a dim blue. It is also important to note once more although the dynamic range of the imaging system was insufficient to capture this dim-bluish region, all four flames studies remained attached (non-lifted).

The flame-luminosity images shown in Figures 3.1 and 3.2 are cropped on the top and bottom so that the field of view corresponds to the locations of the upper and lower edges of the imaging windows. They are cropped on the right hand side such that they correspond to the wall opposite the injector. The left-hand sides of the images are cropped slightly to the left of the test-section so as to better show the location of the injector. As noted in Chapter 2, the width of the test section is 203 *mm*, or 64 jet-exit diameters. The length of the imaging window was 375 *mm* or approximately 120 jet-exit diameters.

The jet issues horizontally into a vertical crossflow. As such the side of the jet facing the lower and right-hand side edges of the imaging window correspond to the windward-side and those facing the injector wall correspond to the leeward-side. These regions are labeled in Figure 3.1(a) and Figure 3.2(a) for clarity. Henceforth, this terminology will be used to when referring to these regions of the jet.

The instantaneous flametip-location is defined as the point in a single luminous flame image furthest downstream of the injector and still visible (based on an intensity threshhold, as will be discussed later). The mean luminous flame shape is shown overlaid on top of the instantaneous images shown in Figures 3.1(b) and 3.2(b).

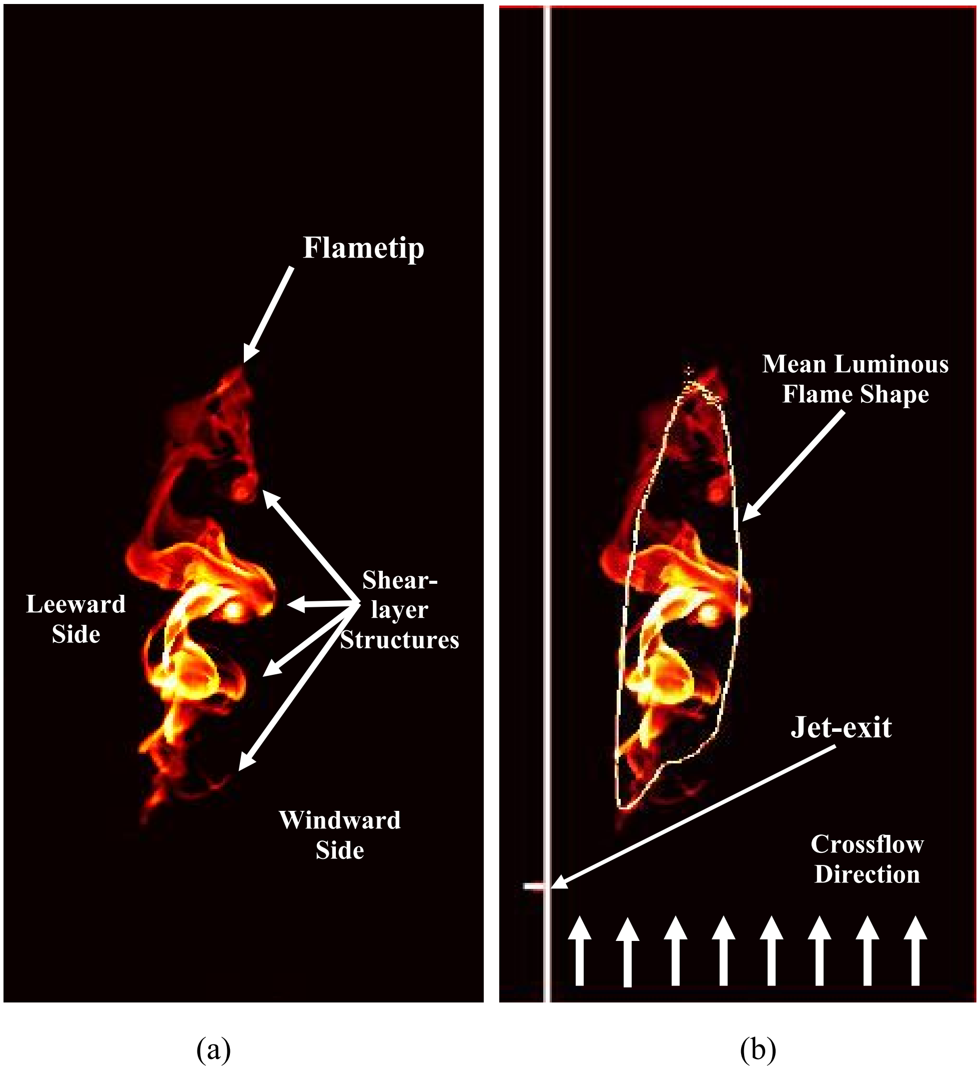

(a) (b)

Figure 3.1 Sample JFICF image (r = 7, Re = 3350 case) showing (a) characteristic luminous shear-layer structures and (b) overlaid with lines showing the relative locations of the injector, wall, mean luminous flame shape and crossflow direction. Both images have been cropped on the right-hand side to correspond to the location of the wall opposite the injector (203 *mm*, or 64 jet-exit diameters across from injector wall). The top and bottom of the images were cropped to the length of the front imaging window (375 *mm* or approximately 120 jet-exit diameters).

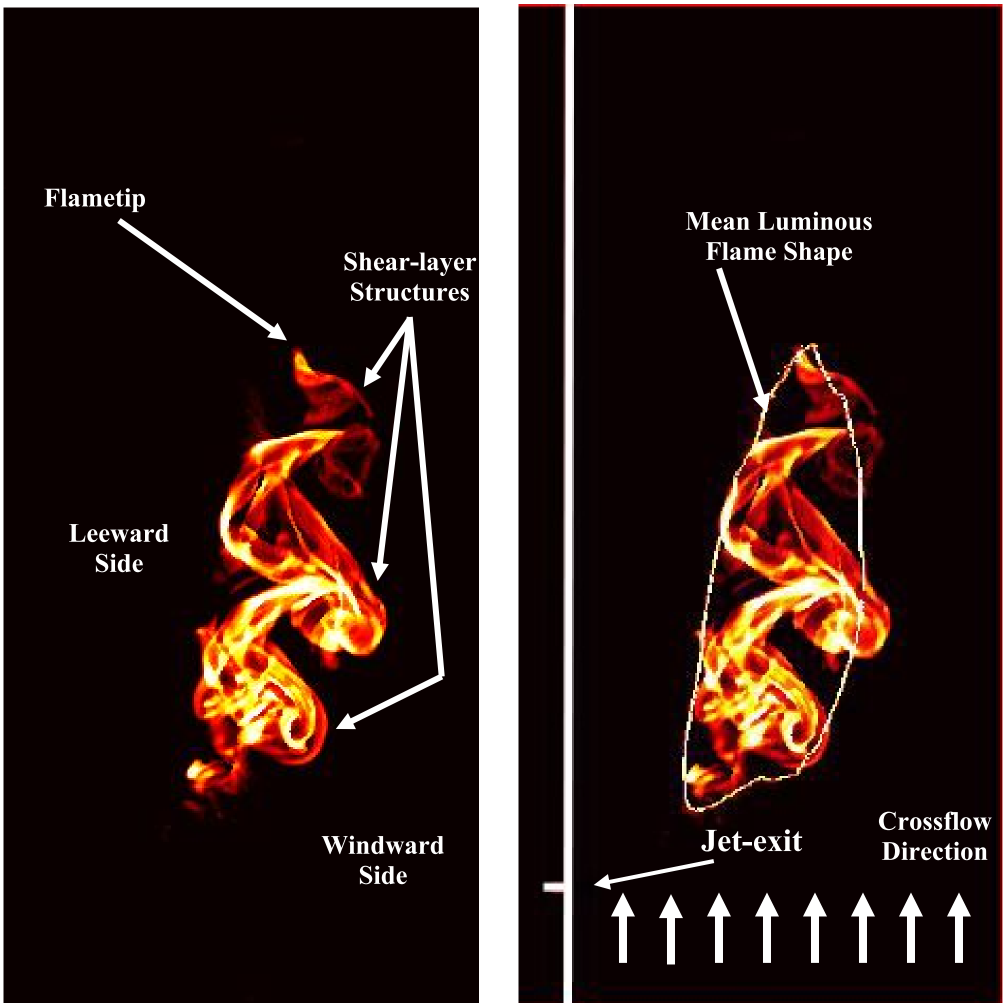

(a) (b)

Figure 3.2 Sample JFICF image (r = 11.5, Re = 5500 case) showing (a) characteristic luminous shear-layer structures and (b) overlaid with lines showing the relative locations of the injector, wall, mean luminous flame shape and crossflow direction. Both images have been cropped on the right-hand side to correspond to the location of the wall opposite the injector (203 *mm*, or 64 jet-exit diameters across from injector wall). The top and bottom of the images were cropped to the length of the front imaging window (375 *mm* or approximately 120 jet-exit diameters).

Figures 3.3 - 3.6 show a series of sample image sequences taken at various conditions. The images were pseudo-colored for improved contrast/visualization. The time between frames for each case shown is 3.33 *ms*, which corresponds to one tenth of the actual frame-rate of the camera during an experiment. It is clear from these image sequences that the large-scale luminous flow-structures are fully time-resolved. The images are cropped in the same fashion as Figures 3.1 and 3.2.

Elongation and Distortion of Luminous Flame

Comparing Figure 3.3 ($r = 7$, low-gravity case) with Figure 3.4 ($r = 7$, normal-gravity case) it is clear that the buoyancy has an observable effect on the instantaneous large-scale luminous structure of the JFICF. As can be seen from the image sequence of Figure 3.3, the low-gravity flames tend to remain of relatively uniform width with downstream distance. As can be seen from the arrows overlaid on the images (which follow the downstream convection of a typical shear-layer structure in the flame) even when luminous structures separate from the main body of the luminous flame, the overall width of the luminous flame zone remains relatively uniform with downstream distance. This uniformity of luminous flame width is quite consistent throughout the downstream region until burn-out occurs at the flame-tip.

The corresponding flames show a different behavior in normal-gravity. As can be seen in the image sequences of Figure 3.4, the normal-gravity flames show a clear tendency to thin-down and elongate with downstream distance and tend to reach an almost filamentary appearance close to the flame-tip. They do not appear to maintain the same uniformity of luminous flame width with downstream distance as their low-gravity counterparts. An example of this thinning-down and elongation of the flame is marked by the arrows overlaid on the on the image sequences shown in Figure 3.4. It should be noted that this thinning-down and apparent elongation of the luminous flame is a transient (rather than steady-state) phenomenon. In the image-sequence of Figure 3.4a there appears to be a correlation between the convection of a large-scale luminous structure through the luminous flame zone and the thinning down and elongation of the luminous flame. Observation of the dynamics of this shear-layer vortex / flame-elongation phenomenon is impeded by the spatially-integrated nature of flame-luminosity image. However it appears from this image sequence that the shear-layer vortex itself it being distorted in the vertical direction, going from approximately circular in shape, to almost linear near the flame-tip.

Figures 3.3 and 3.4 also show significant differences in burnout characteristics for the same momentum flux ratio and jet-exit Reynolds number. The tendency of the low-gravity flames to maintain a relatively uniform luminous flame-width with downstream distance lasted up to and including burnout of the flametip. At the flame-tip of the low-gravity JFICF, the flame begins to dim relatively uniformly across the width of the flame before finally disappearing. Convection velocity of the luminous flame-tip appears similar to that of the fluid immediately below it. The tendency of the normal-gravity flames to thin-down and elongate also appears to be inextricably linked to the nature of its flame-tip burn-out. Although it is not immediately obvious from the image sequences of Figure 3.4, close inspection of the movie sequences from which these images were taken reveals an apparent acceleration of the flametip away from the main body of the flame as burnout occurs. This gives the flametip the appearance of being torn away from the main body of the luminous flame rather than simply convecting downstream with it.

A close examination of the image-sequences of the high momentum-flux ($r = 11.5$, $Re = 5500$) JFICF in Figure 3.5 and Figure 3.6 (low- and normal-gravity case, respectively) reveals similar though less pronounced characteristics. Just as in the lower-momentum flux case, the low-gravity images show a wider flame with a more uniform luminosity across the width of the flame. The normal-gravity case (Figure 3.6a and b) shows a similar elongation of the flame luminous flame-tip.

The differences between the normal- and low-gravity flames at this higher momentum-flux ratio (and jet-exit Reynolds number) are not as obvious as in the lower momentum-flux case. It appears in the image sequences of Figure 3.6 that the main body of the luminous flame in normal-gravity tends to maintain a more uniform luminosity across its width with downstream location that did the lower-momentum flux ratio JFICF shown in Figure 3.4. The flametip still shows a tendency to thin-down and elongate with downstream distance but this no longer appears to be a feature of the majority of the luminous flame zone. It should be noted here once more that this thinning down and elongation is not a universal normal-gravity burnout characteristic. It can be seen in the first six images of the sequence shown in Figure 3.6a that the flame dims relatively uniformly across the visible flame width and burns out without significant elongation. None of the low-gravity flames however, appear to display the elongation and distortion sometimes seen in normal-gravity flames. It appears, based on these flame-luminosity image-sequences, that the instantaneous large-scale luminous structure of the normal- and low-gravity flames are approaching a similar state, suggesting that in this case the flame is approaching a momentum-dominated limit.

It is illuminating to note here a significant resemblance between the image sequences of Figures 3.3 - 3.6 and the luminosity images of normal- and low-gravity, straight turbulent hydrocarbon jet-flames shown in Idicheria *et al.* (2004). Despite the major differences between the flow-fields of a turbulent non-premixed straight jet-flame and a turbulent JFICF, the image sequences show obvious similarities.

For example, Idicheria *et al.* (2004) shows time-resolved images sequences of a piloted, straight propane jet-flame in normal and low-gravity. The jet-exit diameter (1.75 *mm*) and Reynolds number (*Re* = 8500) of the flame in are roughly comparable to those of the present study. The flames in the image-sequences appear to show a thinning-down and elongation with downstream distance very similar to that seen in Figure 3.3 and 3.4. The flame-tip burnout characteristics also bear a striking similarity to the images in the present study, with the low-gravity flames showing a tendency to dim uniformly across the width of the jet before disappearing. The normal-gravity images in that study show a similar tendency to those in the present study in that their flame-tips appear to accelerate away from the body of the luminous flame before burning out. The lower Reynolds number flame-luminosity image sequences in Idicheria *et al*. (2004) show less similarity to those of Figure 3.3 - 3.6 of the present study. Given the lower jet-exit Reynolds number (*Re* = 2500, methane fuel) and lack of a crossflow in those flames though, it is reasonable to expect to a more laminar looking flame.

Idicheria *et al.* (2004) attribute the observed characteristics of the aforementioned image sequences to the competition between convection and diffusion in their flame. According to their interpretation of the images, the elongation of the flametip is caused by an increased downstream velocity caused by buoyancy-induced downstream acceleration of the flow. This increased convection velocity is thought to decrease the relative importance of molecular diffusion in the downstream mixing characteristics and thus cause the flame to thin-down in the downstream location. They see this phenomenon over a range of jet-exit Reynolds numbers ranging from 2000 to 10,500 and ξ_L = 3.7 – 12 (in normal-gravity).

It appears that once the (horizontal) jet has turned largely in the direction of the (vertical) crossflow, its luminous flame characteristics begin to mimic some of those found in the straight vertical jet. Given the similarity of flow-conditions at the jet-exit, together with the strong similarity of the instantaneous image sequences between this study and that of Idicheria *et al.* (2004), it seems their interpretation of the flame-tip behavior would provide a reasonable explanation of the flame-characteristics observed in Figure 3.3 - 3.6. This conjecture is supported by the fact that in both the present study and that of Idicheria *et al*. (2004), the thinning-down and elongation of the flametip occurs in the same direction with respect to the gravity vector. The image sequences of Figure 3.4 and 3.6 appear to provide clear evidence of buoyant acceleration of the luminous flame-tip, which leads in turn to the previously discussed elongation and thinning-down characteristics of the luminous flame.

Beyond noting the buoyant acceleration-induced thinning and elongation of the flame-tip, Idicheria *et al.* (2004) conclude from their work that one of the net effects of gravity on straight turbulent jet-flames is the disruption of the Kelvin-Helmholtz instability governing the large-scale structure of their flow-field. This conclusion was based on a range of parameters in their data including flame-tip oscillations, instantaneous images, RMS luminosity fields. Again, their interpretation appears to provide a reasonable starting point for interpreting the phenomena seen in Figures 3.3 - 3.6. In particular, a buoyancy-induced disruption of the Kelvin-Helmholtz instability could potentially explain the previously noted distortion of the shear-layer vortices in the (low-momentum, normal-gravity) JFICF images shown in Figure 3.4a. Although the straight jet-flames of the Idicheria *et al.* (2004) study did not have directly comparable JFICF shear-layer vortices (and certainly no counter-rotating vortex pair or wake vortices for that matter) the buoyant acceleration associated with heat-release could have a similarly destabilizing influence upon the flow. The fact that the observed shear-layer vortex distortion occurs in the direction of the gravity vector makes such an interpretation appear reasonable.

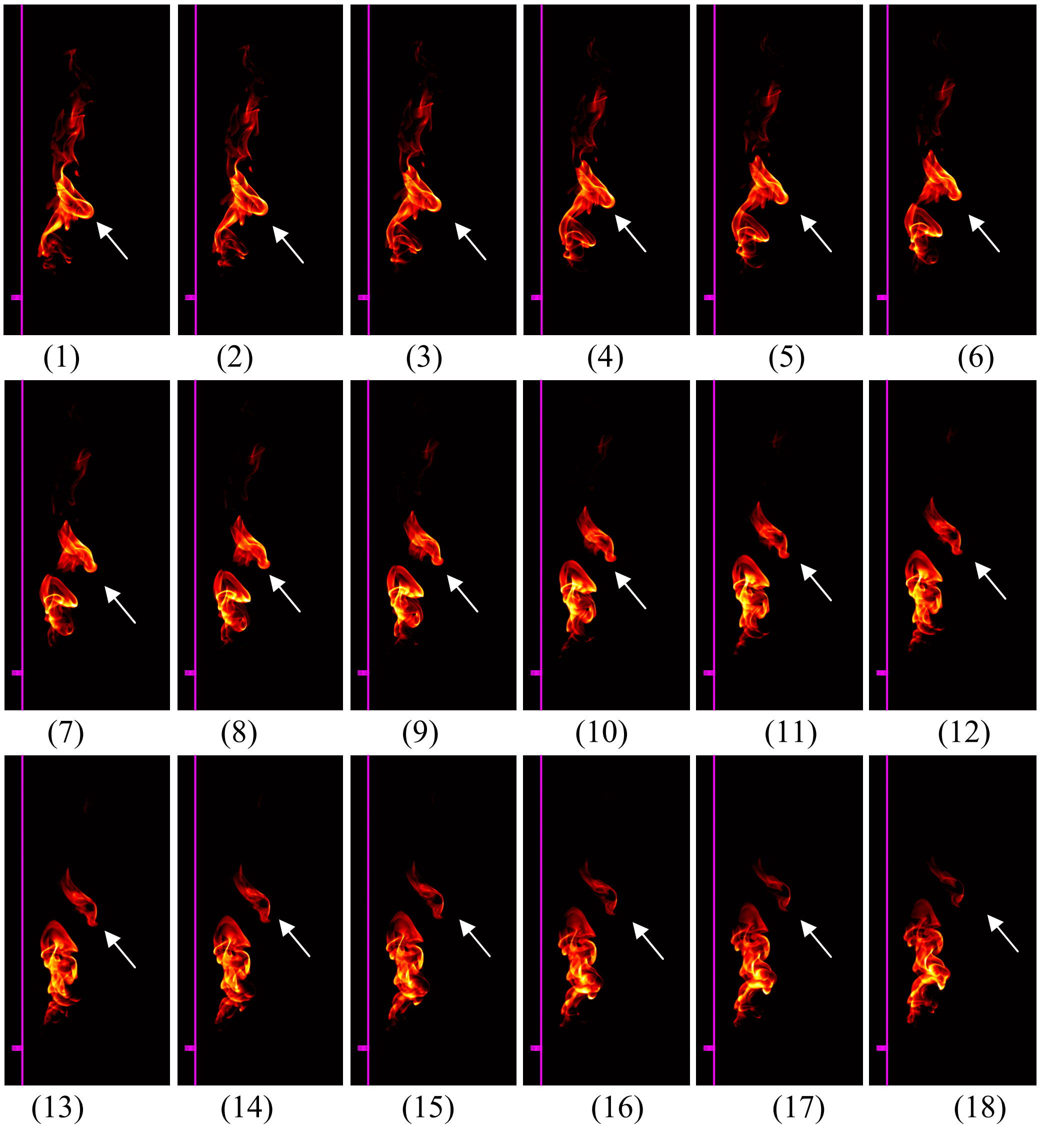

Figure 3.3(a) Cinematographic image sequence of natural flame luminosity for low-gravity JFICF with r = 7, Re = 3350. Time between frames is 3.33 ms (corresponding to every tenth image acquired during an experiment run). 50 μs exposure-time. Arrows follow the downstream convection and burnout of a typical large-scale luminous structure. Note how the structure convects downstream without apparent acceleration with respect to the rest of the luminous flow. Note also how the structure dims uniformly across its width as it burns out.

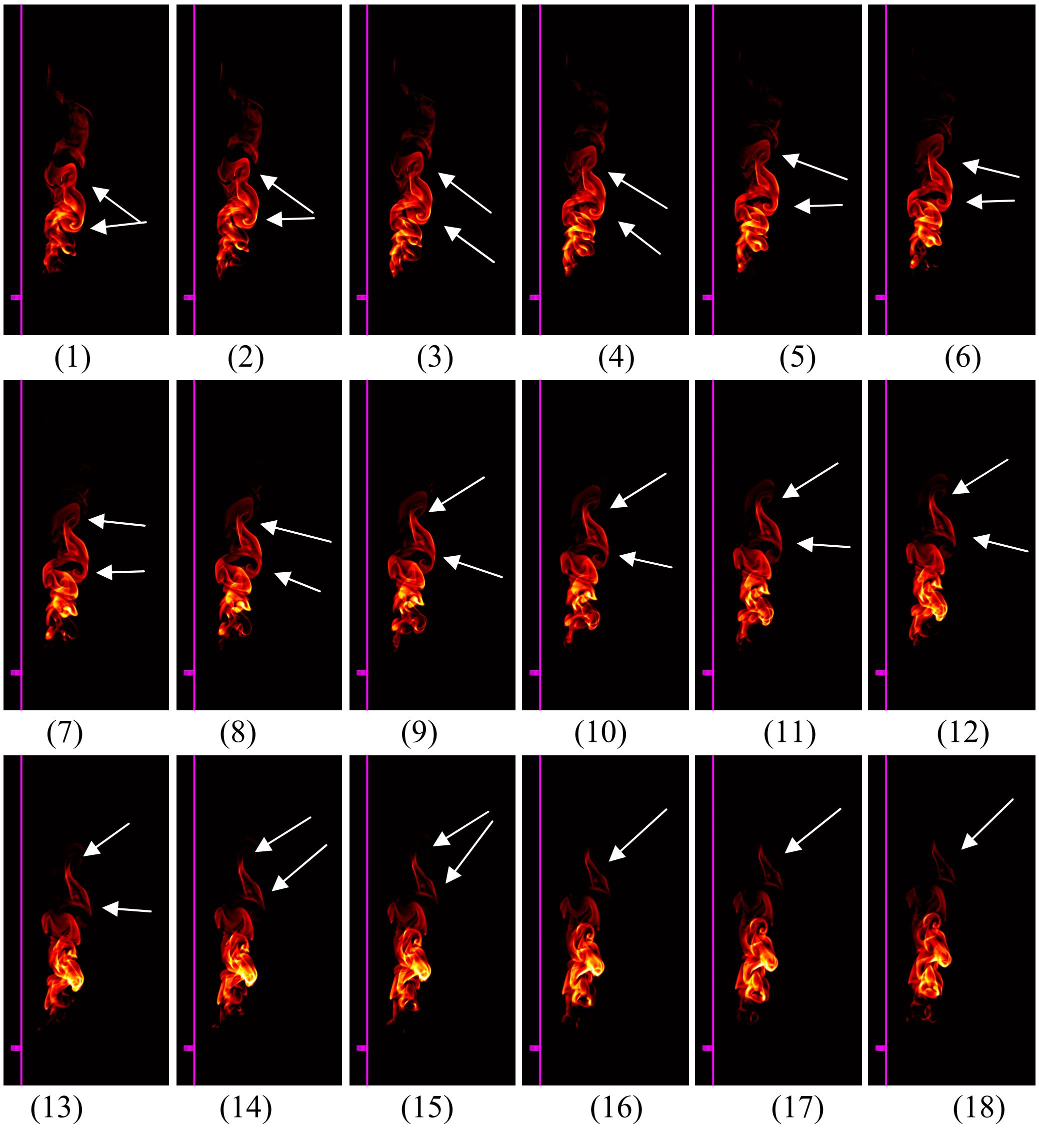

(1) (2) (3) (4) (5) (6)

(7) (8) (9) (10) (11) (12)

(13) (14) (15) (16) (17) (18)

Figure 3.3(b) Cinematographic image sequence of natural flame luminosity for low-gravity JFICF with $r = 7$, $Re = 3350$. Time between frames is 3.33 *ms* (corresponding to every tenth image acquired during an experiment run). 50 μs exposure-time. Arrows indicate the roll-up and burnout of a pair of shear-layer structures in the flow. This structure does not appear to accelerate with respect to the rest of the flow as it separates and burns out. It also dims uniformly across its width as it burns out. This characteristic is typical of low-gravity flametip burnout but not so in normal-gravity.

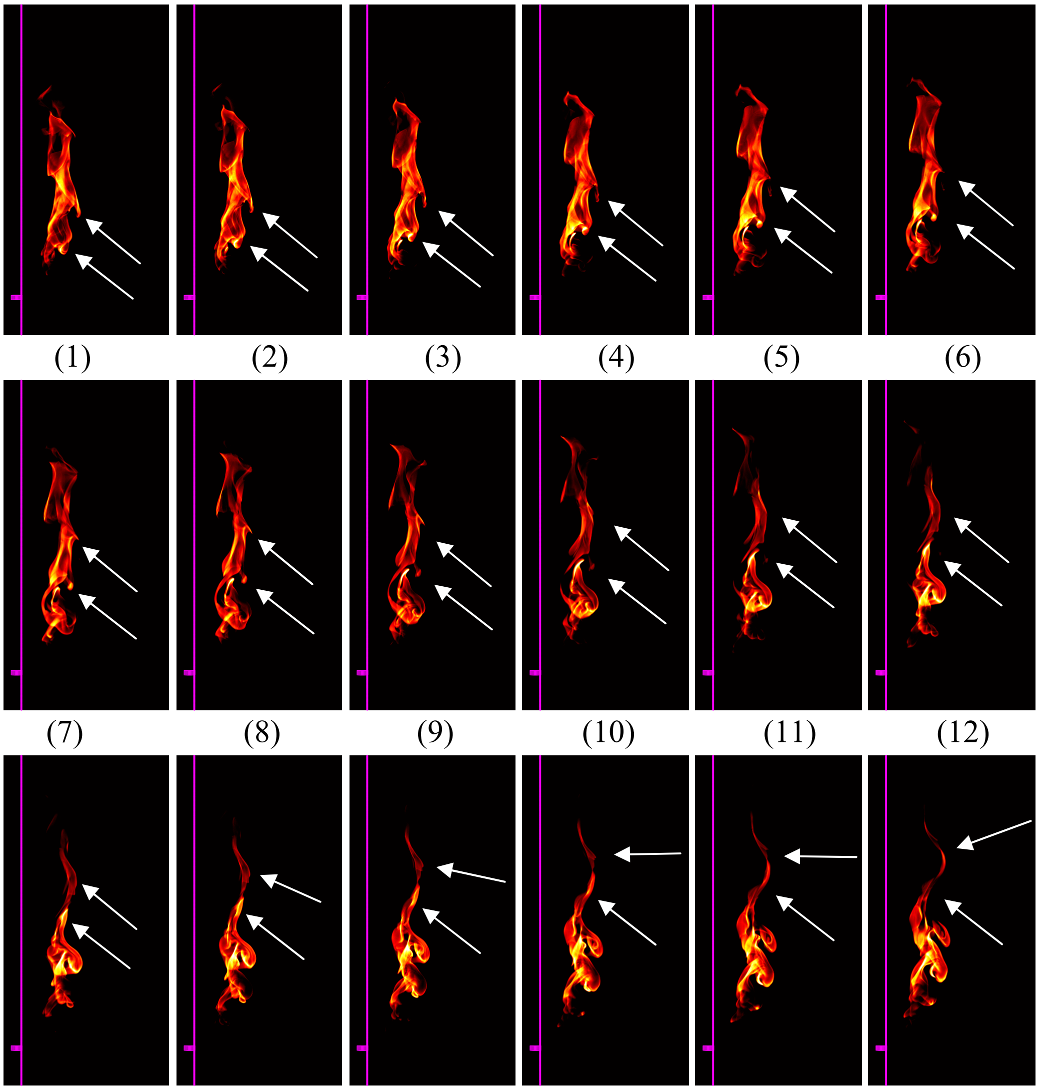

(1) (2) (3) (4) (5) (6)

(7) (8) (9) (10) (11) (12)

(13) (14) (15) (16) (17) (18)

Figure 3.4 (a) Cinematographic image sequence of natural flame luminosity for normal-gravity JFICF with $r = 7$, $Re = 3350$. Time between frames is 3.33 ms (corresponding to every tenth image acquired during an experiment run). 50 μs exposure-time. Arrows show the thinning down and distortion luminous structure as flow nears the flame time.

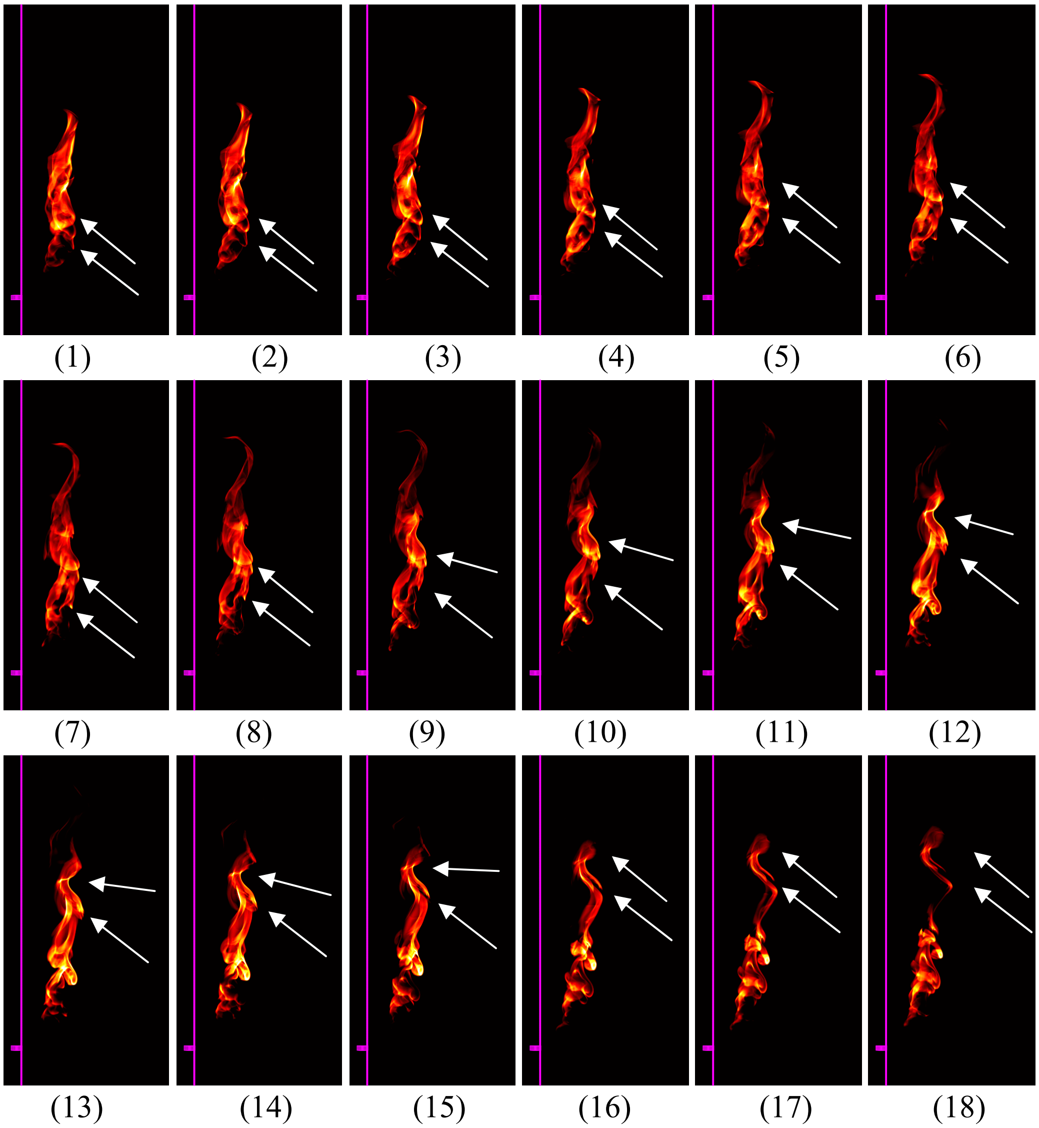
(1) (2) (3) (4) (5) (6)
(7) (8) (9) (10) (11) (12)
(13) (14) (15) (16) (17) (18)

Figure 3.4(b) Cinematographic image sequence of natural flame luminosity for normal-gravity JFICF with r = 7, Re = 3350. Time between frames is 3.33 *ms* (corresponding to every tenth image acquired during an experiment run). 50 *μs* exposure-time.

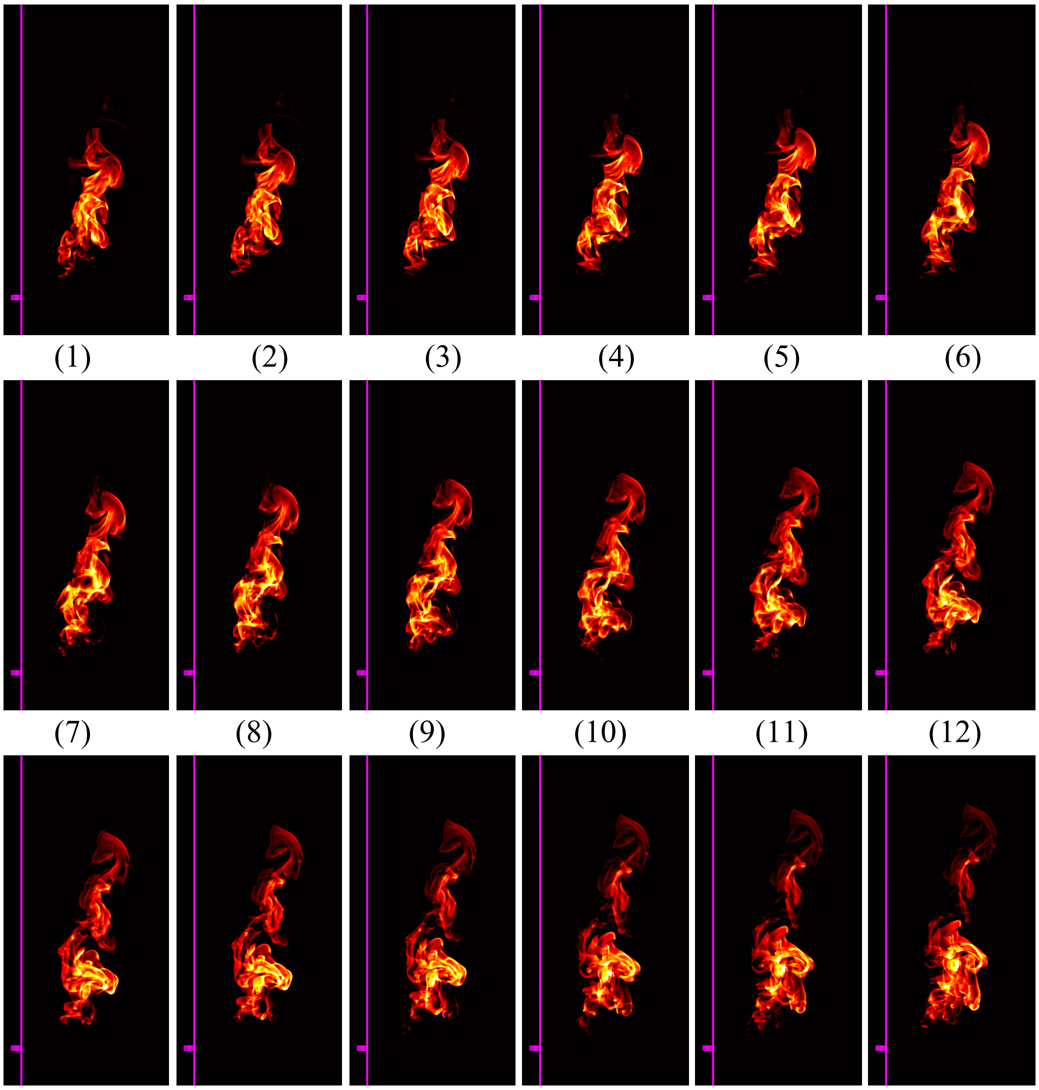
(1) (2) (3) (4) (5) (6)
(7) (8) (9) (10) (11) (12)
(13) (14) (15) (16) (17) (18)

Figure 3.5(a) Cinematographic image sequence of natural flame luminosity for low-gravity JFICF with r = 11.5, Re = 5500. Time between frames is 3.3 *ms* (corresponding to every tenth image acquired during an experiment run). 50 *μs* exposure-time.

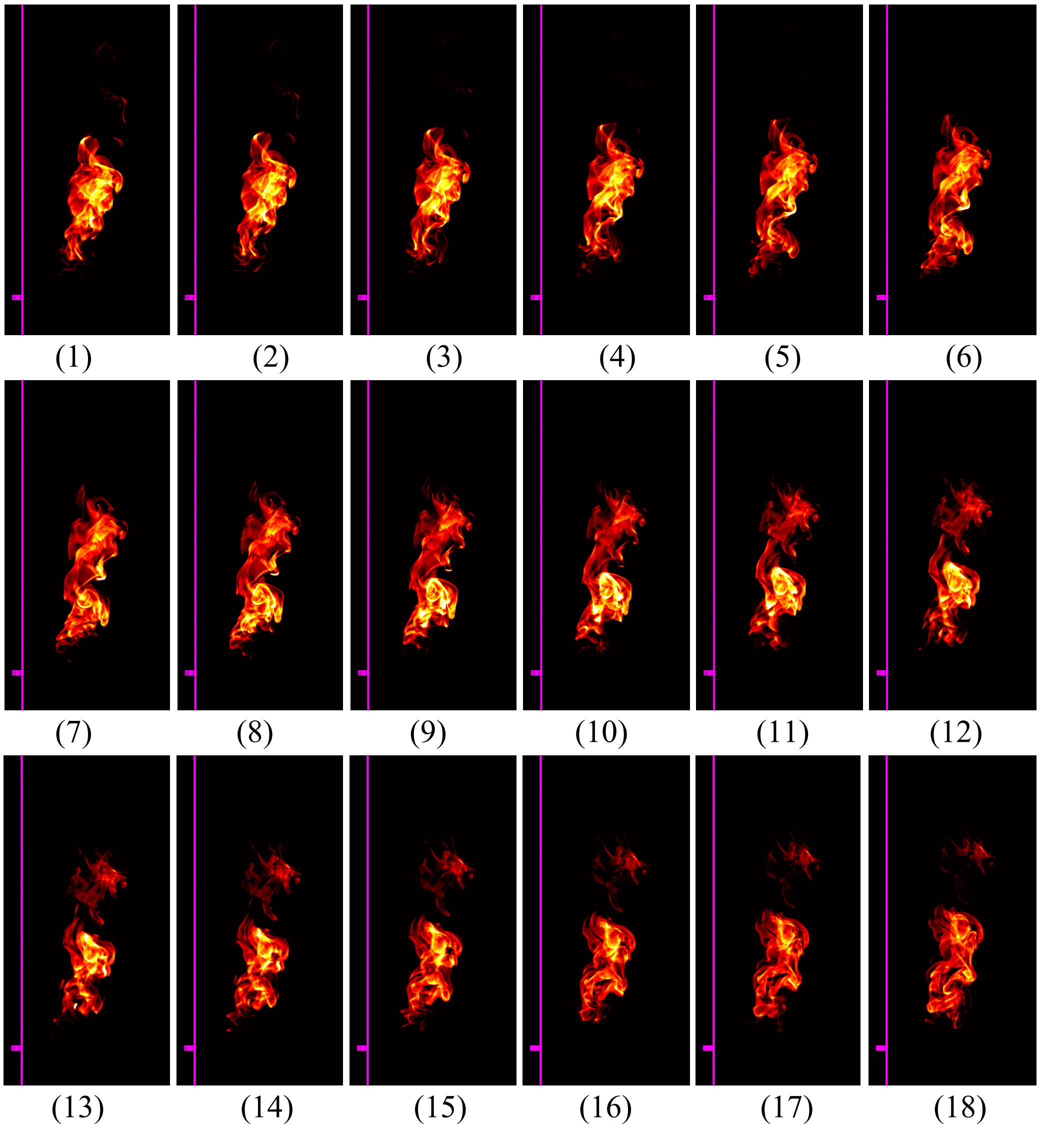

(1) (2) (3) (4) (5) (6)

(7) (8) (9) (10) (11) (12)

(13) (14) (15) (16) (17) (18)

Figure 3.5(b) Cinematographic image sequence of natural flame luminosity for low-gravity JFICF with r = 11.5, Re = 5500. Time between frames is 3.33 *ms* (corresponding to every tenth image acquired during an experiment run). 50 μs exposure-time.

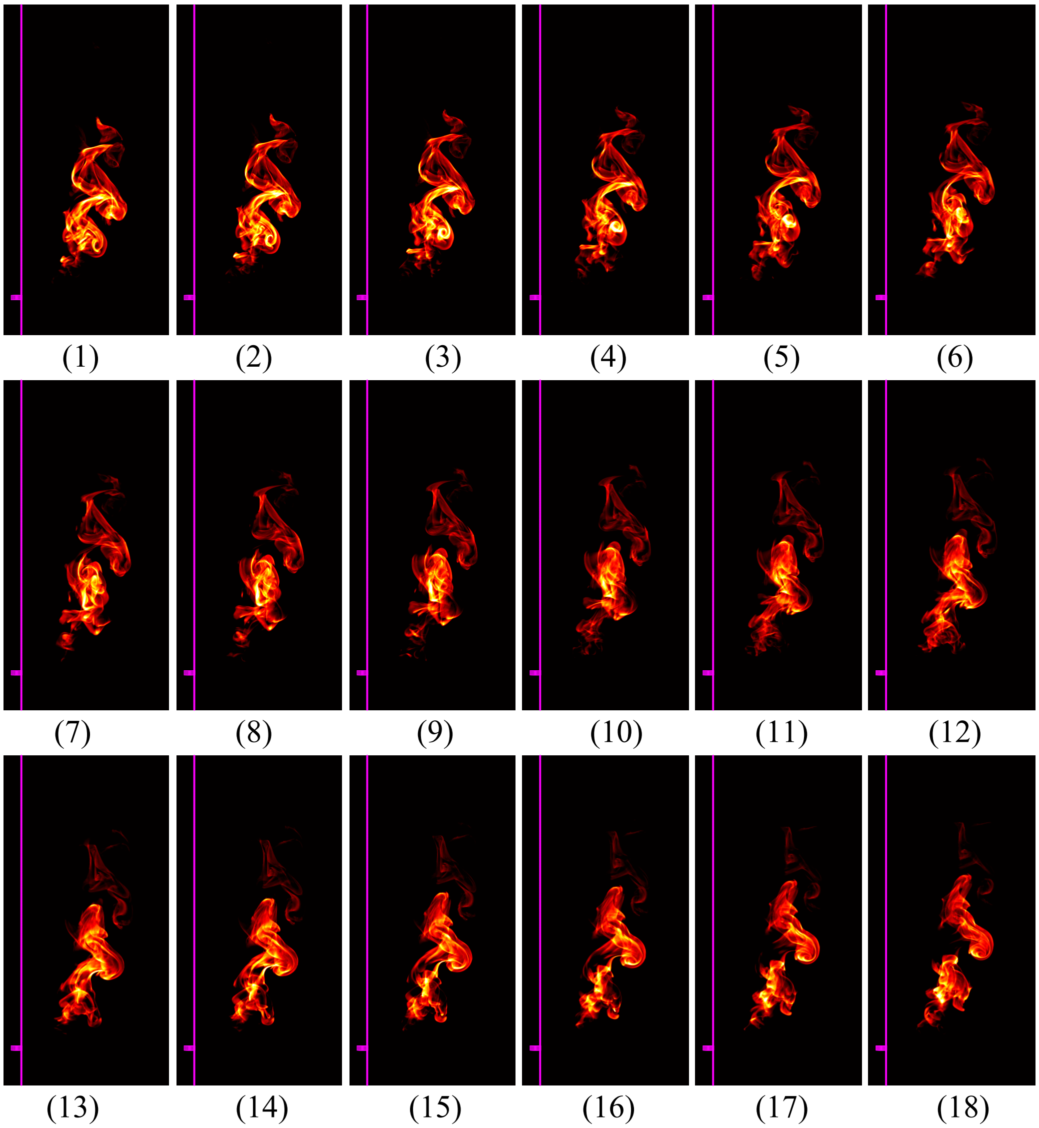

Figure 3.5(c) Cinematographic image sequence of natural flame luminosity for low-gravity JFICF with r = 11.5, Re = 5500. Time between frames is 3.33 ms (corresponding to every tenth image acquired during an experiment run). 50 μs exposure-time.

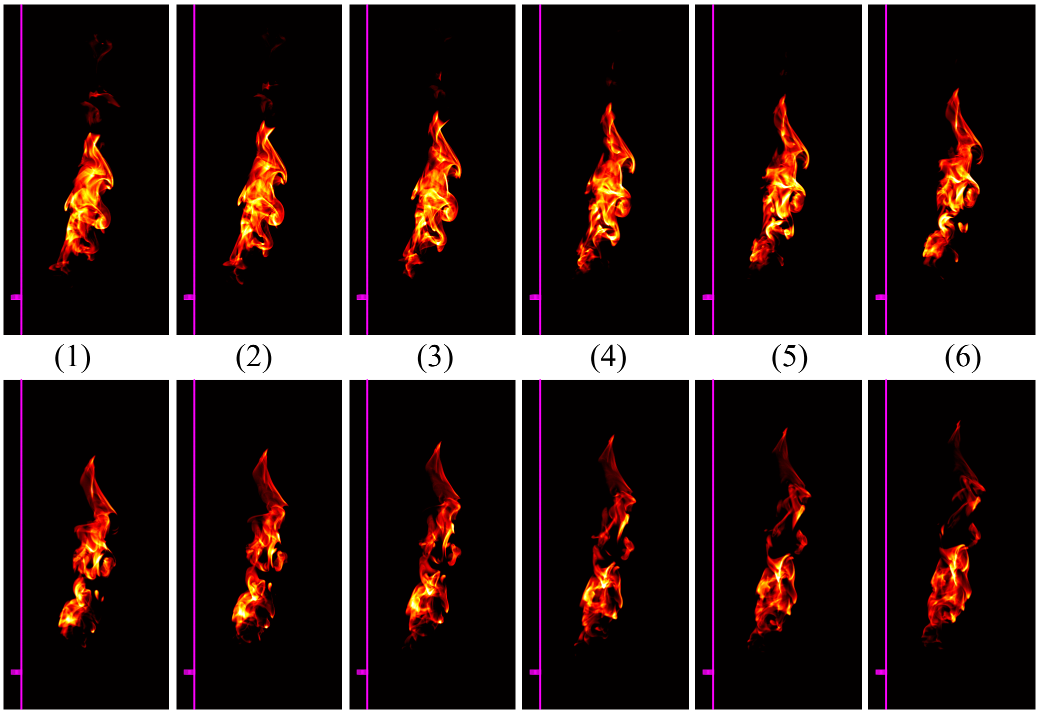

(1) (2) (3) (4) (5) (6)

(7) (8) (9) (10) (11) (12)

Figure 3.6(a) Cinematographic image sequence of natural flame luminosity for normal-gravity JFICF with r = 11.5, Re = 5500. Time between frames is 3.33 *ms* (corresponding to every tenth image acquired during an experiment run). 50 μs exposure-time.

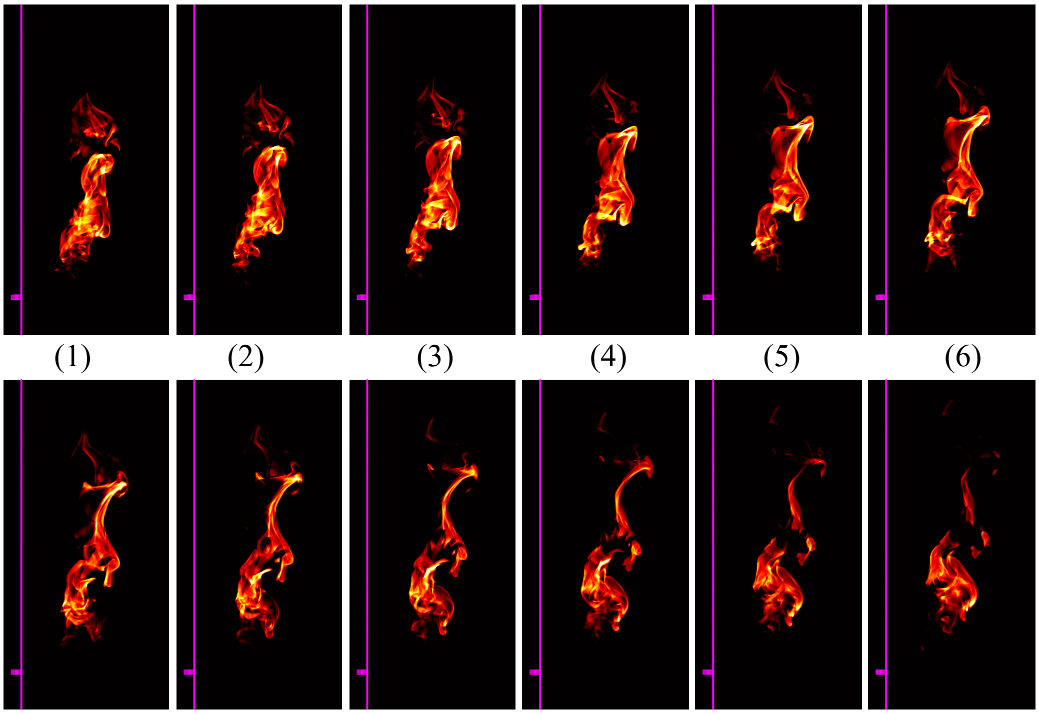

(1) (2) (3) (4) (5) (6)

(7) (8) (9) (10) (11) (12)

Figure 3.6(b) Cinematographic image sequence of natural flame luminosity for normal-gravity JFICF with r = 11.5, Re = 5500. Time between frames is 3.33 *ms* (corresponding to every tenth image acquired during an experiment run). 50 μs exposure-time.

MEAN AND RMS CHARACTERISTICS

Mean and RMS luminosity images were computed from the first 2700 images (0.9 *s*) gathered in each drop. As the time-scale over which these images were collected is relatively small, it was thought appropriate to check the convergence of the mean with each frame of the ensemble-average. This was done by comparing summation of the total difference in pixel-intensities of the mean-image at each step of the computation of the ensemble average. The residual was defined as $\sum_i \sum_j \{\bar{I}_n(i,j) - \bar{I}_{n-1}(i,j)\}$where $\bar{I}_n(i,j)$ is the ensemble average of the images (1 to *n*), at pixel location (i, j). Figure 3.7 shows a plot of one representative residual decay, plotted with frame number *n*. Since the magnitude of the residuals over first few frames was significantly larger than the later frames the first several residual points are not shown in this plot. The residuals plot was normalized with respect to the first maximum in the profile.

Judging from the decay of the residuals shown in Figure 3.7, it seems reasonable to conclude that the ensemble-average luminosity image is well converged at the end of the 0.9 *s* of images averaged for each experiment run. Indeed, it appears from this plot that the magnitude of the fluctuation in the residuals has decayed to within less than 10% of the max within the first 1200 frames (~0.44 *s*) and continues to decay thereafter.

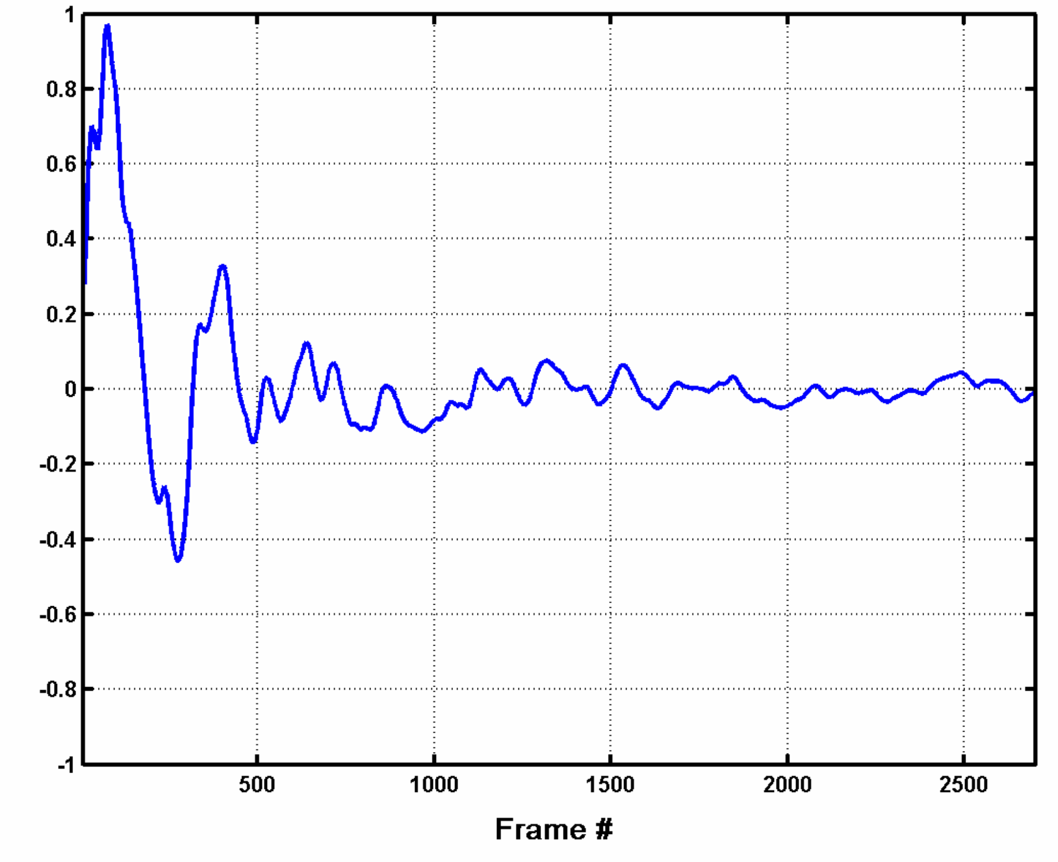

Figure 3.7 Sample residual decay from calculation of ensemble average of flame luminosity image sequence. This trace does not show the first several residual points (per text) as they were significantly larger than the later points. The residual data was normalized with the first local maximum. Note, the trace above was sub-sampled for improved display and thus does not appear (to the eye) to reach a numerical value of unity at the point of the first maximum.

Observations

Sample mean luminosity images for each normal and low-gravity case are shown in Figure 3.8. These images are displayed with a full-scale contrast stretch and false-colored to highlight low-intensity regions of the mean flame-shape and the fore-aft asymmetry of the mean-luminosity profile (to be discussed shortly). Also shown (as points of reference) in the images are the location of the flow-facility wall and the injector nozzle. As previously mentioned though, the flame was fully attached in all cases. The dim, bluish portion of the flame in the near-field does not appear in the images due to its low relative luminosity; i.e. the dynamic range of the camera was not sufficient to capture both the highly luminous sooting region and (much-dimmer) near field region.

Several interesting features stand out in the mean images. In all cases, the flame luminosity is clearly biased towards the leeward side of the JFCIF. Both the magnitude and gradient of mean luminosity are visibly higher on the leeward side of the jet. This observation is consistent with the observations of Birch *et al*. (1989) and Kadota *et al*. (1990), who measured higher mean temperatures on the leeward side of turbulent JFICF. The Kadota study attributed this to the behavior of the increased rate of mixing and chemical reaction induced by vortex motion of the lee-ward side of the JFICF. A frame-by-frame inspection of the image sequences suggests the lower windward-side luminosity may be due in part to the intermittency of jet/crossflow fluid in the imaging region. The noticeably greater penetration of non-reacting crossflow air into the jet on the windward side (compared to the leeward) is evidently also a contributing factor in the biasing the mean luminosity towards the leeward side.

Figure 3.9 shows the mean luminous flame shape for each of the cases studied. In this study, the edge of the mean luminous flame shape is defined as the iso-contour where mean luminosity drops to 15% of the peak value for a given case. From these images it is clear that in all cases, the luminous flame zone is significantly wider in low-gravity than in normal-gravity. The widening of the luminous flame zone of transitional and turbulent nonpremixed jet-flames and JFICF as one goes from normal- to low-gravity has been observed in several previous studies (Bahadori *et al.*, 1993, Hegde *et al.*, 1994, Idicheria *et al.*, 2001, Boxx *et al.*, 2003).

A logical explanation of this phenomenon lies with competition between convection and molecular diffusion in non-premixed jet flames. As noted previously, in their study of transitional and turbulent nonpremixed jet-flames, Idicheria *et al.* (2004) argued that greater convection velocity due to buoyant acceleration in the vertical direction decreased the relative importance of molecular diffusion in the straight vertical jet flame compared to in low-gravity and thus resulted in thinner mean luminous flameshapes. It seems logical that a similar argument can be made to explain the observed widening of mean luminous flame shape of JFICF in low gravity.

If one assumes that the observed distortion and elongation of the luminous structures in normal-gravity is associated with a local buoyancy-induced acceleration of the flow, then one would expect the large-scale convection velocity to increase. This increase in convection velocity would decrease the relative importance of molecular diffusion in the flow. One likely outcome of the increased relative importance of molecular diffusion in low-gravity would be an increase in local flame-width.

The flame-shape images of Figure 3.9 also show a trend of increasing luminous flame-width with increasing momentum flux ratio. This trend is apparent in both the normal- and low-gravity cases. This observation is consistent with previous observations of normal-gravity JFICF (Kalghatgi, 1983, Rao and Brzustowski, 1982, Kadota *et al.*, 1990). Kadota *et al.* (1990) interpret an increase in flame-width with velocity ratio in terms of the decreasing influence of crossflow velocity upon the mixed-ness of the wake-region of the JFICF. According to this interpretation, a higher crossflow-velocity (relative to the jet) enhances the rate of fuel-air mixing in the wake region and results in a decreased flame width. This interpretation would explain the observed broadening of the luminous flame zone with *r* seen in both the normal- and low-gravity flames.

It can also be seen in Figure 3.9 that the mean luminous flame-shapes of the lower-momentum JFICF show a noticeable difference towards the flame-tip. Whereas in normal gravity the mean luminous flame shape comes to a relatively sharp point at the tip, in all cases the low-gravity flames tend to have a more even, rounded shape. The mean normal- and low-gravity flame-tip shapes are more similar at higher momentum flux ratios (and jet-exit Reynolds number), suggesting the cause of the more pointed flame-shape is buoyancy-related. One possible explanation for the more pointed flame-shape in normal-gravity is the aforementioned difference in burnout characteristics between buoyant and non-buoyant JFICF. Whereas buoyant JFICF tend to stretch, elongate and burn out in a more filamentary fashion, the non-buoyant ones tend to burn out more uniformly. The increased intermittency of luminous combustion products in the buoyant JFICF (relative to its low-gravity counterpart) arising from this difference would produce such an effect on the mean.

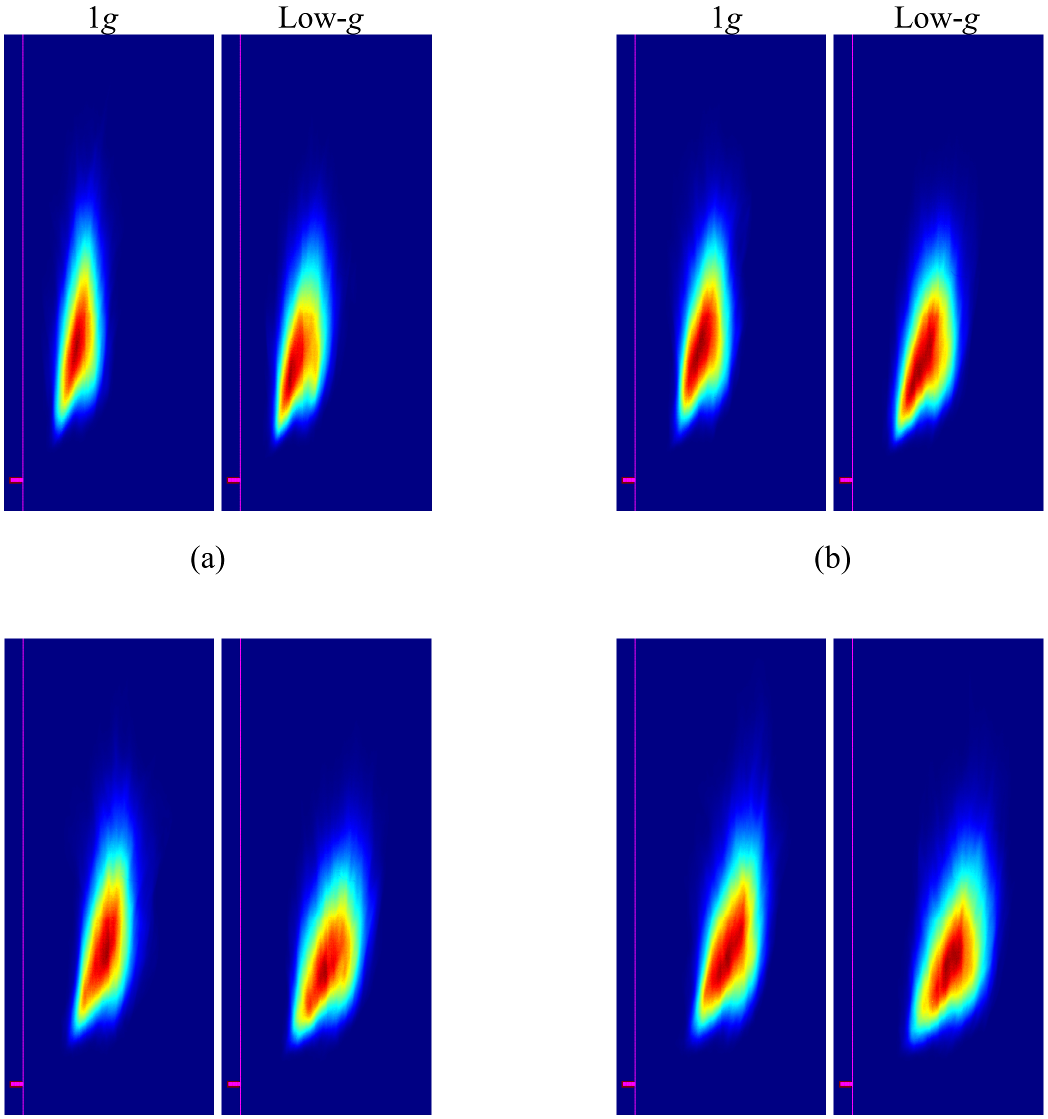

(a)

(b)

(c)

(d)

Figure 3.8 Sample mean (hydrogen-propane JFICF) luminosity images. Left-hand-side images correspond to normal-gravity and right-hand-side ones to low-gravity. a) r = 7, *Re* = 3350. b) r = 8.5 *Re* = 4070 c) r = 10, *Re* = 4800 d) r = 11.5, *Re* = 5500

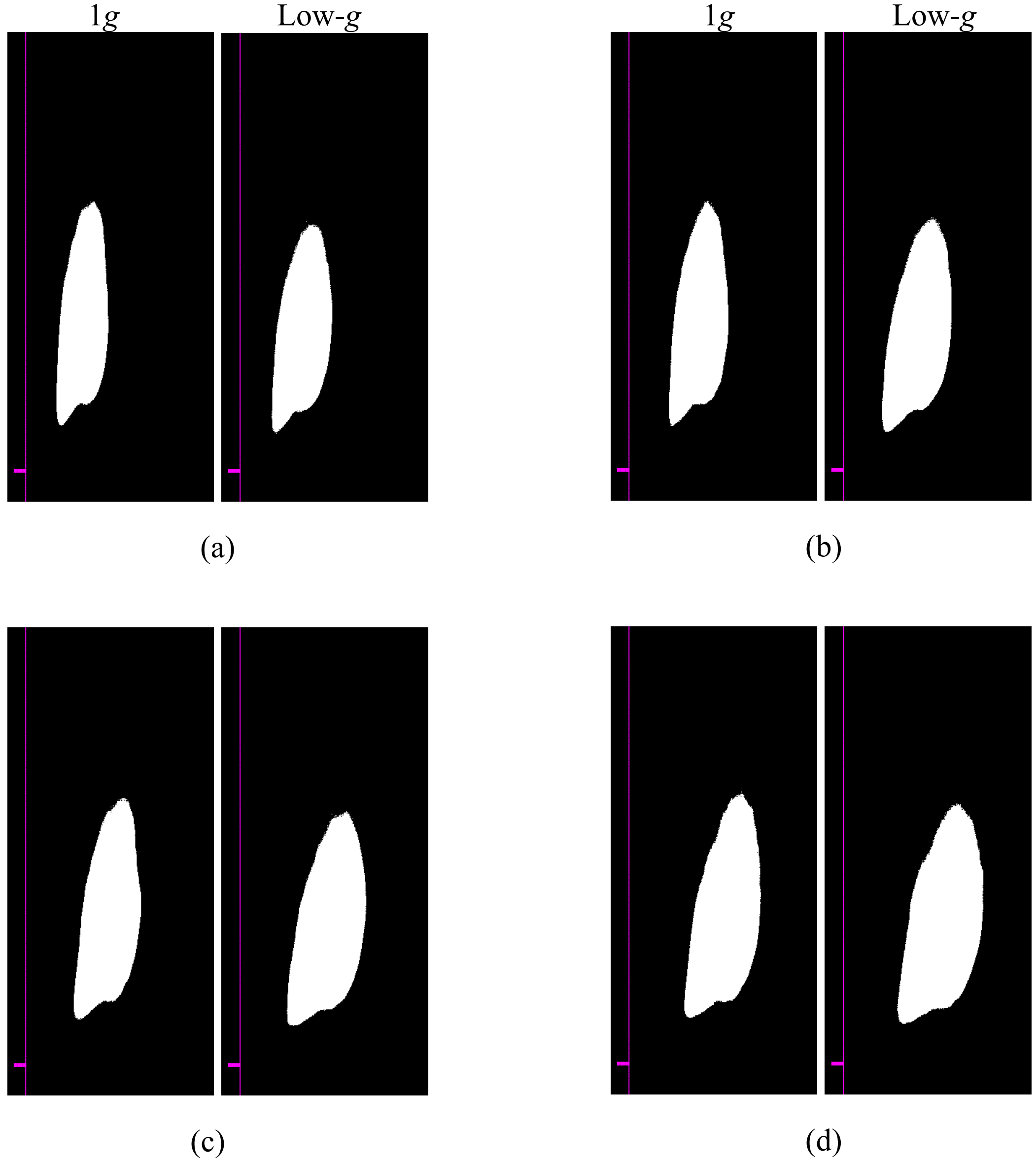

(a) (b) (c) (d)

Figure 3.9 Luminous flame shapes based on 15% iso-contour of mean luminosity. Left-hand-side images correspond to normal-gravity and right-hand-side ones to low-gravity. a) $r = 7$, $Re = 3350$. b) $r = 8.5$, $Re = 4070$ c) $r = 10$, $Re = 4800$ d) $r = 11.5$, $Re = 5500$

Flame Lengths

The mean visible flame lengths of the JFICF were determined based on the ensemble average images using the definition of Kalghatgi (1983). As shown in Figure 3.10, the flame-length is defined as the straight-line distance between the jet-exit and the visible flame-tip as determined by an intensity threshold. Broadwell *et al.* (1984) used the same definition, calling it the flame "chord length". In this case the intensity threshold was specified as 15% of the maximum ensemble-average luminosity for a given experiment run. It was necessary to use the straight-line or "chord length" definition as the near-field of the flame is not captured in the luminosity images. The use of this definition also has the useful characteristic of allowing direct comparison of the current data to the extensive JFICF visible flame-length measurements presented in Kalghatgi (1983).

It has been noted by previous researchers that the visible flame-length is an ambiguous measure which tends to generate flame-lengths longer than the stoichiometric surface. Becker and Yamazaki (1978) defined L_t, the 'thermal flame length' for a straight turbulent jet flame as the downstream distance wherein r_m (the radial location of maximum temperature) equals zero, *i.e.* where the maximum temperature falls on the centerline of the jet. They found that this "thermal flame length" typically fell near the location of maximum centerline temperature. They found the thermal flame-length did not correspond to the visible flamelength but ranged anywhere from $L_t = 0.44L$ to approximately $L_t = 0.62L$, where L is the visible flame-length. Although Becker and Yamazaki (1978) do not relate their thermal flame lengths directly to the stoichiometric flame length, if one makes the assumption that local mean flame temperature peaks near the location of stoichiometric mixture fraction, it is clear that the visible flame-length measure significantly over-predicts the stoichiometric flame length.

The way in which the visible flame length itself is defined also introduces a degree of variability into the measurement. It has also been noted that flame-lengths based on the instantaneous location of the visible flame-tip tend to be significantly higher than those based on the maximum downstream location of a mean luminous flame shape (found from either an ensemble-average of instantaneous flame-luminosity images or a single long-time exposure image). The difference in flame lengths arises from the billowing of the flame and the frequent separation of the flame-tip from the main body of the luminous flame zone (Ibrahim *et al*., 1985). With these limitations in mind, the flame luminosity is useful in identifying trends and examining large-scale luminous flame structure, without attempting to link it directly to the stoichiometric flame length.

Figure 3.11 shows a plot of the straight-line flame lengths, normalized with the jet-exit diameter and jet-exit Reynolds number. The flame lengths of the normal-gravity JFICF show no discernable variation with increasing momentum flux ratio. The low-gravity JFICF however, do appear to show a very modest (≈ 10%) increase in visible flame length with jet-exit momentum flux ratio over the range of conditions studied. A similar trend is seen in the data of Rao and Brzustowski (1982) and Bandaru *et al.* (2000) in a roughly overlapping range of momentum flux ratios. The trend is inconsistent with the measurements of Brzustowski *et al*. (1975) of a turbulent hydrogen JFICF and acid-base, "liquid-flame" JICF measurements of Broadwell *et al.* (1984), which show a decrease in flame length with increasing momentum flux ratio. The reason for the difference is not known but a possible explanation for the difference may be found in the theoretical work of Fairweather *et al*. (1991) and Karagozian (1986). These two studies suggest that flame-lengths only decrease with increasing momentum flux ratio until a certain threshhold is passed, at which point the flame length begins to increase. The data of Brzustowski (1975), Broadwell *et al.* (1984) and Tsue *et al*. (2000) support this theoretical work. It is therefore possible that the increasing visible flame length is connected with the range of momentum flux ratios chosen for this study.

It is also possible that the observed increase in flame length with momentum flux ratio is a Reynolds number effect. As the crossflow velocity is held constant in this study, increasing momentum flux ratios correspond to increasing jet-exit Reynolds numbers. It is well-established (Kuo, 1986) that laminar and transitional vertical jets flames are particularly sensitive to increasing Reynolds number and the relatively low jet-exit Reynolds numbers of the JFICF in this study (3350 – 5500) overlap the transitional regime of vertical straight jet-flames. Such an explanation for the flame-length variation does not seem persuasive however, given that the aforementioned study of Rao and Brzustowski (1982) showed a similar trend in propane flames with Re = 18,200 - 43,400. Bandaru and Turns (2000) showed a similar trend in propane flames of $Re > 14{,}000$ with crossflow velocity 2.3 *m/s* and $Re > 33{,}000$ with crossflow velocity 4.3 *m/s*. Thus it seems unlikely the variation is a Reynolds number effect.

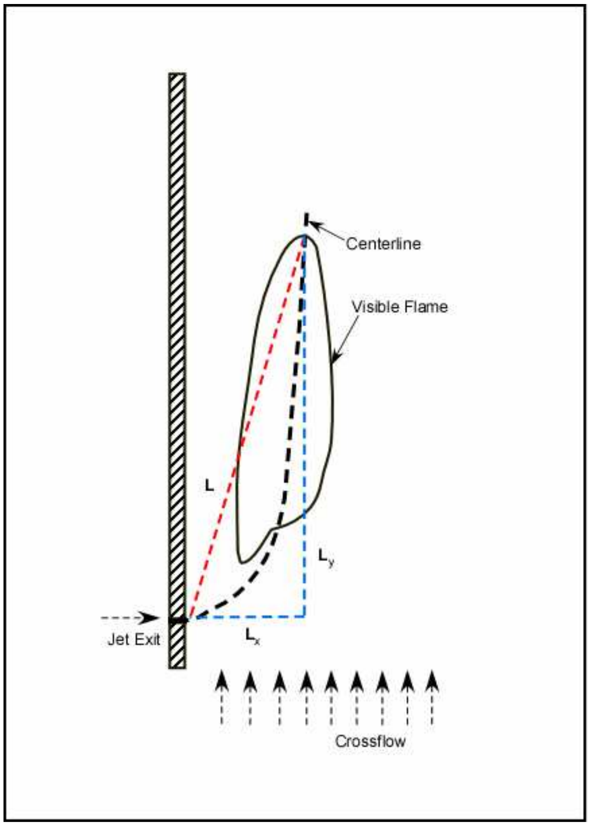

Figure 3.10 Definition of visible flame length. Straight-line distance between the jet-exit and visible flametip (based on 15% mean intensity threshold). Based on Kalghatgi (1983).

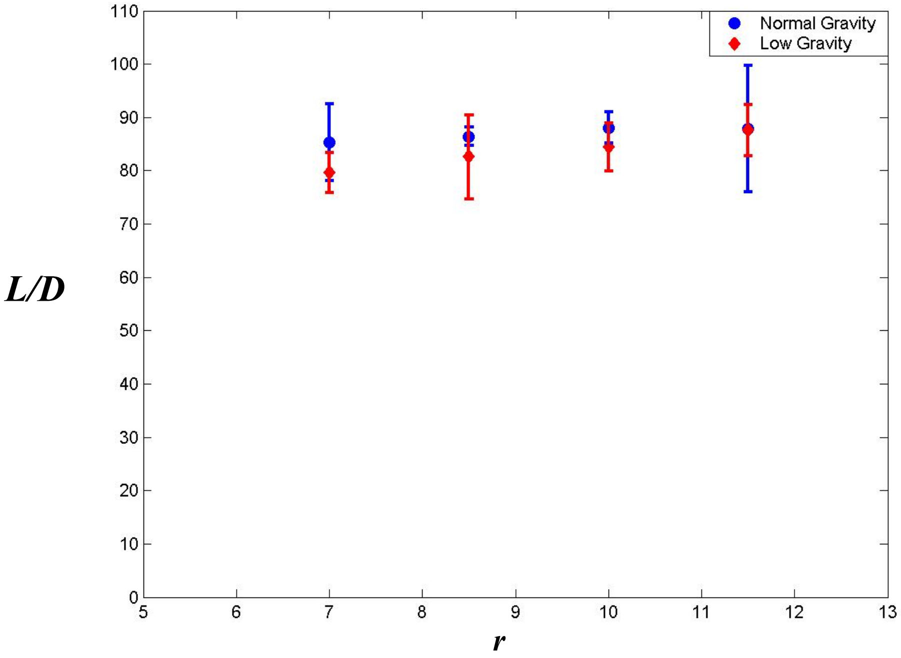

(a)

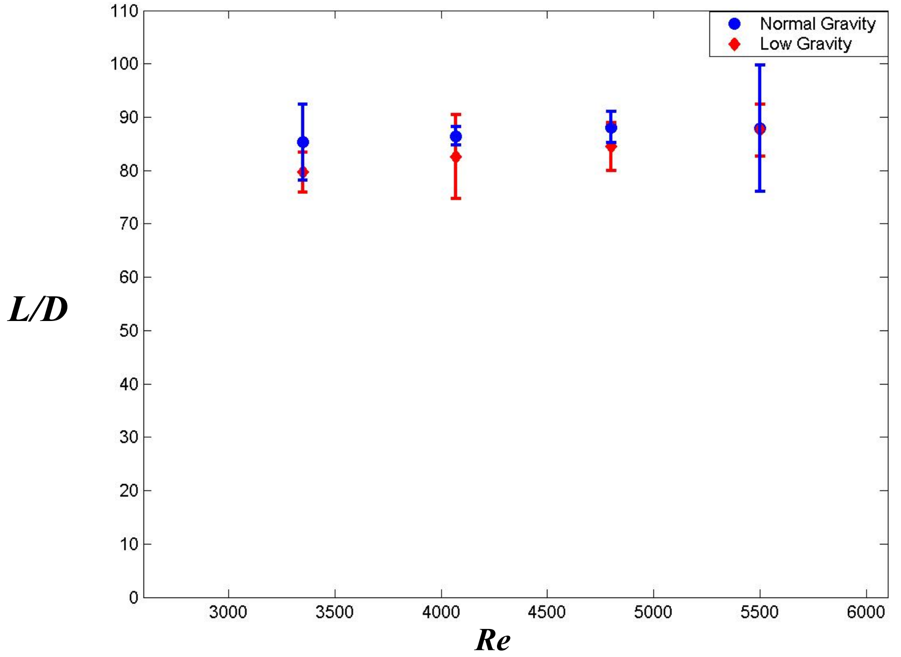

(b)

Figure 3.11 Flame-lengths, nondimensionalized by jet-exit diameter, plotted against (a) momentum flux ratio and (b) jet-exit Reynolds Number

The penetration (in both the jet- and crossflow-direction) of the visible flame was compared to the correlation for flame penetration given in Kalghatgi (1983). Although the Kalghatgi (1983) correlation attempts to match various properties of turbulent JFICF over a wide range of momentum flux ratios with a single scaling relation and is based on data taken at significantly higher jet-exit Reynolds number ($\approx 10^4$ - 10^5) and larger jet-exit diameters (6 – 22 *mm*), it does appear to provide a useful dataset for comparison due to its overlapping range of momentum flux ratios and stoichiometric mixture fractions. Kalghatgi (1983) studied hydrocarbon fuels (methane, ethylene, propane and butane) with stoichiometric mixture fractions ranging from 0.055 to 0.064. The stoichiometric mixture fraction of the fuel (60% H_2 / 40% C_3H_8) used in this study was 0.056. His correlations (based on the velocity ratio $R = u_{\mathrm{cf}}/u_{\mathrm{j}}$ and source-diameter $D_s = \mathrm{d}(\rho_j/\rho_{cf})^{1/2}$) are based on best-fit curves for data over the range $0.02 < R < 0.25$. This corresponds to a momentum flux ratios ranging from $r = 3 – 37$ (for methane) to $r = 6 – 71$ (for butane).

The results of this comparison are listed in Tables 3.2 – 3.4. The maximum difference between predicted and observed jet-direction penetration is approximately 10%. The y-direction (i.e., crossflow direction) penetration length prediction was less accurate, giving discrepancies of up to approximately 16%. The straight-line penetration length differed by a similar amount. Such differences are not unreasonable given the range of stoichiometric mixture fractions the Kalghatgi (1981) correlation attempts to match with a single curve-fit based on source-diameter and velocity ratio. The over-prediction of the Kalghatgi scaling relations is consistent with the well-known flame-shortening effect hydrogen-dilution has on turbulent hydrocarbon jet-flames (Choudhuri *et al.*, 2003).

r	L_x/D_s (Measured)	L_x/D_s (Predicted)	% Difference
7	28 ± 3.5 (Low-g)	29	-3.4
	26 ± 2.9 (1-g)		-10.3
8.5	34 ± 2.5	33	3.0
	30 ± 0.9		-9.1
10	40 ± 6.8	37	8.1
	38 ±3.6		2.7
11.5	44 ± 0.8	41	7.3
	43 ± 2.3		4.9

Table 3.2 Comparison of measured visible flame penetration (in x-direction) with scaling correlation of Kalghatgi (1983). Note, the data of Kalghatgi (1983) contains considerable spread due to the wide range of *r*, *Re* used in that study, making a direct comparison of trends more difficult.

r	L_y/D_s (Measured)	L_y/D_s (Predicted)	% Difference
7	96 ± 4.6 (Low-g)	116	16.4
	103 ± 9.2 (1-g)		11.2
8.5	97 ± 9.5	113	14.2
	104 ± 2.4		8.0
10	98 ± 5.6	109	11
	104 ± 4.5		4.8
11.5	100 ± 6.5	105	4.8
	105 ± 9.2		0

Table 3.3 Comparison of measured visible flame (in y-direction) with scaling correlation of Kalghatgi (1983). Note, the data of Kalghatgi (1983) contains considerable spread due to the wide range of *r*, *Re* used in that study, making a direct comparison of trends more difficult.

r	L/D_s (Measured)	L/D_s (Predicted)	% Difference
7	100 ± 4.7 (Low-g) 107 ± 9.0 (1-g)	120	16.7 10.8
8.5	103 ± 9.8 108 ± 2.1	118	12.7 8.4
10	106 ± 5.6 110 ± 3.7	115	7.8 4.3
11.5	109 ± 6.1 109 ± 14.8	113	3.5 3.5

Table 3.4 Comparison of measured straight-line flame with that predicted by scaling relations of Kalghatgi (1983). Note, the data of Kalghatgi (1983) contains considerable spread due to the wide range of *r*, *Re* used in that study, making a direct comparison of trends more difficult.

It is noteworthy that the Kalghatgi correlation produces as close an approximation to the current data as it does. The correlation does not account for buoyancy, is based on a different configuration of JFICF (with a vertical jet in horizontal crossflow) and uses velocity ratio where a momentum flux ratio may be more appropriate. Thus, while buoyancy does indeed affect the centerline trajectory (as will be shown in the following section) it does not appear to be the dominant parameter governing jet / crossflow interaction in these flames.

Judging from Figure 3.11 it seems clear that any difference in the visible flame length of the JFICF between normal- and low-gravity is relatively minor, suggesting that buoyancy does not play a dominant role in determining visible flame length under the conditions tested in this study. The similarity in visible flame lengths in normal- and low-gravity is consistent with the work of Idicheria *et al.* (2004), who found the visible flame-lengths of transitional/turbulent hydrocarbon jet-flames (of similar jet-exit Reynolds number, *Re* = 2000 – 10,500) to be largely unaffected by buoyancy. It is also consistent with the study of Hermanson *et al.* (2004), which focused on turbulent, pulsed ethylene / O_2-enriched air straight jet-flames but also showed measurements for an unpulsed flame at $Re = 5000$ in normal and low-gravity. That study showed very little difference in flame length between normal and low-gravity. The similarity in normal- and low-gravity flame lengths contrasts with the results of Bahadori *et al.* (1993), which show a significant increase in visible flame length for straight turbulent jet-flames in low-gravity compared to normal-gravity over a similar range of Reynolds numbers ($< \approx 5000$). The data of Hegde *et al.* (1999) also showed a significant lengthening (by as much as a factor of two) of the visible flame-lengths of turbulent hydrocarbon jet-flames between normal- and low-gravity. Idicheria *et al.* (2004) argue that the flame length data of Bahadori *et al.* (1993) and Hegde *et al.* (1999) are indicative of an extended laminar flow region in the low-gravity jet-flames. Whether this alone explains the difference between the flame length behavior (between normal- and low-gravity) in the Bahadori *et al.* (1993) and Hegde *et al.* (1999) studies and the present one is unclear.

RMS Characteristics

RMS fluctuations of flame luminosity were computed for each run. Although the same limitations outlined above (regarding the use of flame luminosity as a flame-zone marker) still hold, the RMS fluctuation fields provide a useful qualitative means of comparing the behaviors of luminous flames. As shown schematically in Figure 3.12, the RMS luminosity field may be used qualitatively to compare the large-scale intermittency at a given location. Such a comparison is justified on the grounds that the largest RMS fluctuations in a given series are related to regions of the image space whose intensity oscillates frequently between brightly illuminated and completely dark. Such large-scale fluctuations in image luminosity are generally caused by the flame being present or completely absent at a given location.

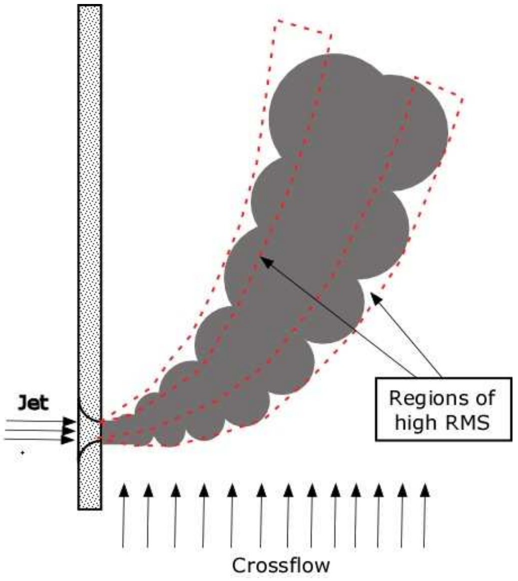

(a)

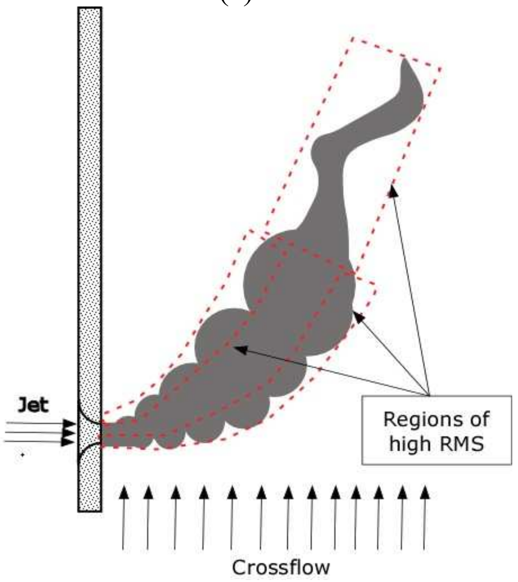

(b)

Figure 3.12 Schematic diagram illustrating differences in the flame structure that may account for the observed differences in the RMS luminosity fields between normal- and low-gravity. Frame (a) shows a JFICF wherein large-scale fluctuations are centered at the edges of the jet. Frame (b) shows a JFICF wherein the flame has thinned down and distort as it nears the tip, causing the RMS luminosity to peak near the centerline of the jet. As was shown earlier this characteristic is generally associated with the normal-gravity flames.

Figure 3.13 shows sample images of the RMS luminosity fields for each of the cases studied as a percentage of the maximum average luminosity for that run. Several characteristics are noticeable in the RMS fields. In the low momentum cases, both the normal and low-gravity fields show a strong dual-peak profile. The peaks lay on the windward and leeward side of the jet, with the windward side peak being the stronger of the two. This confirms the observation (based on instantaneous luminosity images) of greater penetration of unburned air on the windward side of the jet.

The dual-peak RMS profile is much more apparent in the low momentum ratio cases, and lower jet-exit Reynolds number) cases. As the momentum flux ratio increases (along with jet-exit Reynolds number), the dual peak RMS field profile becomes less and less obvious. Since the RMS luminosity field is strongly influenced by the large-scale intermittency of luminous jet-fluid and non-luminous crossflow fluid, it would appear that large-scale luminous structures play a more dominant role in the lower-momentum cases. Such a characteristic is to be expected given the relatively low Reynolds number (≈ 3350) of the low momentum cases. The heat-release associated with the presence of a flame is also known to stabilize, and even induce a local re-laminarization, of turbulent jet flames (Takagi *et al*. 1980, Takagi *et al*. 1981, Clemens *et al*. 1995) and JFICF (Savas *et al*., 1997). As such, the lower-momentum flames may be considered transitional and thus more sensitive to Reynolds number. With increasing Reynolds number, large-scale intermittency can be expected to be a less dominant feature of the luminous flame. This indeed appears to be the case.

In the low-momentum, normal-gravity cases (Figure 3.13a and Figure 3.13b, left) the dominant (windward-side) RMS-peak moves toward the center of the jet with downstream distance and the two peaks coalesce. This coalescence of peak RMS luminosity is not apparent in the low-gravity cases. It is also not as apparent in the highest momentum ratio case, where the RMS fields look very similar. The coalescence of peak RMS luminosity toward the leeward side of the jet in the lower-momentum, normal-gravity cases is suggestive of an asymmetry in the large-scale structure of the JFICF. The fact that this asymmetric RMS-peak coalescence behavior is not observed in the low-gravity cases suggests that the reason for it is buoyancy-related.

Based on the flame-luminosity image-sequences (Figure 3.3 - Figure 3.6) discussed in a previous section, the following argument can be made to explain the differences in the RMS luminosity fields between normal and low-gravity. It was noted that at the lower momentum-flux ratios, the normal-gravity flames assume a thinner, more distorted instantaneous flame-shape than their low-gravity counterparts. As can be seen in Figure 3.4, the thin luminous flame-shape does not typically correspond to the mean-luminous flame-width (as is the case in low-gravity) but tends to oscillate from one side to the other with the convection of large-scale flow structures up through the flame. The oscillation of the instantaneous luminous flame-shape results in frequent, large-magnitude fluctuations between light and dark in a given region of the image. Such large-magnitude fluctuations would result in large RMS luminosity. If the dominant source of luminosity fluctuations in the normal-gravity flames were oscillations of a thin luminous flame-shape from side-to-side across the mean-luminous flame-shape, rather than from the penetration of unburned fluid (from the crossflow) across the edges of a thicker instantaneous flame-shape (as appears to be the case in low-gravity) one would expect a single-peak RMS luminosity profile. The fact that the higher momentum-flux cases show more dual-peaked profiles, as well as thicker and less oscillatory instantaneous luminous flame-shapes would appear to support this conjecture.

The large peaks of the RMS luminosity fields are seen to persist further downstream in normal-gravity than in low-gravity. This is most evident in the lower-momentum cases and less-so in the highest-momentum case. As noted above, the persistence of peak-RMS luminosity is indicative of greater large-scale fluctuations in flame-luminosity in the downstream region. As such, based on the argument above as well as on the previously noted similarities between the instantaneous images shown in Figure 3.5 and 3.6 (low- and normal-gravity, r = 11.5, Re = 5500 cases, respectively), it appears that the high-momentum flux ratio case is momentum-dominated or close to it.

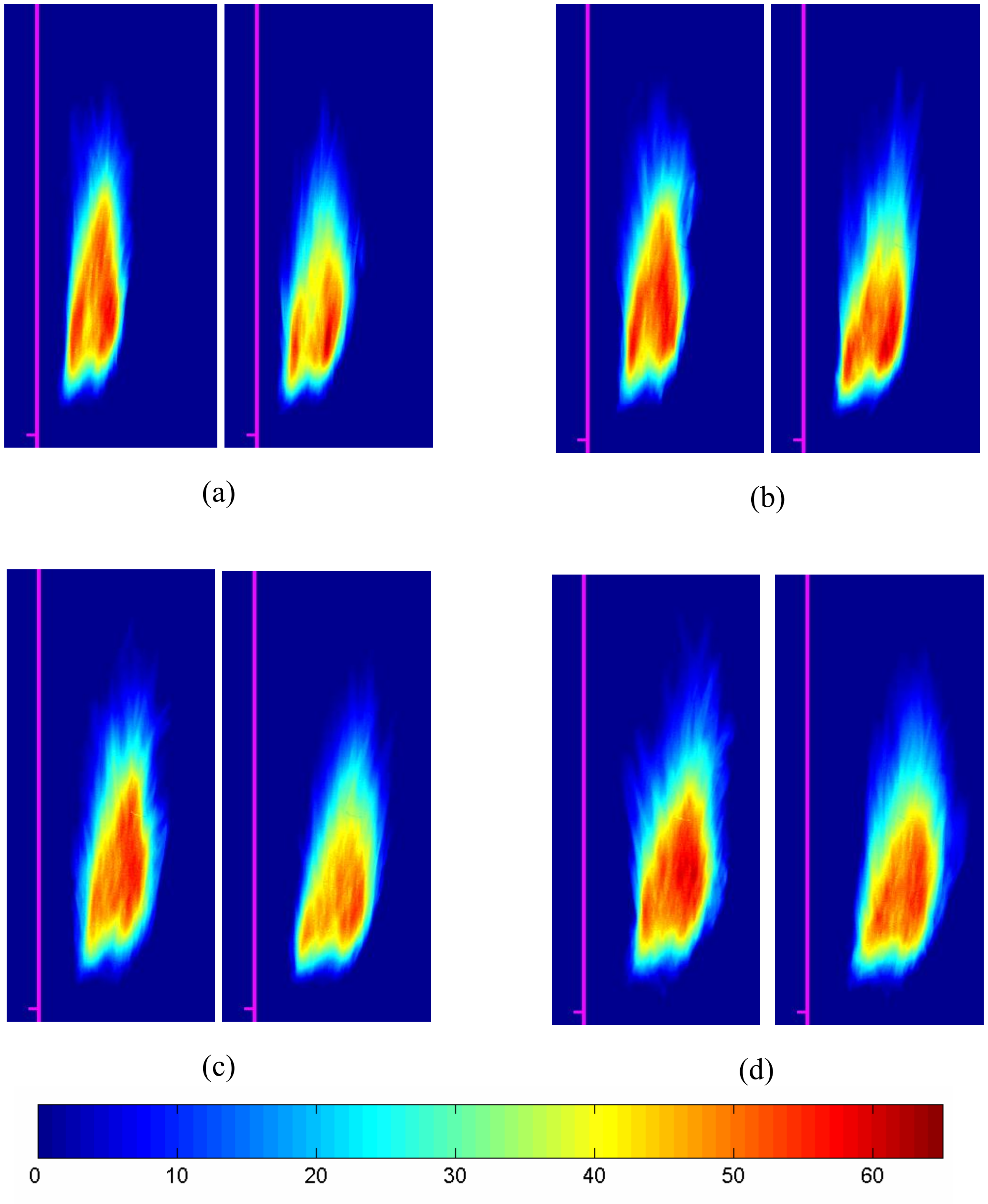

(a)

(b)

(c)

(d)

Figure 3.13 Sample RMS luminosity fields, normalized with max intensity. (Left-hand-side images correspond to normal-gravity and right-hand-side ones to low-gravity). a) r = 7, Re = 3350 b) r = 8.5, Re = 4070 c) r = 10, Re = 4800 d) r = 11.5, Re = 5500

Trajectories

The ensemble-average flame-luminosity images were used to determine the centerline trajectories of the JFICF. This was done as shown in Figure 3.13, wherein each mean luminosity image was converted to a binary image based on an intensity threshold corresponding to 10% of the maximum value of the mean image. The binary image was then scanned row-by-row to determine the center-point of each line of the flame. The row and column indices of this centerline trajectory data were then converted to units of '*rd*' using a calibration ruler image (which was taken prior to each run). These data were then fitted to the classic *x/rd* vs. *y/rd* power law using an unconstrained nonlinear (Nelder-Mead, a.k.a. the "downhill simplex") minimization function (MATLAB).

As mentioned previously, the dynamic range of the camera was insufficient to capture the dim, bluish near field of the flame. As such, only the far-field trajectories were obtained in this study and the power laws determined based on them should not be considered valid in the near-field region. Also, as can be seen in the mean flame-shape images of Figure 3.9, the base of flames tend to have a local inflexion point and lee-ward bias. The power-law fit was begun several rows above this feature in all the images to avoid including a physically unrealistic discontinuity in the trajectory.

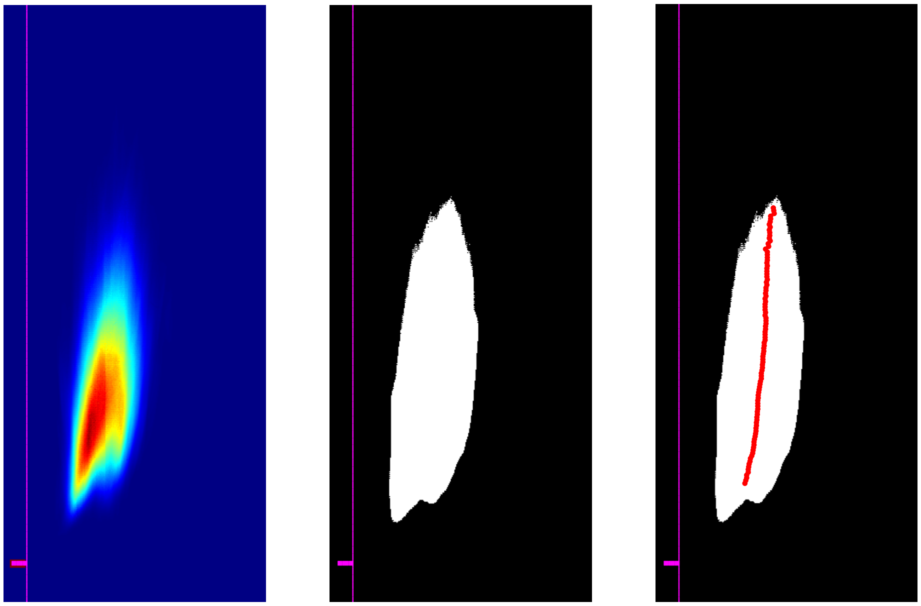

Figure 3.14 Trajectories were based on the centerline of the visible flame, as determined by a threshold corresponding to 10% of maximum intensity in the ensemble average image.

Figure 3.15 shows plots of the centerline trajectories for each of the four cases studied. The trajectories in this figure are normalized in terms of '*rd*' and plotted in linear format with a one-to-one aspect ratio. This format highlights the subtlety of the differences in centerline trajectories between normal- and low-gravity. It is clear from this figure that in all cases, the low-gravity JFICF penetrates further into the crossflow than its normal-gravity counterpart. It is also apparent in the lower-momentum flux cases that the trajectories tend to diverge significantly as they move downstream. The magnitude of the difference in normal- and low-gravity trajectories appears to decrease with increasing momentum flux ratio.

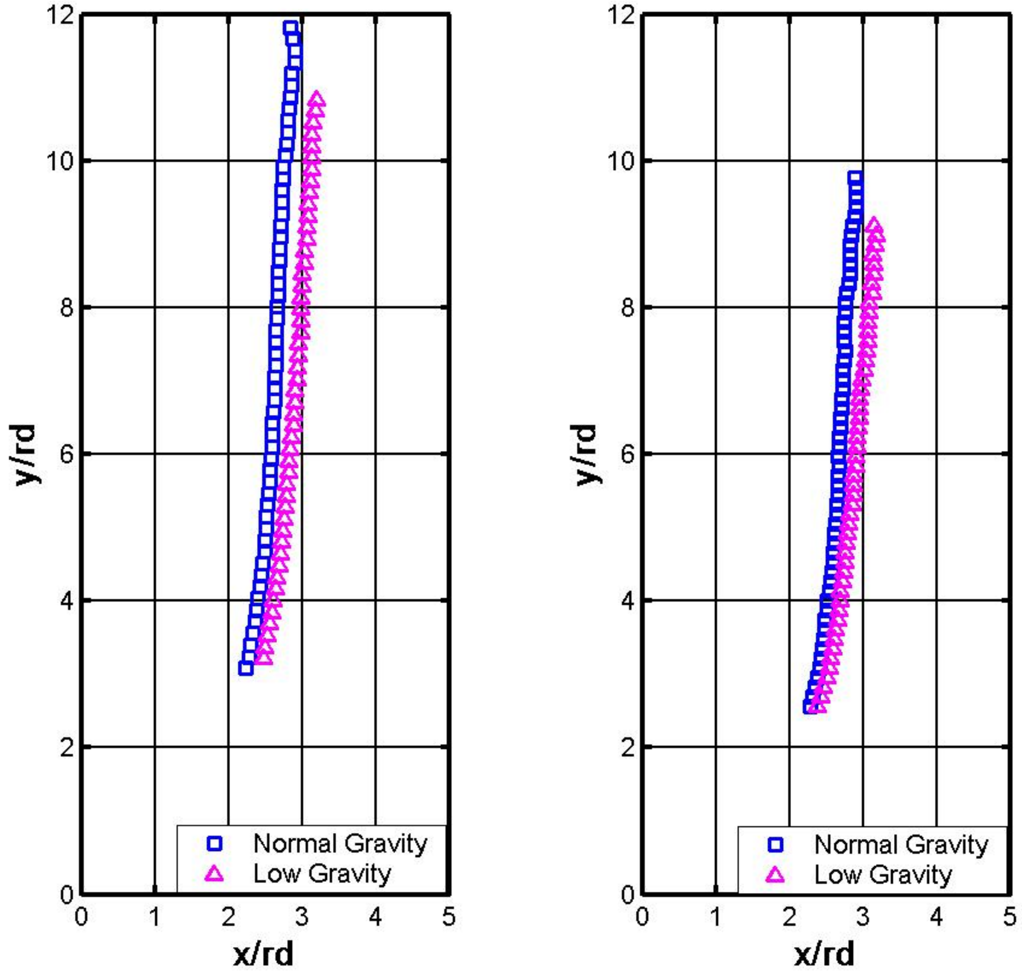

(a) (b)

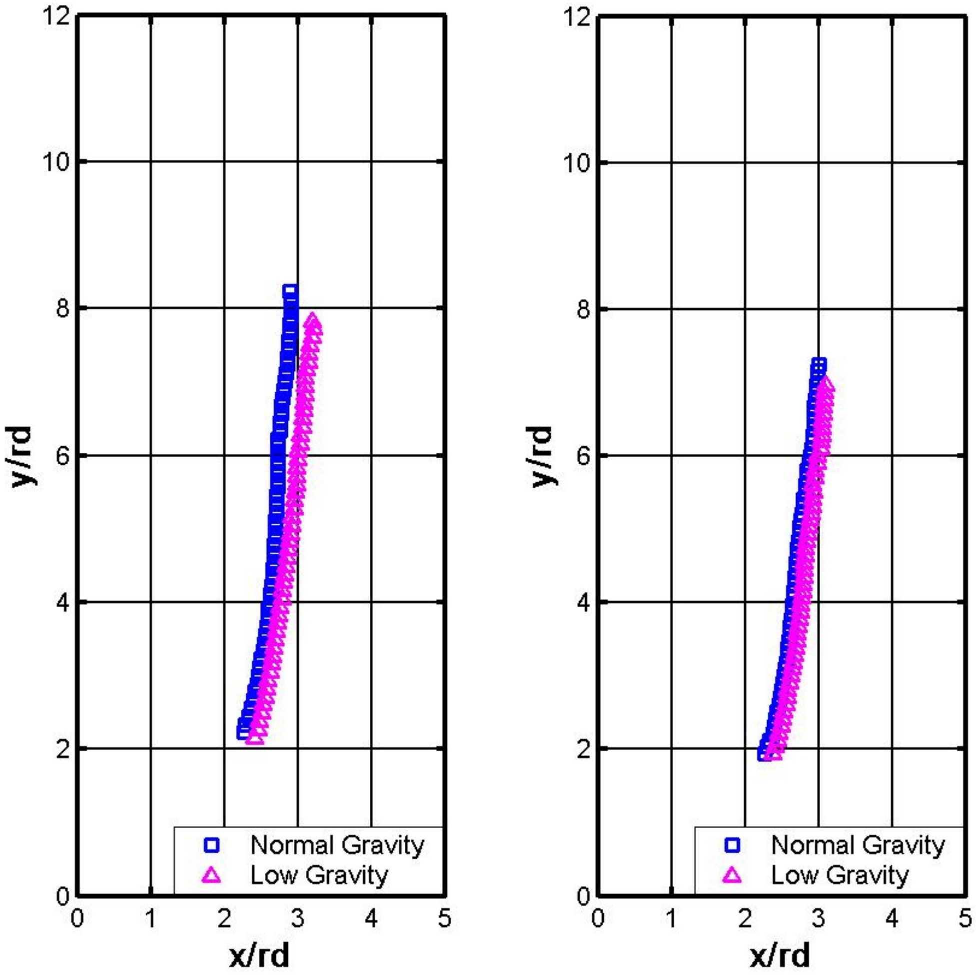

(c) (d)

Figure 3.15 Centerline trajectories for each case. Plotted here with a one-to-one aspect ratio, i.e. *x*- and *y*-axis have the same scale. (Squares = Normal-gravity, Triangles = Low-gravity). a) r = 7*, Re* = 3350. b) r = 8.5, *Re* = 4070 c) r = 10*, Re* = 4800 d) r = 11.5*, Re* = 5500

Figure 3.15 shows the measured centerline trajectories for each case plotted on logarithmic axes. The trajectories were fit to the classic $(x/rd) = A(y/rd)^n$ power-law. As can be seen in the plots, the trajectories of the low-gravity flames appear to follow a single power-law scaling throughout the region of interest. For reasons to be described later in this section, the normal-gravity trajectories were fit to the *rd* power-law in two different regions. The beginning and end of these two regions are shown in the plots as vertical, magenta colored lines. These best-fit power-law scalings are shown overlaid on Figure 3.16 in order to show how closely the measured trajectory mimics the derived power-law scaling.

It is immediately clear from Figure 3.16 that the centerline trajectories of the low-gravity flames follow the classic $(x/rd) = A(y/rd)^n$ power-law scaling much more closely than the normal-gravity flames. Whereas the low-gravity flames tend to follow the power-law scaling with little apparent deviation in all four cases, the normal-gravity flames tend to assume an almost S-shaped profile when plotted on the logarithmic scale. Viewed on the logarithmic scale, the slope of the normal gravity centerline trajectory appears to initially mimic that of the low-gravity flame. However in all cases, beyond a certain downstream location the trajectory of the normal-gravity flames deviates from the power-law and turns more toward the vertical, taking on a steeper slope (i.e. smaller power-law exponent). After this transition the trajectory appears to once more follow a power-law scaling with *rd*, albeit one with different multiplicative and exponential coefficients.

The difference in centerline trajectory outlined above is consistent with a transition of the JFICF from a momentum-dominated, forced convection limit to a buoyancy-influenced regime. Conservation of momentum dictates that when a non-buoyant, non-reacting jet penetrates a crossflow, the rate at which it turns in the direction of the crossflow depends exclusively upon its entrainment of crossflow fluid. With buoyancy present in the normal-gravity JFICF this is no longer the case as y-direction momentum is no longer conserved. The trajectory of a buoyancy-influenced JFICF can depend on both the rate of entrainment of crossflow fluid and on the body force generated by the large density difference resulting from heat-release of the flame.

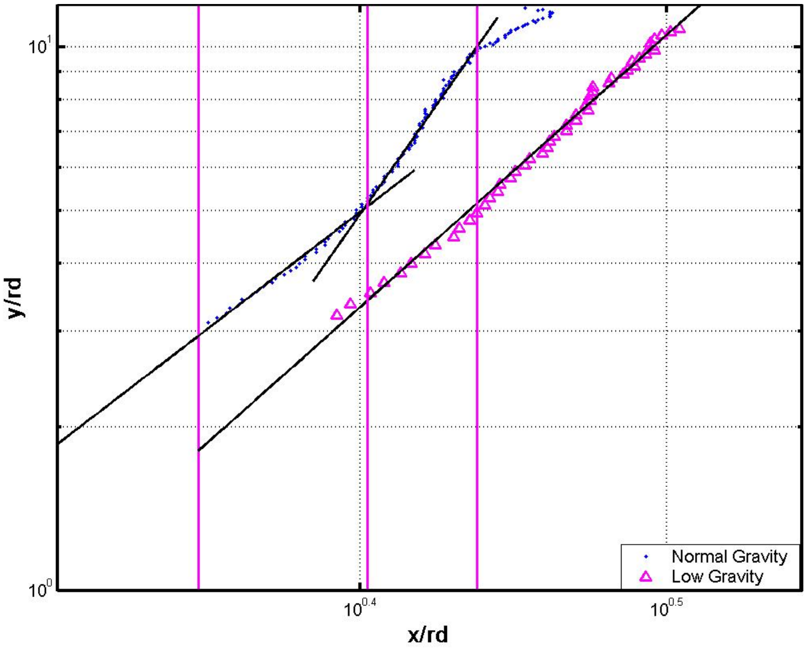
10^1
10^0
y/rd
10^0.4
10^0.5
x/rd
Normal Gravity
Low Gravity

(a)

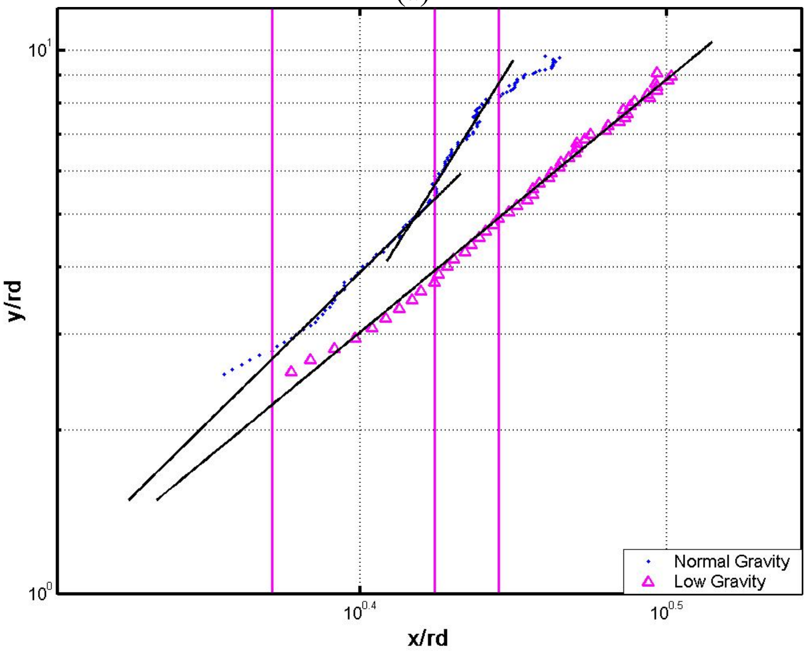
10^1
10^0
y/rd
10^0.4
10^0.5
x/rd
Normal Gravity
Low Gravity

(b)

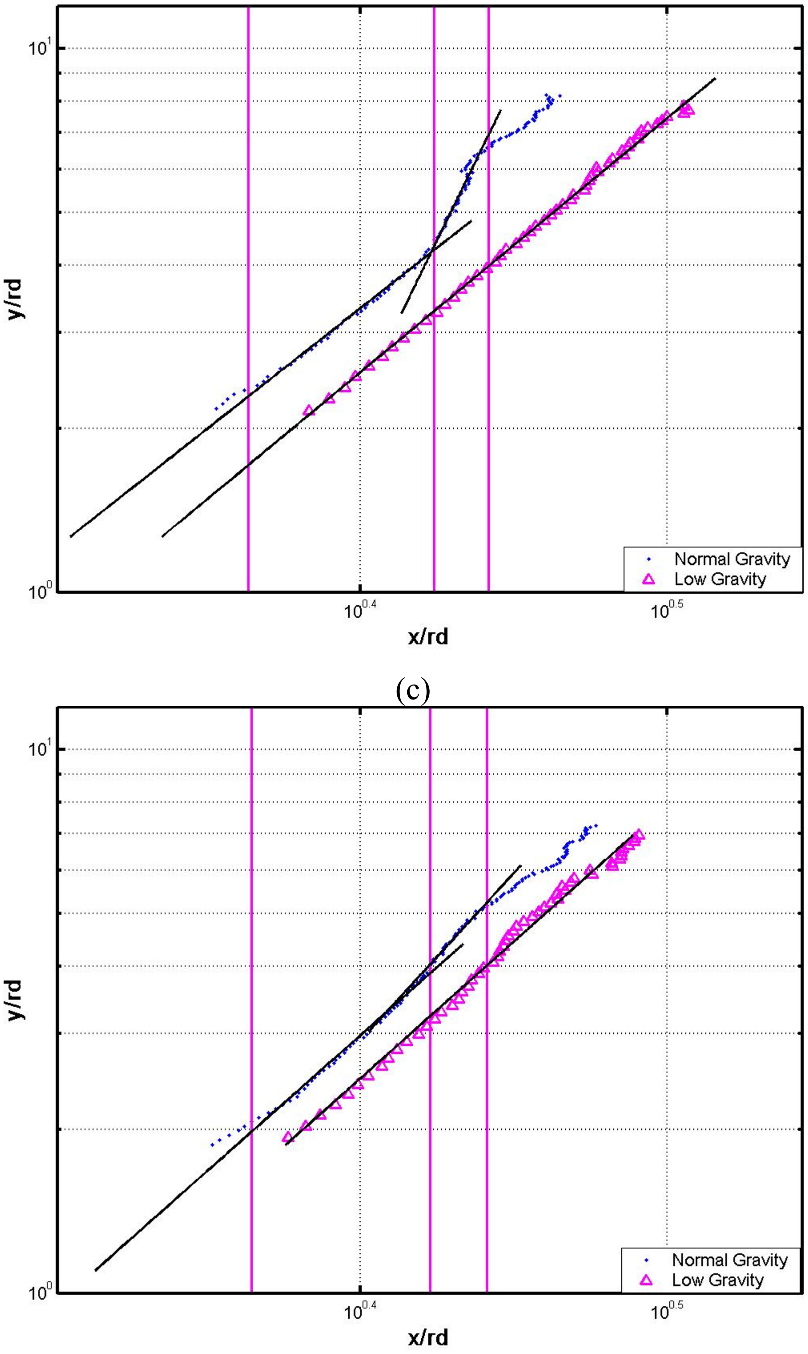

(c)

(d)

Figure 3.16 JFICF Centerline Trajectories – Based on mean luminosity a) $r = 7$, $Re = 3350$. b) $r = 8.5$, $Re = 4070$ c) $r = 10$, $Re = 4800$ d) $r = 11.5$, $Re = 5500$

As buoyancy in a turbulent JFICF scales with the volume of the jet, its relative influence is expected to grow with downstream distance. As such, the point where the centerline trajectory begins to turn more rapidly in the vertical direction should indicate the limit of the forced convection regime and the beginning of a buoyancy-influenced flowfield. In an effort to locate this point, the centerline trajectories of the normal-gravity JFICF were fit to two separate power-laws. These two best-fit power-law scalings and the cutoff-points used to determine them (marked by the vertical, magenta-colored lines) are shown in Figure 3.16. The cut-off point between the two power-law scalings in each case was taken to be point of transition between the forced-convection and buoyancy-influenced regions of the JFICF.

Table 3.5 lists the power-law relations for each best-fit trajectory scaling shown in Figure 3.16. The power-law relations for centerline trajectory in low-gravity show qualitative agreement with those found in the lower power-law scaling region of the normal-gravity JFICF. Whereas the multiplicative and exponential coefficients for the low-gravity JFICF range from 1.98 to 2.09 and 0.2 to 0.21 respectively, the coefficients for the lower-region of the normal-gravity flames range from 1.73 to 2.02 and 0.18 to 0.23 respectively. The similarity in trajectory scalings supports the conclusion that the normal-gravity flames are momentum-dominated in this region.

The multiplicative and exponential coefficients of the upper centerline trajectory power-law trajectory scaling are considerably different from those of the low-gravity scaling, ranging from 2.06 to 2.34 and 0.09 to 0.16 respectively. Although the magnitude of the multiplicative constant varies by approximately 10%, the exponential coefficient is reduced by up to approximately 50%, indicating a significantly more vertical trajectory. This increase in the verticality of the centerline trajectory is consistent with an increased buoyant force on the jet.

r	**A**	**n**
7	1.98	0.2
8.5	1.98	0.21
10	2.06	0.21
11.5	2.09	0.2

(a)

r	**A**	**n**
7	1.73	0.23
8.5	1.96	0.18
10	1.91	0.23
11.5	2.02	0.2

(b)

r	**A**	**n**
7	2.06	0.12
8.5	2.19	0.11
10	2.34	0.09
11.5	2.11	0.16

(c)

Table 3.5 – Best-fit power-law scalings for jet-centerline trajectory. (a) Low-Gravity JFICF (b) Forced-convection limit region of normal-gravity JFICF (c) Buoyancy-influenced region of normal-gravity JFICF.

It should be noted here that the magnitude of the power-law exponent for the JFICF trajectory scalings (particularly in the buoyancy-influenced regime) is significantly smaller than values measured in previous studies. For example Brzustowski (1977) studied turbulent JFICF and defined a jet-centerline trajectory based on color photographs of flame-luminosity and concluded that the power-law scaling of Pratte and Baines (1967), $(x/rd) = 2.05(y/rd)^{0.28}$ provided a reasonable match. However, in the same study Brzustowski plotted several other power-law scaling lines alongside the measured data with power-law exponents in the range of 0.24 to 0.25, which appear (to this author) to better match his data in the far-field.

Hasselbrink and Mungal (2001b) used PIV to study lifted methane JFICF of similar jet-exit conditions and measured a best-fit centerline trajectory scaling of $(x/rd) = 2.1(y/rd)^{0.33}$. The applicability of this trajectory scaling to the present study is questionable though as it is well known that centerline trajectories based on velocity penetrate further than those based on max temperature (Kamotani and Greber, 1972). The Hasselbrink scaling was also based on a lifted JFICF, which one would expect to have had significantly different near-field entrainment characteristics that could conceivably lead to a different far-field trajectory.

The reason for the difference in magnitude of the power-law exponent is not known but as mentioned in Chapter 1, the choice of definition of jet-centerline trajectory and the range of *rd* over which one attempts to apply a given power scaling will affect the value of the multiplicative and exponential coefficients in the *rd* power-law trajectory scaling. As noted above, the centerline trajectory based on maximum velocity scales differently than the one based on maximum concentration or temperature. The fore-aft asymmetry in mean flame luminosity may result in a different mean centerline trajectory than one determined by the threshholding technique used in this study. The

Brzustowski (1977) study plots power-law scalings for centerline trajectory ranging $x/rd > 1$ to $x/rd > 10$, without distinction between near-field and far-field trajectory scaling. Hasselbrink and Mungal (2001b) attempt to capture the near-field, far field, reacting and non-reacting cases in a single, universal power law scaling. In doing so however, they blur potentially significant trends in the trajectory data. For example, it is well-established (Kadota *et al.*, 1990, Huang and Chang, 1994, Hasselbrink 1999) that JFICF tend to penetrate further into the flow than JICF due to the decreased entrainment of the flame. The studies of Pratte and Baines (1967) and Smith and Mungal (1998) found that the power-law exponent for the case of nonreacting, isothermal JICF was 0.28. Indeed, Hasselbrink and Mungal (2001b) note up to 15% difference in the x-location of the centerline trajectory (at a given y-location) of a JFICF as compared that of a JICF. Given the multitude of factors governing the power-law scaling for jet-centerline trajectory, some variation in the magnitude of the power-law exponent is to be expected.

One possible explanation for the difference in the trajectory between the current study and that of previous work is the effect of confinement. Whereas the Hasselbrink and Mungal (2001b) study used a relatively large (500 *mm* × 500 *mm*, or 106 × 106 exit-diameters) test section, the present study used a smaller facility, measuring 203 × 203 *mm* or 64 × 64 exit-diameters. The test-section in the Hasselbrink and Mungal (2001b) study was 2.7 times larger (scaled in terms of jet-exit diameter) than the present study. In order to check this possibility, the maximum luminous flame width was measured for the widest case ($r = 11.5$, low-gravity) and found to be approximately 71 *mm* across. Assuming the jet has a circular cross-section with same diameter, the cross-sectional area of the jet would be 3970 mm^2, or approximately 9.6% of the test-section area. As a check for possible blockage effects caused by the presence of the jet in the test section, Mie scattering images (to be described in detail in Chapter 4) were used to check crossflow velocity at the level of the injector and at downstream locations comparable to the aforementioned point of transition in normal-gravity centerline trajectories. This was done by manually tracking alumina particles in the crossflow region from one frame to the next and computing their velocity. It was found that the crossflow does accelerate slightly with downstream distance but this acceleration is relatively minor, corresponding to approximately 6.4% of the crossflow velocity (1.42 ± 0.04 *m/s* at jet-exit level vs. 1.51 ± 0.03 *m/s* downstream).

The effect of confinement does not seem to provide an adequate explanation for the difference in the power-law coefficient. This is because confinement effects would affect the leeward side of the jet first, as the windward side of the jet has greater room to expand. Thus, the jet centerline trajectory would move further from the injector wall and make it “less vertical”. Such a trajectory would have a higher power-law coefficient, rather than the smaller one noted above. As such, the effect of confinement does not seem a reasonable explanation for the difference in power-law exponent.

Table 3.6 lists the values of ξ_L for the point in each normal-gravity flame where the trajectory is believed to transition from the forced-convection regime into a buoyancy-influenced one. These values were determined by taking the (x,y) location of the point in the normal-gravity trajectory where the slope (i.e. power-law exponent) changes toward the vertical and finding the flame chord length there. The point is shown in Figure 3.16 as the middle of the three vertical, magenta colored lines. The values of ξ_L listed in Table 3.6 are based on the jet-fluid properties at room temperature and pressure. In all four cases, the transition point lies at approximately $\xi_L = 3$. The fact that the centerline trajectory scaling changes in all four cases at approximately the same value of ξ_L, combined with the absence of such changes in the trajectories of the low-gravity

JFICF (which all have $\xi_L < 3$) appears to support the conclusion that the phenomenon is in fact a transition from the forced convection regime to a buoyancy-influenced one.

r	ξ_L
7	2.98
8.5	3.26
10	2.92
11.5	2.87

Table 3.6 – ξ_L for point in each normal-gravity JFICF case where jet-centerline trajectory is believed to transition from the forced convection limit to a buoyancy-influenced flow regime. These values are based on the flame chord length (i.e. straight-line distance from the jet-exit to point on centerline trajectory) at the observed transition point.

This conclusion is consistent with the work of Becker *et al.* (1981), who studied a series of turbulent ethane jet flames issuing horizontally into still air. Based on 1 *s* time-exposure photographs, they concluded that the flames showed negligible buoyancy effects for $\xi_L < 3$. Studies have also concluded that in the case of a straight turbulent jet-flame, the large-scale flow structure is momentum-dominated for $\xi_L < 2 - 3$ (Becker and Yamazaki, 1978, Idicheria *et al.*, 2004). Although one would not expect a turbulent JFICF to scale in exactly the same way as a straight jet, the work of Becker and Yamazaki (1978) and Idicheria *et al.*, (2004) suggests that the $\xi_L = 3$ transition point in centerline trajectory scaling seen above is at least physically reasonable. It is also interesting to note that Hasselbrink and Mungal (2001b) observed (what they concluded to be) a buoyancy effect in the velocity profile of their $r = 10$, $\xi_L = 2.7$, lifted turbulent JFICF. This also suggests that $\xi_L = 3$ is a physically reasonable value around which transition from the forced-convection limit would occur.

Finally, the centerline trajectories shown in Figure 3.16 reveal an interesting feature. After the centerline trajectory transitions to a more vertical trajectory (which is thought to be indicative of the increased relative influence of buoyancy) it follows a power-law scaling in *rd* for some distance downstream. At some point downstream though, the power-law exponent (i.e. the slope of the measured trajectory, plotted in logarithmic scale) begins to change. The magnitude of the exponent appears to increase, which would correspond to the centerline trajectory slowing its turn toward the vertical. Careful consideration of the mean luminosity images suggests that this effect is related to an asymmetry in the mean luminous flame shape near the flame tip. This asymmetry appears consistent with the previously noted fore-aft asymmetry in the mean flame luminosity. The asymmetry of the mean luminous flame shape results in a skewed centerline (luminosity) trajectory at this region.

FLAMETIP CHARACTERISTICS

The time-resolved image-sequences of flame-luminosity were processed to determine the instantaneous flametip location. The flametip location is defined here as the maximum *y*-location in each image where the flame luminosity exceeds 15% of the maximum luminosity (1024 levels in the 10-bit dynamic range of the camera). Although the choice of this threshold is somewhat arbitrary, a manual inspection of the image sequences confirmed that it accurately captured the behavior of the visible flame-tip. Figure 3.17 shows a characteristic trace of the flame-tip, as determined by a range of intensity thresholds. The figure shows that while changing the intensity threshold alters the magnitude of the instantaneous flamelength, the characteristics of the large-scale flametip oscillations remain virtually unchanged.

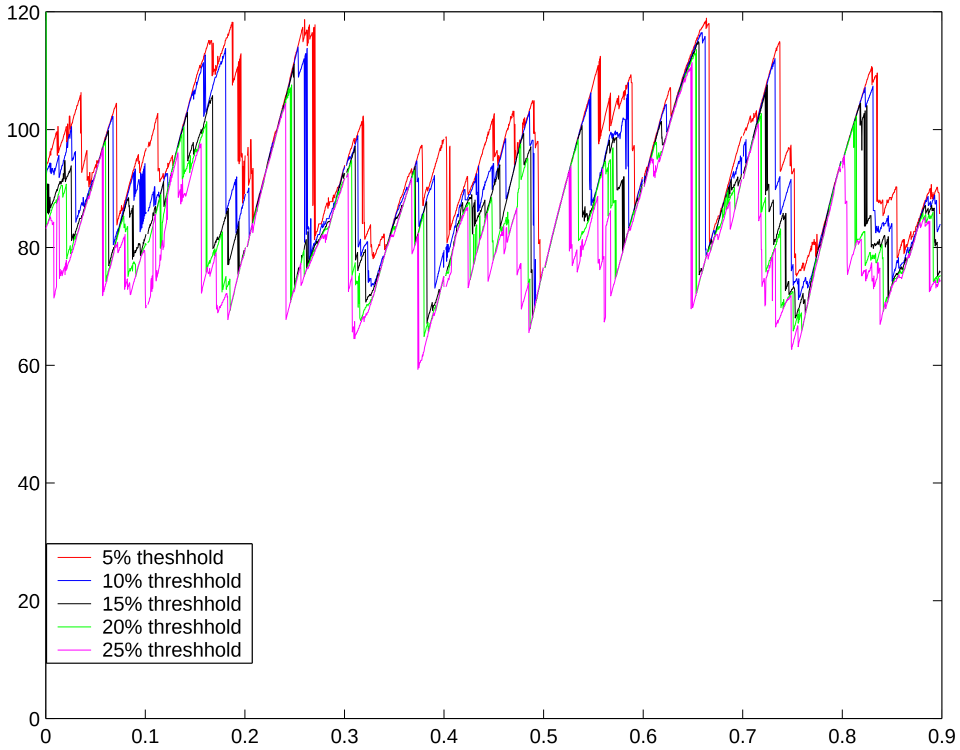

Figure 3.17 A representative flametip time-history trace as determined by a range of intensity thresholds. The large-scale flametip fluctuations appear insensitive to the intensity threshold used.

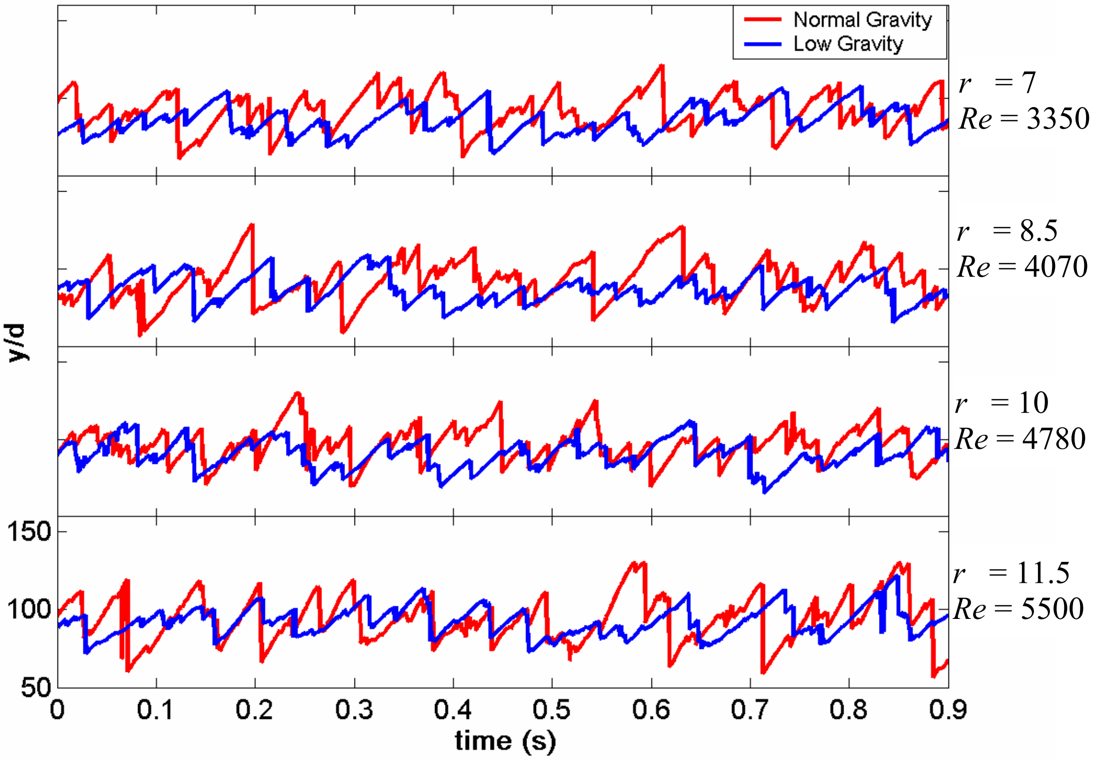

Figure 3.18 Instantaneous traces of flametip location for each case.

Figure 3.18 shows representative traces of the instantaneous flametip location for each of the JFICF cases studies. A close inspection of the traces reveals several interesting characteristics. For example, it is apparent from Figure 3.18 that both the normal- and low-gravity flametip traces tend to assume a "ramplike" profile wherein they rise steadily before abruptly falling to a lower value. Similar "ramplike" flametip time-history profiles were observed by Mungal *et al.*, (1991) in a study of straight turbulent jet-flames and by Dahm *et al.* (1985) in a study of momentum-dominated, liquid-phase reacting jets (otherwise known as acid-base "liquid flames"). Mungal *et al.* (1991) noted that this ramplike profile appeared closely linked to the evolution and burnout of large-scale coherent structures in the flow.

As noted in a previous section, Idicheria *et al.* (2004) compared normal- and low-gravity (i.e. high- and low-ξ_L) straight turbulent jet-flames using high frame-rate digital imaging. They observed that while the low-gravity (low-ξ_L) flames showed a ramplike flametip profile, the normal-gravity traces tended to assume a more "sawtoothed" profile wherein each rise and fall of the flametip trace was approximately symmetric. As noted previously, their flame-luminosity image sequences showed elongation and distortion of the flame near the flametip similar to that seen in the present study. Based on their luminosity imaging, they concluded that the buoyancy-induced distortion of the flame resulted in less uniformly mixed structures near the flametip and thus the more gradual burnout noted in the sawtooth flametip time-history profiles. Their observations contrasted with those of Mungal *et al.* (1991), who studied flames of virtually the same ξ_L (10.2 vs. 10.1) and saw only ramplike flametip profiles. Idicheria *et al.* (2004) suggested that a possible reason for the difference was the higher Reynolds numbers of the flames studied by Mungal *et al.* (1991).

The ξ_L values of the JFICF in the present study ($\approx 4.6 - 6.2$ at 1-*g*) are significantly smaller than those of Idicheria *et al.* (2004), ($\approx 7.9 - 12$ for their propane flames at 1-g). Thus, at similar Reynolds numbers (3350 – 5500 for the present study vs. 2500 – 8500 for the propane flames of Idicheria *et al.*, 2004), the effect of buoyancy would be reduced by a factor of approximately 7.25. Although the JFICF and straight jet-flames have fundamentally different flowfields, it seems reasonable to suggest that this reduced buoyancy may partially explain the observed difference in flame tip burnout characteristics.

As mentioned previously, Idicheria *et al.* (2004) argued that the "sawtooth"-shaped flametip time-history profile was caused by buoyancy-induced distortion of coherent structures convecting up through the flame. They argued that this distortion of the coherent structures results in less uniformly mixed regions in the flame and thus a more gradual flametip burnout. This interpretation may help explain the more ramplike flametip time-history profiles seen in the present study. It was noted previously (based on the luminosity image sequences) that the shear-layer vortices appear to have a dominant influence on flametip burnout characteristics. Given the reduced effect of buoyancy (i.e. reduced ξ_L values) noted above, it appears the buoyancy felt by the JFICF was insufficient to cause the same level of distortion as that noted by Idicheria *et al.* (2004). Although the luminosity image sequences do reveal significant elongation and distortion of the flame similar to that noted by Idicheria *et al.* (2004), this effect does not appear to have as pronounced an impact on flametip dynamics.

As can be seen in Figure 3.18, each 0.9 *s* experiment captured approximately 18 - 26 large-scale flametip oscillations. This was insufficient to perform a reliable Fourier decomposition on the flametip traces. Given the range of parameters upon which flame luminosity depends (temperature, stoichiometry, etc), it is not clear such an analysis is either necessary or appropriate for this type of data. As noted above though, Mungal *et al.* (1991) argued that large-scale flametip fluctuations are closely linked to the convection of large-scale luminous structures up through the flame. With that in mind a manual (“by eye”) inspection was performed to locate the peaks of each large-scale flametip fluctuation in each data trace.

Table 3.7 lists the mean time between flametip peaks for each case. The uncertainties listed in this table correspond to 95% confidence levels (based on 53 – 72 large-scale flametip oscillations observed over three experiment runs for each case). This table shows that the timescales of the large-scale flametip oscillations are relatively insensitive to either buoyancy or momentum-flux ratio over the range of conditions studied. Such a result is not unexpected. It was previously noted that the dominant large-scale structures affecting flametip behavior appear to be the shear-layer vortices. These vortices form in the momentum-dominated near-field where one would not expect buoyancy to be significant.

r	τ (1-g, *s*)	Uncertainty (*s*)	τ (low-g, *s*)	Uncertainty (*s*)
7	0.047	0.007	0.046	0.006
8.5	0.043	0.005	0.047	0.006
10	0.040	0.005	0.047	0.005
11.5	0.037	0.005	0.041	0.005

Table 3.7 Flametip burnout timescale for each case, based on 15% luminosity threshhold. The uncertainties listed are 95% confidence levels based on 53 – 72 flametip oscillations gathered over 2.7 *s* total run time for each case. The 2.7 *s* of data was acquired in three separate experiment runs.

Table 3.8 lists the RMS of the flame length time histories (normalized by the mean flame length) for each case studied. While the timescales of the large-scale flametip oscillations do not appear to be buoyancy-dependent, the magnitude of these fluctuations does. In all cases the magnitude of the flametip oscillations are significantly larger in normal gravity than in low-gravity. The reason for this difference is not immediately clear.

r	Normal Gravity (%)	Low Gravity (%)
7	12.1	10.2
8.5	13.7	11.3
10	13.1	10.5
11.5	14.6	10.9

Table 3.8 – RMS of flametip oscillations (normalized by mean flametip location) for each case studied

Figure 3.19 shows the histograms of instantaneous flametip location for each of the four (normal- and low-gravity) cases studied. The histograms each comprise 8100 points, representing the first 2700 frames (or 0.9 *s*) of each experimental run. Although the computation of histograms removes time-dependent information from the flametip time-history data-sets, they provide a useful measure of the magnitude and distribution of flametip oscillations.

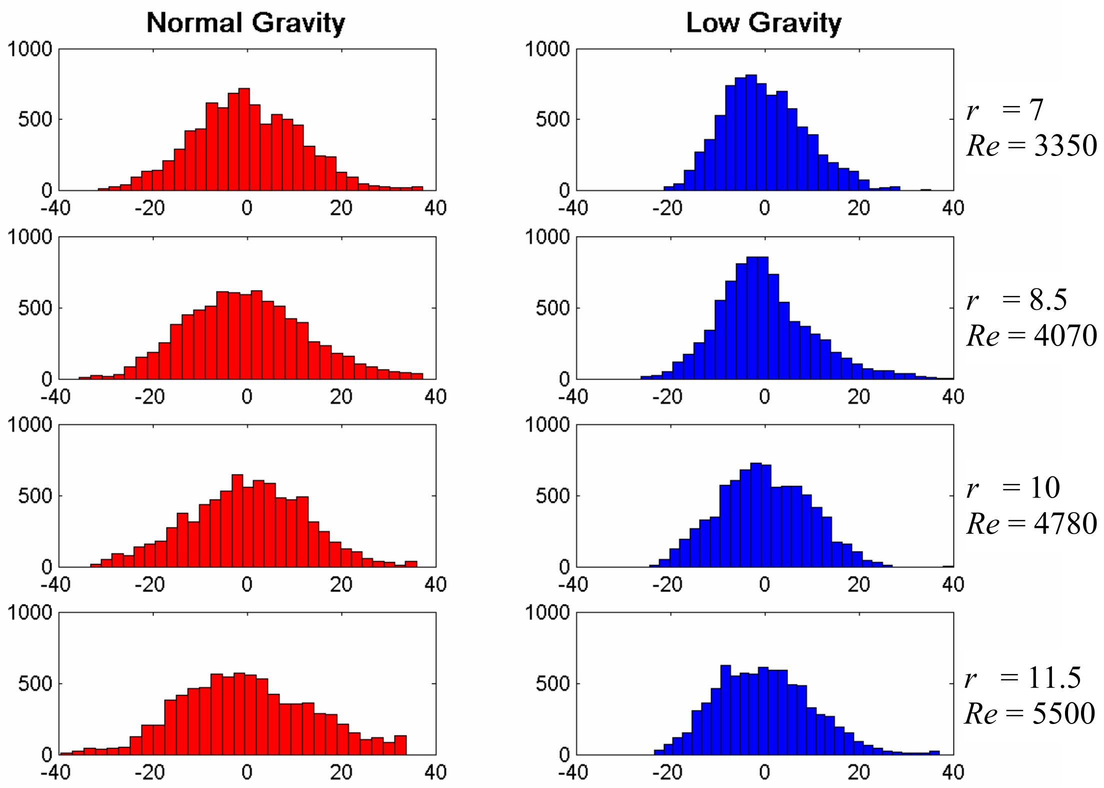

Figure 3.19 Histograms of flametip height for each case. The histograms of normal-gravity flametip location show a wider profile, which is indicative of larger-magnitude fluctuations of the instantaneous flame-tip locations about the mean.

In all cases, the histograms show single-peak profiles. Although the histograms appear to peak close to the mean flametip height, they do not display a clear symmetry about this point. In all four cases, the histogram of the normal gravity runs appears noticeably wider than its low-gravity counterpart. As a narrower histogram indicates more consistent, repetitive fluctuations occurring over a smaller range of magnitudes, the low-gravity flametip histogram is consistent with our previous observations of more coherent, organized flametip burnout behavior. The wider normal-gravity histogram is indicative of fluctuations taking place over a wider range of magnitudes, which would tend to indicate a more disorganized flametip burn out behavior.

The wider normal-gravity histograms are also consistent with the previous observation of larger standard-deviations of flametip-location about the mean in normal-gravity. Both are indicative of larger-magnitude flametip oscillations in normal-gravity than in low-gravity. The larger-magnitude flametip oscillations in normal-gravity are consistent with the previously observed differences in burnout characteristics. It was noted earlier that in low-gravity the JFICF flametips tend to dim and burn out uniformly across the width of the luminous flame. When luminous structures separate from the main body of the luminous flame in low-gravity they tend to convect downstream at roughly the same speed as they had prior to separation. In normal-gravity, when such a separation occurs, the luminous structures typically elongate and appear to accelerate away from the main body of the luminous flame. This produces a larger dim region between the instantaneous flametip and the main body of the luminous region than is the case in low-gravity. Thus, when the flametip burns out the magnitude of the fluctuation in flametip location is larger than it would be in low-gravity.

Chapter Four: PLMS RESULTS

Multi-kilohertz framerate planar laser Mie scattering (PLMS) was used to study a series of transitional/turbulent jet-flames in a crossflow (JFICF) under normal- and low-gravity conditions. PLMS imaging was used to acquire time-resolved cinematographic flow-visualizations of the large-scale flow structure of the JFICF. Mean PLMS data was used to determine the centerline trajectory (based on mixture-fraction), mixture fraction decay and the mean and rms jet-to-crossflow fluid intermittency along the JFICF in normal- and low-gravity.

EXPERIMENTAL CONSIDERATIONS

Three hydrogen-diluted propane JFICF were tested in normal- and low-gravity. The imaging fields of view are shown in Figure 4.1, and are 154 *mm* × 154 *mm*. The fields of view will hereafter be referred to as the "upper" and "lower" imaging locations. The imaging locations were set partially by the limited available volume inside the drop-rig, which limited the placement options for the camera. The usable area of the image was limited by the width of the laser sheet, which varied from approximately 70 *mm* on the right-hand-side of the image to 110 *mm* on the left. The sheet width was determined by the need to maintain sufficient intensity for good quality imaging. The sheet-illuminated area of the upper imaging location extends to approximately 190 *mm* downstream of the injector. This is slightly below the top of the field-of-view of the upper imaging location, which explains why the images appear discontinuous there. The camera head was positioned such that its field of view was offset from the wall by approximately 12 *mm* in order to avoid reflections from the laser where it impinges upon the wall of the flow-facility.

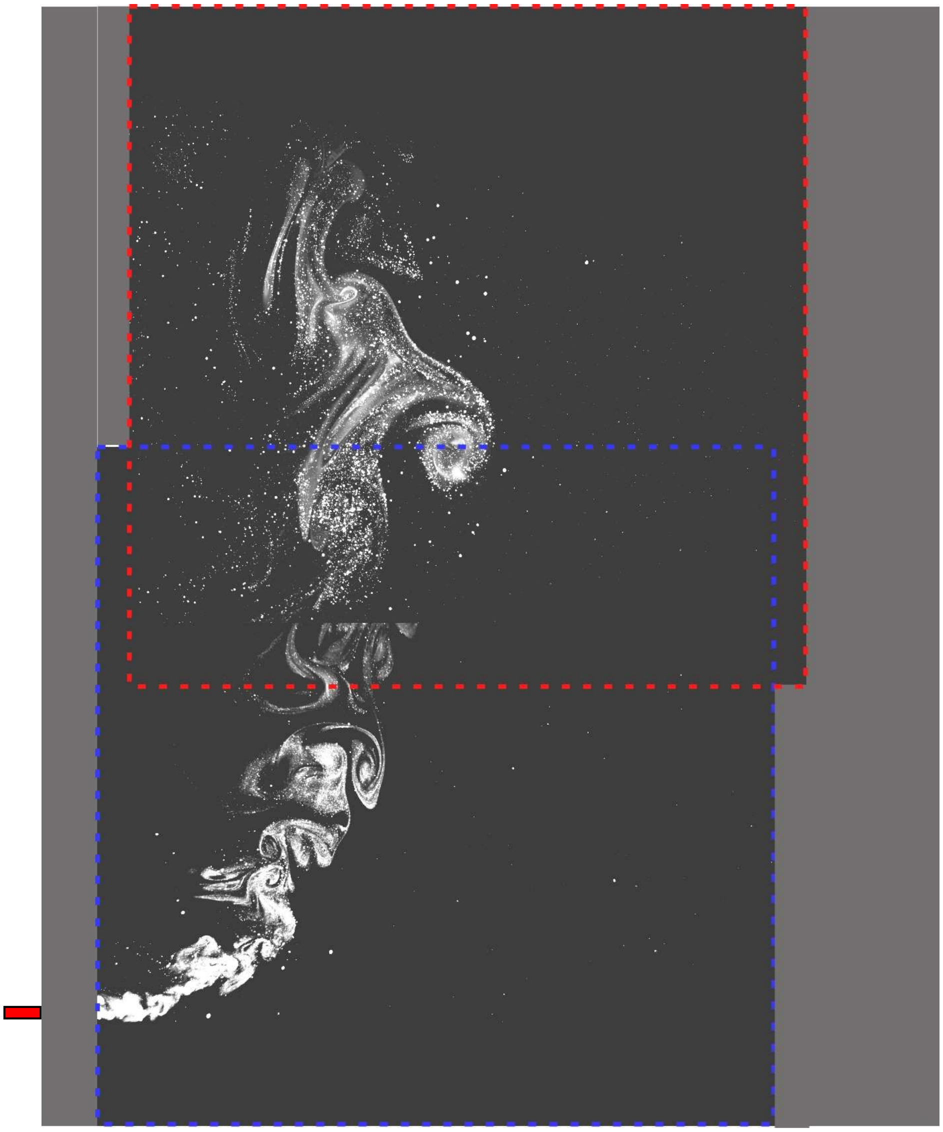

Figure 4.1 Fields of view for the upper and lower-PLMS imaging locations in relation to the width of the flow-facility test section. The field-of-view for the lower imaging location was offset from the test-section wall in order to minimize glare from laser reflections.

Table 4.1 lists the flow conditions used for each case. The momentum flux ratio *r*, *Re* and ξ_y are all based on jet-exit conditions at room temperature and pressure. Note, the ξ_y listed in the table is based on distance from the jet-exit to the upper edge of the sheet-illumination in the upper imaging location (approximately 60*d*), not flame-length. In several places in the upcoming sections, ξ_y values based on the distance from the jet-exit to the upper edge of the sheet-illumination for the lower imaging location will also be quoted. *St* refers to the Stokes number ($St = \tau_p/\tau_f$) of the alumina particles. This parameter will be discussed further in a later section.

Table 4.1 Experimental Conditions for PLMS Experiment Runs.

Parameter	Case		
	1	2	3
r	7	10	11.5
Re	3350	4780	5500
$\mathbf{u}_j$ (m/s)	11.3	16.1	18.5
$\mathbf{u}_{cf}$ (m/s)	1.3	1.3	1.3
$\xi_y\|_{y/d=60} - 1g$	4.31	3.40	3.10
$\xi_y\|_{y/d=60} - 0.01g$	0.93	0.73	0.67
St ($\times 10^4$) (at **y/d** = 20)	1.81	1.72	1.75

In all cases, the JFICF were seeded with alumina (Al_2O_3) particles. The particles have a nominal diameter of 0.3 μm, but in reality tend to be somewhat larger due to particle agglomeration (Rehm, 1999). The melting point of alumina is 2373K, which substantially exceeds the adiabatic flame temperature of the hydrogen-diluted propane/air mixture. The alumina particles are also non-reactive in the flame and as such may be considered a conserved scalar and used as a marker of matter originating in the jet-fluid. In this study, this characteristic was exploited to make a quantitative and qualitative investigation of jet-to-crossflow fluid mixing through the use of PLMS.

FLOW VISUALIZATION

As mentioned in previous chapters, the mixing and entrainment processes of a turbulent JFICF are dominated by a series of interacting, large-scale vortex systems. Much insight into the nature of these systems has come from the use of instantaneous flow-visualization images. Fric and Roshko (1994), Kelso and Smits (1995), Kelso *et al*. (1996) and Lim *et al*. (2000) all relied extensively on instantaneous images of non-reacting JICF to identify and evaluate key features of the jet/crossflow interaction.

Although there is potentially much physical insight to be gained from systematic flow-visualization studies of turbulent JFICF, such studies appear quite scarce in the literature. To provide just a single illustration of this scarcity, recall that it is well-established that the heat-release associated with the presence of a flame in a turbulent jet tends to inhibit the growth of the near-exit shear-layer (Clemens and Paul, 1995) and suppresses turbulence intensities there (Takagi *et al*. 1980, Takagi *et al*. 1981). Given the prominence of the shear-layer vortices in the flow-structure of turbulent JFICF one would expect this phenomenon to be of critical importance and provide rich fodder for flow-visualization studies. It appears however that few if any such studies have dealt with this issue in turbulent JFICF.

Although several recent studies have produced some fine schlieren images of various JFICF, (Huang and Chang, 1994, Savas *et al*., 1997, Choudhuri and Gollahalli 2000) there does not appear to have been an extensive or systematic effort to realize the potential of flow-visualization techniques to develop physical insight into the flow structure of turbulent JFICF. Detailed, systematic PLMS flow-visualizations of turbulent JFICF appear to be virtually absent in the published literature. The following section attempts to fill some of this gap in the literature using the PLMS images acquired in this study as time-resolved flow-visualizations for to quote Brown and Roshko (1974), “there is often no substitute for direct flow visualization”.

PLMS flow-visualization was used in this study to examine both the instantaneous and temporally developing structural characteristics of the JFICF. The following section is thus broken down into two parts with the first directly comparing and contrasting individual PLMS flow-visualization images. It is well known however, that instantaneous flow-visualization images can be misleading as the distribution of a scalar marker in a flowfield is strongly influenced by its integrated time-history (Hama, 1962, Cimbala *et al.*, 1988) and care must be taken in the interpretation of such images. With this in mind, the second part of this section deals with temporally developing flow characteristics using image sequences or “movies” of the instantaneous PLMS visualizations. Time-resolved PLMS flow-visualization allows one to track individual medium-to-large scale flow structures as they convect downstream and observe their interaction with other features of the flow. In this way, some of the uncertainty associated with the aforementioned short-coming of scalar-marker based flow-visualization can be overcome.

Single Image Comparisons

Figure 4.2 through Figure 4.4 show representative PLMS flow-visualization images of the three turbulent JFICF in (a) low-gravity and (b) normal-gravity. The images were processed to brighten them and enhance their contrast. As the upper and lower-imaging location experiments were conducted separately, there is no spatial or temporal correlation between individual flow-structures seen in the lower and upper portions of the images. The images are overlaid according their relative locations in physical space, as can be seen from the slight rightward offset of the upper imaging location with respect to the lower.

Figure 4.2 shows representative PLMS flow-visualization images from (a) low- and (b) normal-gravity experiments on the $r = 7$, $Re = 3350$ case. Several characteristic flow-features are present in these images. Comparing the normal- and low-gravity images, one sees that the shear-layer vortices appear more round and uniform in shape in low-gravity compared to those in normal-gravity. For example, the normal-gravity JFICF shear-layer vortices indicated by the white arrows overlaid on Figure 4.2(b) (normal-gravity) appear quite distorted and elongated in the vertical direction. Indeed, without time-resolved imaging or a prior knowledge of the topology of a JFICF, it would not be obvious from this image alone that the structures indicated were shear-layer vortices at all.

Although Figure 4.2(b) represents just one image among many thousands acquired for this flow-condition, the far-field behavior (specifically, the elongation and distortion of shear-layer vortices in the downstream region of the jet) is characteristic of the normal-gravity behavior of the JFICF. Similar elongation and distortion of shear-layer vortices was seen repeatedly throughout the time-resolved image sequences for the normal-gravity, $r = 7$ case. Although elongation and distortion was occasionally observed in the low-gravity flames, in that case it was generally in the cross-stream direction rather than the vertical, suggesting a dilatation or multiple-vortex interaction effect rather than a buoyancy-related one. This phenomenon will be illustrated in a later section dealing with time-dependent flowfield characteristics.

Although flame luminosity cannot be interpreted in exactly the same way as the PLMS visualizations (*i.e.* as a proxy for fluid originating at the jet-exit) the elongation and distortion of shear-layer vortices observed in Figure 4.2(b) appears consistent with the observation of similar behavior in the luminosity images shown in Chapter 3. It appears the distortion of the large-scale luminous structures noted in the (flame-luminosity) image sequences of Chapter 3 was actually indicative of distortion of the underlying shear-layer vortex structures.

Comparing the normal- and low-gravity PLMS images shown Figure 4.3 ($r = 10$, $Re = 4800$ case) one still sees evidence of distortion and elongation of the shear-layer structures in the far-field of the normal-gravity JFICF. Several representative vortex structures are highlighted by the white arrows overlaid on each image. Whereas the shear-layer vortices in the low-gravity JFICF appear relatively smooth and almost circular in profile, the normal-gravity shear-layer structures appear almost oval in shape. As can be seen from the arrows overlaid on the image, these oval-shaped vortices tend to align more toward the vertical direction than the horizontal. The distortion seen in Figure 4.3(b) appears much less significant than that noted in Figure 4.2(b) however. The shear-layer structures are still clearly recognizable, though somewhat elongated in the vertical direction. Their size and shape are similar to that of the low-gravity vortices.

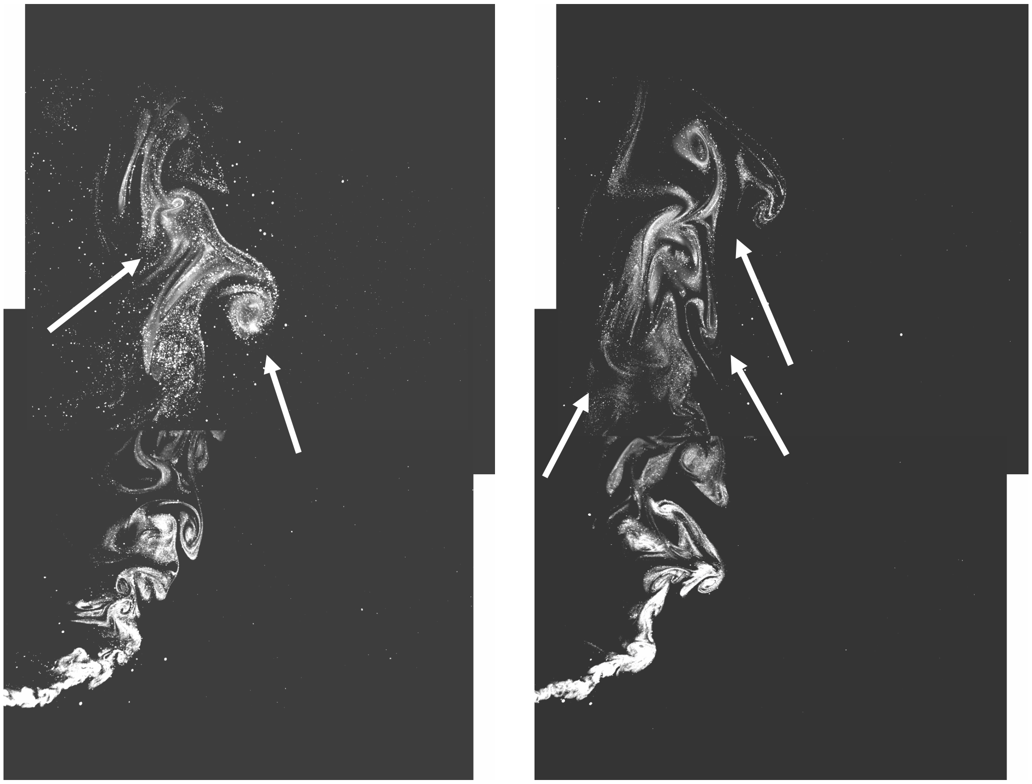

(a) (b)

Figure 4.2 Sample instantaneous PLMS flow-visualization images of the $r = 7$, $Re = 3350$ JFICF. The upper and lower images were each acquired in separate experiment runs and are not temporally or spatially correlated. The shear-layer vortex structures in the normal-gravity JFICF display noticeable elongation and distortion compared to their low-gravity counterparts. (a) Low-gravity (b) Normal-gravity

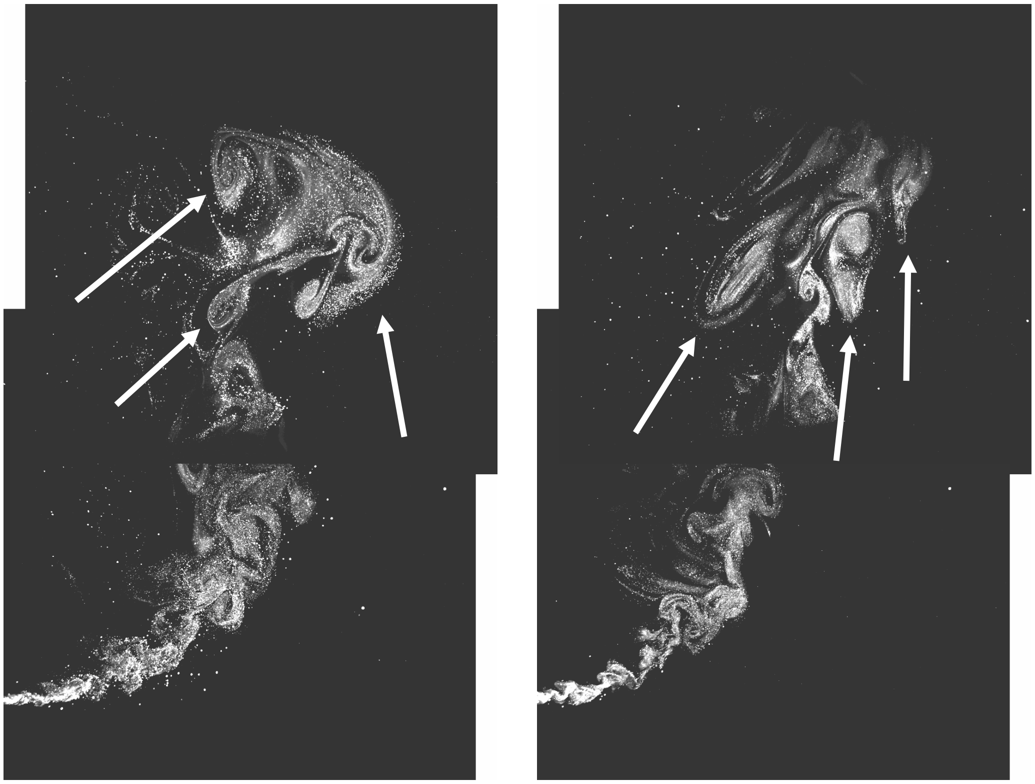
(a) (b)

Figure 4.3 Sample instantaneous PLMS flow-visualization images of the $r = 10$, $Re = 4800$ JFICF. The upper and lower images were each acquired in separate experiment runs and are not temporally or spatially correlated. As in the lower momentum-flux ratio case, the shear-layer vortex structures in the normal-gravity JFICF display more noticeable elongation and distortion compared to their low-gravity counterparts. In this case though, the difference appears less significant. (a) Low-gravity (b) Normal-gravity

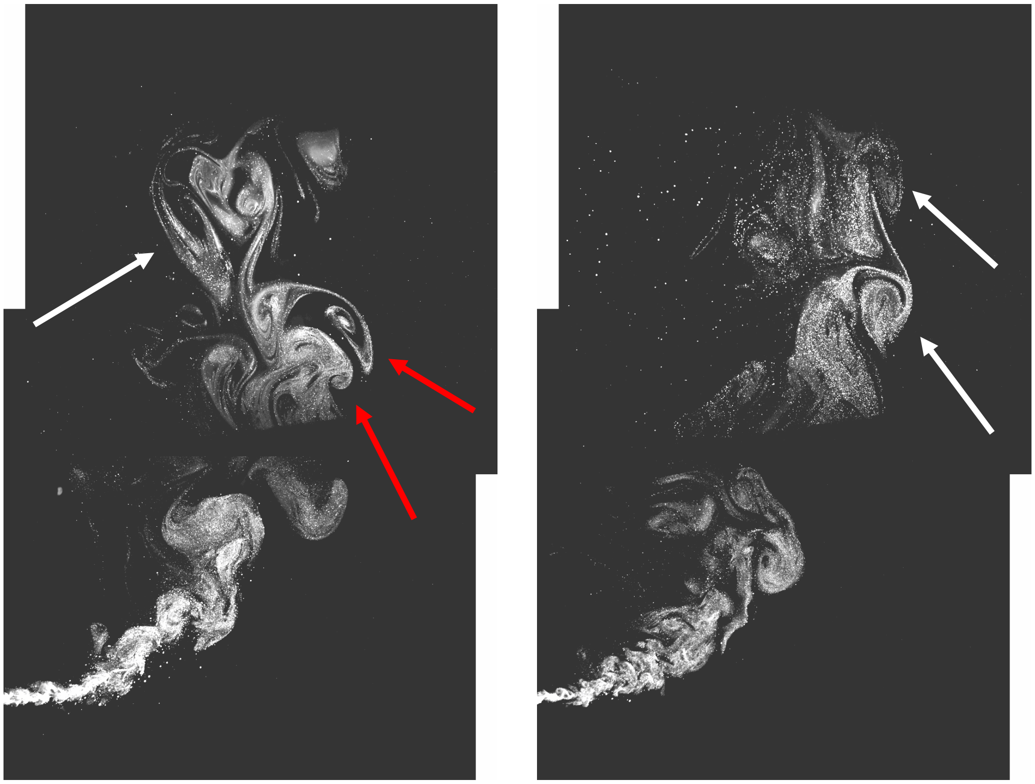

(a) (b)

Figure 4.4 Sample instantaneous PLMS flow-visualization images of the $r = 11.5$, $Re = 5500$ JFICF. The upper and lower images were each acquired in separate experiment runs and are not temporally or spatially correlated. In contrast the lower momentum-flux ratio cases, the normal-gravity JFICF does not show very significant elongation and distortion compared to its low-gravity counterparts. The apparent discontinuity between the upper and lower images reflects the cut-off caused by the laser-sheet, which expands in the vertical direction from the left to the right. (a) Low-gravity (b) Normal-Gravity

Figure 4.4 shows typical PLMS flow-visualization images taken from the normal- and low-gravity, $r = 11.5$, $Re = 5500$ case. Comparing the large-scale shear-layer vortices highlighted with arrows overlaid on Figure 4.4(a) and Figure 4.4(b), one does not see clear evidence of elongation and distortion noted in the earlier two figures. In both the normal and low-gravity cases the fuel-bearing (seeded) shear-layer vortex structures are clearly distinguishable in the upper imaging location. The vortices in this case appear relatively smooth and circular in shape.

Based on the observations above it seems logical to conclude that the elongation and distortion of the large-scale shear layer vortices is a buoyancy-induced phenomenon. Such a conclusion is consistent with the observations outlined in Chapter 3, which found similar elongation and distortion of the instantaneous luminous flame structure in normal-gravity at the lower momentum flux ratios. The mechanism by which buoyancy would generate such elongation and distortion is not immediately clear from the images above. One possibility is it exerts a global effect on the large-scale structure of the JFICF which alters the mean strain field, which would in turn alter the vortex dynamics. Without 2-dimentional velocity and strain field data however, it is impossible to determine whether this is the case.

It is noteworthy that the shear-layer vortex distortion is considerably more apparent in the $r = 7$ case than in the other two. Recalling the centerline trajectory data presented in Chapter 3, it was argued that at the downstream location corresponding to $\xi_C \approx 3$, the flow transitions from a forced convection limit to a buoyancy-influenced regime. Noting the value of ξ_y in the upper imaging location for the $r = 7$ case is 4.3 and 3.4 and 3.1 for the $r = 10$ and $r = 11.5$ cases respectively, the observations above are consistent with such a conclusion. It appears that above $\xi_C \approx 3$, buoyancy effects begin to become apparent in the instantaneous large scale structure of the flow. As noted in

Chapter 3, the transition from a forced convection limit to a buoyancy-influenced flow regime around such a value of ξ_C is consistent with previous studies.

Figure 4.4(a) appears at first to contradict the observations above in that it shows a distorted (i.e. flattened, non-circular) shear-layer structure (highlighted by the red arrows overlaid on the figure) in the high-momentum, low-gravity case. This is not the case however. As will be discussed in greater detail in the following section (related to the time-resolved PLMS image sequences), this structure is actually in the process of coalescing with another, smaller shear layer structure which is pushing up from immediately below it. Such vortex-coalescence induced distortion is common in all cases but generally occurs in the cross-stream (rather than vertical) direction. This image illustrates the value of time-resolved PLMS imaging. Based on this single flow-visualization image the cause of the distortion would not have been obvious and could possibly have lead to an erroneous dismissal of buoyancy as the cause of the observed distortion and elongation of large-scale shear-layer structures in the figures above.

Reynolds Number and Momentum-Flux Ratio Effects

In addition to comparing individual normal-gravity JFICF images with those from their low-gravity counterparts, it is instructive to compare them to the normal-gravity images from the other cases. The same goes for the low-gravity cases.

Comparing the low-gravity images of Figure 4.2(a), Figure 4.3(a) and Figure 4.4(a), one sees the effect of increasing Reynolds number and momentum-flux ratio. The effect of increasing momentum-flux ratio is particularly obvious in the increased penetration of the jet into the crossflow but also in the noticeably greater jet-width. The observed widening of the jet with increasing momentum flux ratio is consistent with the observations made in Chapter 3 based on flame-luminosity. It also agrees with the observations of several previous researchers (Kalghatgi, 1983, Rao and Brzustowski, 1982, Kadota *et al*., 1990). It appears from the PLMS images that not only does the overall jet-width increase but so too do the width of individual large-scale shear-layer vortices. As expected in the case of increasing jet-exit Reynolds number, the PLMS images appear to show an increased range of shear-layer vortex widths with increasing momentum flux ratio. A comparison of the normal-gravity images (frame (b) in the figures listed above) reveals similar trends. In line with the discussion of the previous section however, these trends are obscured somewhat by the "smearing" or elongation of the shear-layer vortices noted in the images acquired in the downstream imaging location.

Image Sequence Comparisons

Figure 4.5 – Figure 4.7 show representative PLMS flow-visualization image sequences taken at the lower imaging location for each of the three normal- and low-gravity cases studied. Sequential frames in these figures are separated in time by 2.78 *ms*, which corresponds to every fifth image acquired by the camera during an experiment run. Unlike the images shown in Figure 4.2 – Figure 4.4, the images in this sequence were cropped around the edges for a more compact display. It is clear from these images that the large-scale motion of the jet is fully time-resolved, even in the near field.

Figure 4.8 – Figure 4.10 show representative PLMS flow-visualization image sequences taken at the upper imaging location. The time between sequential frames in these figures is somewhat longer than before, at 5.55 *ms*, which corresponds to every tenth image acquired by the camera (at 1.8 *kHz*). The longer time-separation was chosen due to the longer fluid timescale in that region. As was done in the lower imaging location, the images in these figures were cropped for compactness of display. The images were cropped to identical sizes for each of the figures. Due to the different depths of penetration of the jet into the crossflow, the field of view of the two image sequences in each figure was chosen such that the jet falls in the center. Thus, the physical location of the images varies from figure to figure, but does not vary within a given figure.

Observations

Figure 4.5 shows a representative PLMS flow-visualization image sequence taken at the lower imaging location for the $r = 7$, $Re = 3350$ JFICF case. The images in this sequence were cropped such that the dimensions in the horizontal and vertical directions are 118 *mm* and 103 *mm* (37 and 32.5 jet-exit diameters) respectively. These image sequences show several subtle but interesting flow-field characteristics which are not obvious when examining single flow-visualization images such as those discussed in the previous section.

Figure 4.5(a) illustrates a characteristic feature seen repeatedly throughout both the normal- and low-gravity JFICF. As expected, shear-layer vortices are seen to form periodically in the near-field of the jet and convect downstream, growing in diameter, interacting and coalescing as they go. The windward-side vortices are seen to rotate clockwise and the leeward-side ones counter-clockwise. The shear-layer vortices however show a significant fore-aft asymmetry. This asymmetry appears in both the size and rate of rotation of the vortices. One example of such a fore-aft asymmetry in the shear-layer vortices is highlighted in frames 1 – 4 of Figure 4.5(a). In these frames the windward- and leeward-side vortices are indicated with red and yellow arrows, respectively. It is clear from these images that whereas the windward side vortex remains relatively compact as it moves downstream, the leeward-side vortex grows substantially in diameter. The lower of the two highlighted vortices on the leeward side also develops a loop-like appearance with downstream distance. The upper vortex has such an appearance throughout the image sequence. Such a loop-like expansion of the shear-layer vortex is also apparent in frames 5 – 10 of Figure 4.5(a). The rapid expansion of the leeward-side shear-layer vortices is accompanied by a simultaneous decay in local seed-particle density. Although perhaps not immediately apparent from the image sequence, close inspection of the flow-visualization movies revealed a significant reduction in the rate of rotation of the leeward-side vortices during and after their rapid expansion. Similar windward vs. leeward-side vortex asymmetry is apparent in various planar flow-visualization images (PLMS and acetone PLIF) of non-reacting JICF (Smith and Mungal, 1998, Hasselbrink, 1999 and 2001b, Su and Mungal, 2004). The rapid loop-like expansion of leeward-side vortices is not apparent in these images, however as noted previously, such features are more obvious in time-resolved image sequences.

The fact that similar leeward-side behavior is apparent in flows with no heat-release indicates that the phenomenon is related to the basic fluid dynamics of the jet/crossflow interaction and is not solely a heat-release effect. One possible explanation for the leeward-side behavior noted above is an asymmetry in the mean strain field of the JFICF. One would expect the windward side of the jet to see a sheet-forming strain-field which would tend to thin down the reaction zone on that side. With the twin lobes of the counter-rotating vortex pair meeting on the leeward side of the jet one may expect a similar sheet-forming strain-field there. This strain field would be oriented in a direction approximately perpendicular to the one on the windward side. A sheet-forming strain field aligned with the *x-y* symmetry plane of the jet is consistent with the more rapid leeward-side shear-layer vortex expansion noted above. The sheet-forming strain field seen by the windward side would result in a thin flame sheet surrounding the jet-fluid there. Consistent with the work of Takagi *et al.* (1980), one would expect the presence of the flame at the interface between the jet and crossflow to effectively shield the (more turbulent) jet-fluid and thus allow the windward-side vortices to maintain the higher rate of rotation noted above.

There is reason to believe the phenomenon described above is significantly affected by heat-release. As mentioned previously, several researchers (Birch *et al.*, 1989, Kadota *et al*. 1990, Tsue *et al*. 2000, 2001) have noted significant fore-aft asymmetry in the thermochemical structure of a turbulent JFICF. These studies have shown that the temperature profile of a turbulent JFICF is biased toward the leeward side of the jet. Kadota *et al.* (1990) interpreted this asymmetry as being the result of the stirring action of the CVP creating a well-mixed region in the wake of the flame where the chemical reaction proceeds very actively. The resulting high-temperature region on the leeward-side of the jet would cause volumetric expansion in the gas there. The significantly reduced seed-particle density seen in that region of the images is consistent with such an expansion. It should be noted that the nonreacting JICF flow-visualization images of Smith and Mungal (1998), Hasselbrink (1999) and Su and Mungal (2004) appear to show significantly higher jet-fluid concentration on the leeward side of the jet than is apparent in the image sequences of Figure 4.5. This supports the argument that the reduced seed-particle concentration seen in that region of the PLMS images above is the result of volumetric expansion caused by heat-release.

Frequent interaction and coalescence of the shear-layer vortices was seen in the flow-visualization movies. Although such interactions are difficult to pick out in individual images, they become quite clear in time-resolved image sequences. One such interaction is highlighted in frames 1 – 7 (indicated by the arrows overlaid on the images) of Figure 4.5(a). Interaction and coalescence of the shear-layer vortex structures was seen in all cases, in both normal and low-gravity. This phenomenon has been directly observed in previous shear-layer studies (Brown and Roshko, 1974) and is a well understood characteristic of shear-layer vortex dynamics. It is noted here in relation to the effect such interactions have on the elongation and distortion of the shear-layer structures. As can be seen from the vortex-interaction shown frames 1 – 7 of Figure 4.5(a), (highlighted by white arrows) these interactions may result in cross-stream-wise distortion of the shear-layer vortices but typically do not preferentially distort the structures in the vertical direction. A similar vortex interaction event is highlighted in frames 8 - 12 of Figure 4.5(b) (taken in the lower imaging location where it is reasonable to assume the flow is momentum-dominated), showing that this vortex-interaction-induced cross-stream distortion and elongation is characteristic of momentum-dominated flows, regardless of gravity level.

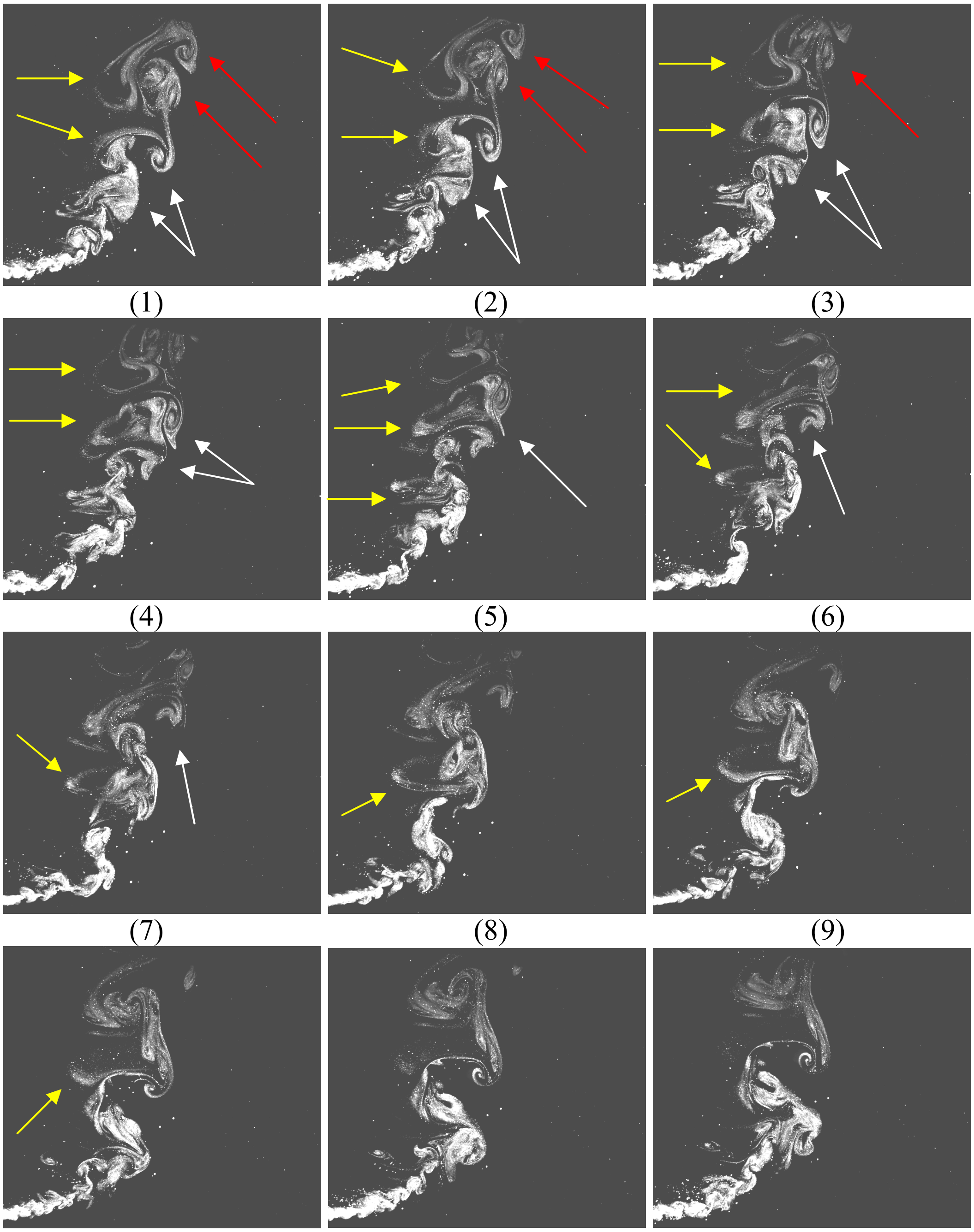

(1) (2) (3)

(4) (5) (6)

(7) (8) (9)

(10) (11) (12)

(a) See next page for caption

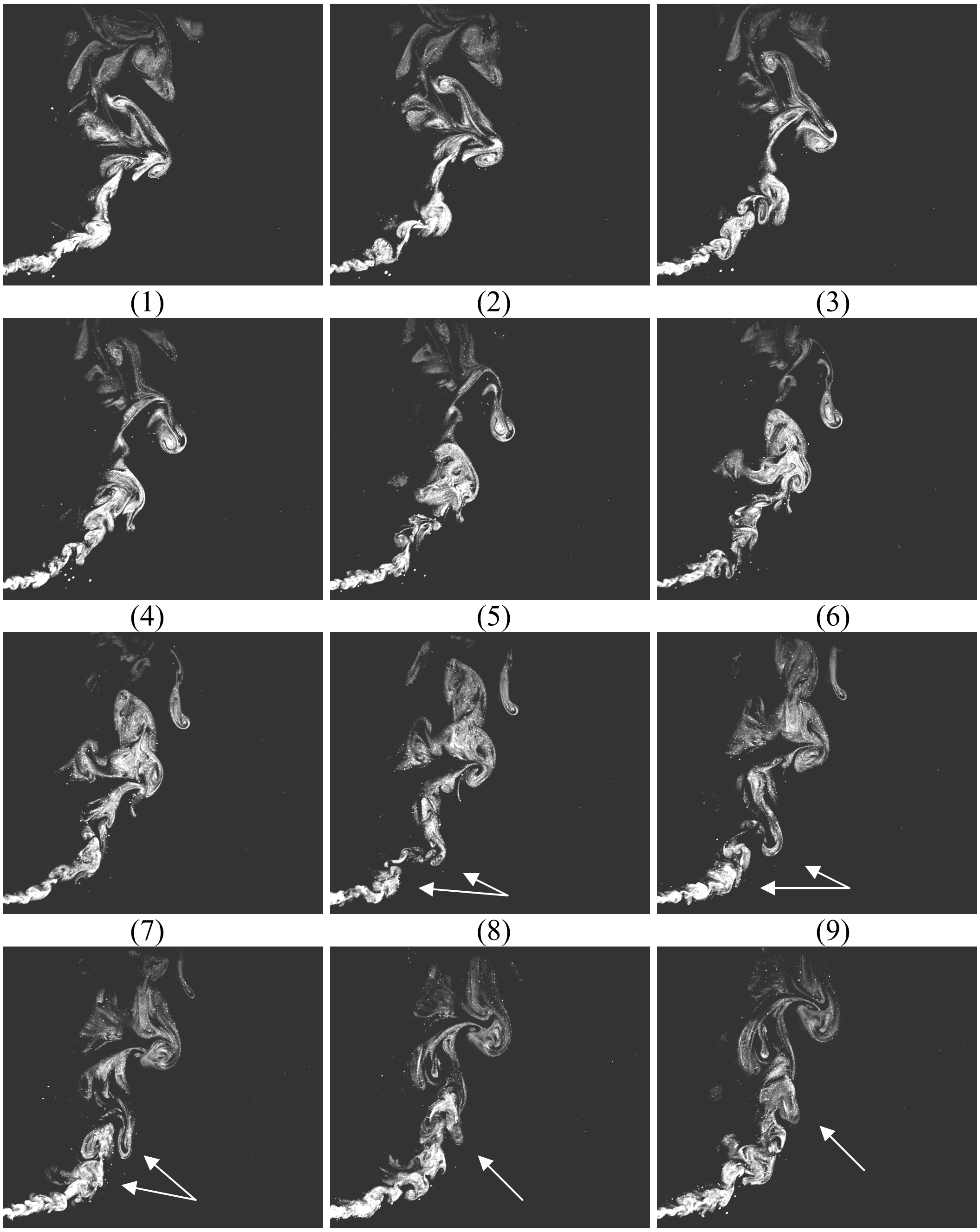

(1) (2) (3)

(4) (5) (6)

(7) (8) (9)

(10) (11) (12)

(b)

Figure 4.5 Cinematographic PLMS flow-visualization image sequence of the $r = 7$, $Re = 3350$ turbulent JFICF. Time-delay between images is 2.78*ms*, which corresponds to every fifth frame acquired by the camera during this portion of the experiment. (a) Low-gravity (b) Normal-gravity.

Figure 4.6 shows a representative PLMS flow-visualization image sequence taken at the lower imaging location for the $r = 10$, $Re = 4800$ case. The images in this sequence were cropped to the same dimensions as those in Figure 4.5.

The image sequences in Figure 4.6 display generally similar characteristics to those seen in Figure 4.5. As can be seen in the circled regions of frames 2 – 9 of Figure 4.6(a) and 6 - 11 of Figure 4.6(b), the shear-layer vortices in the $r = 10$ case display rapid, loop-like expansion of the leeward-side vortices similar to that noted in Figure 4.5. Although it may not be immediately clear from the image sequences, close inspection of the flow-visualization movies for this case revealed that the windward-side vortices tend to maintain their small size and high rate-of-rotation further downstream than do the vortices on the leeward-side. This is consistent with similar behavior previously noted in the image sequences of Figure 4.5.

Frames 1 – 6 of Figure 4.6(b) show another shear-layer vortex coalescence event. In this event, the smaller upstream vortex appears to be caught and rolled up around the outer edge of the (apparently) stronger downstream vortex. Whereas the (initially) upstream vortex is severely stretched in the coalescence event, the downstream vortex appears to show little distortion as a result of it.

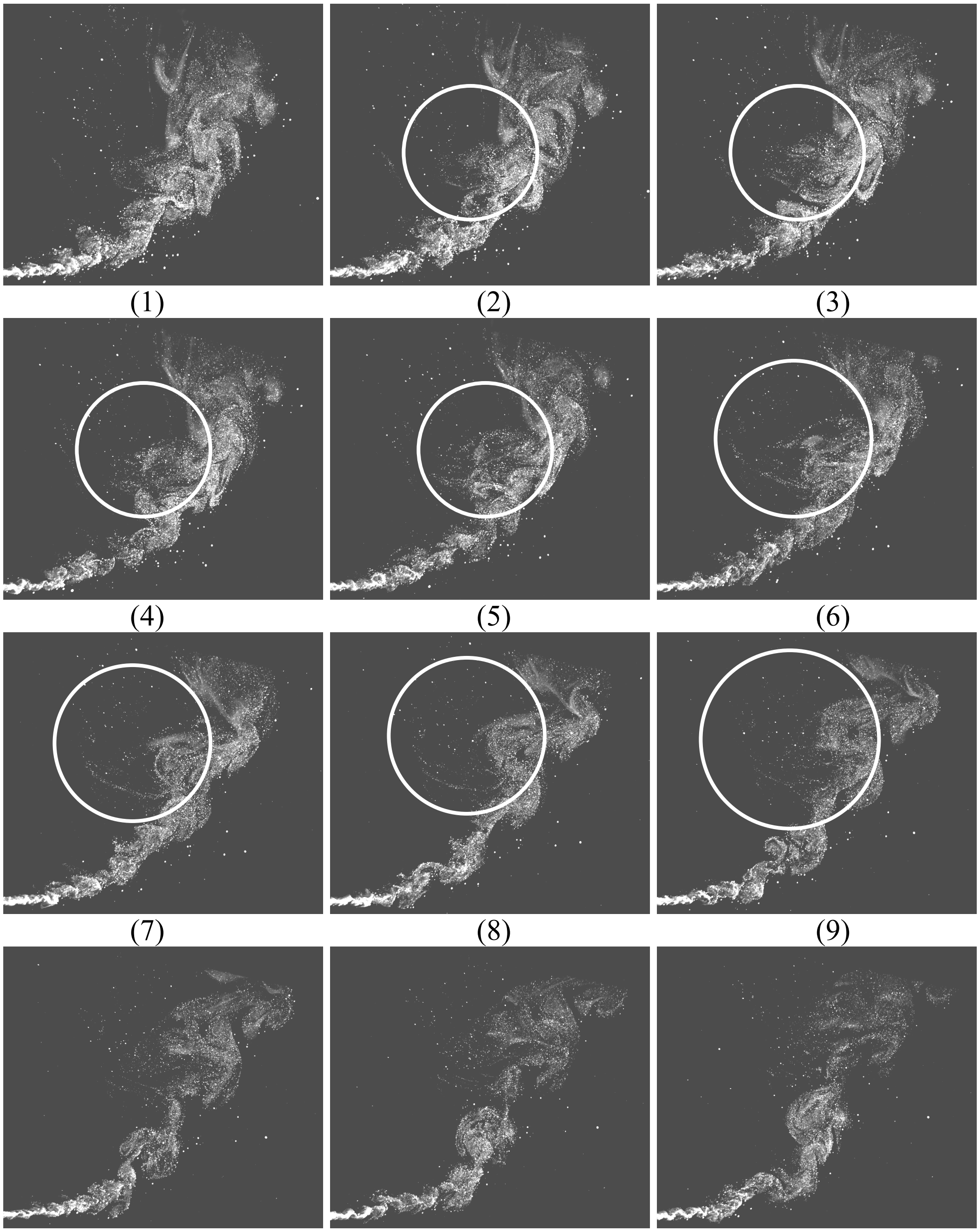

(1) (2) (3)

(4) (5) (6)

(7) (8) (9)

(10) (11) (12)

(a) See next page for caption

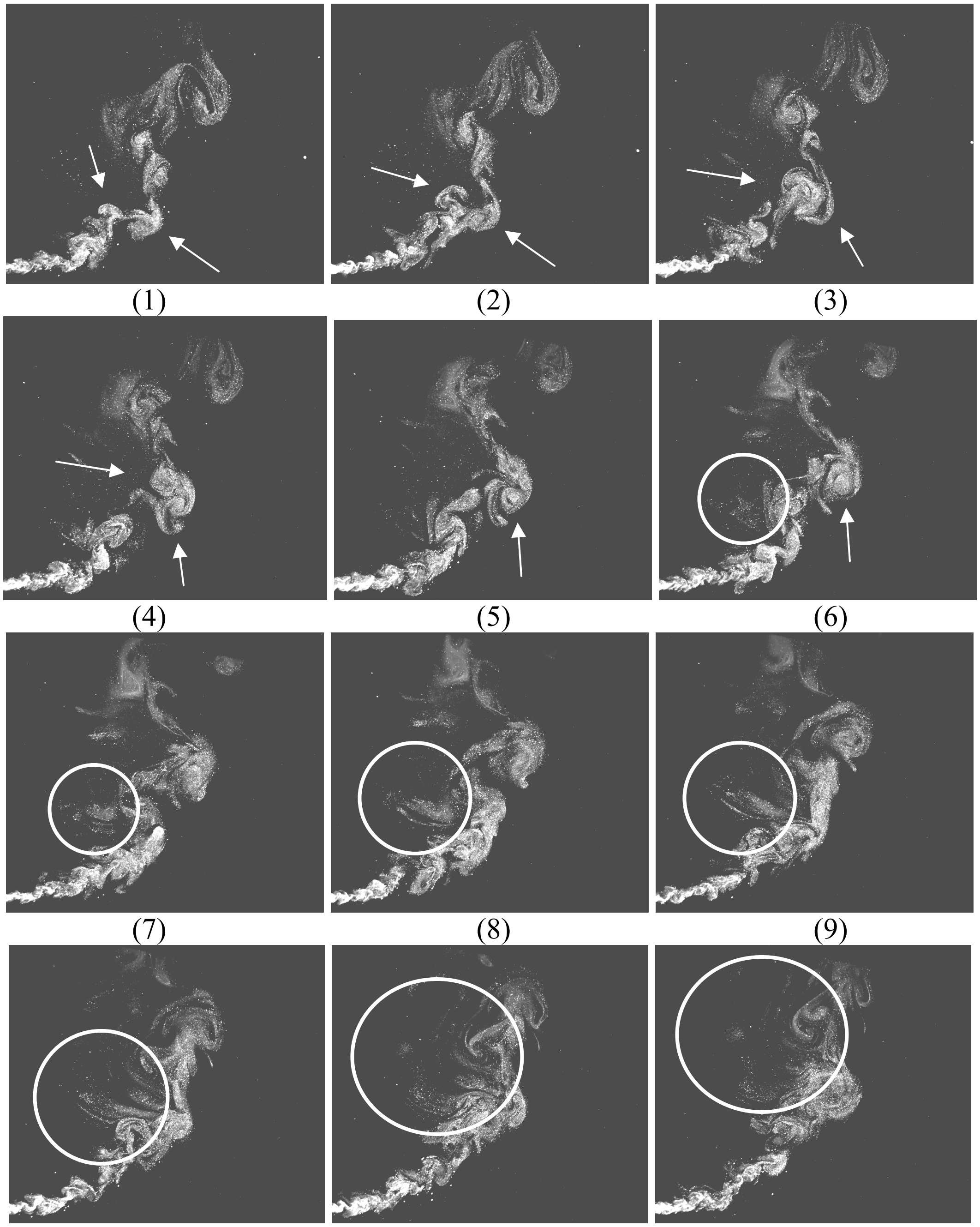

(1) (2) (3)

(4) (5) (6)

(7) (8) (9)

(10) (11) (12)

(b)

Figure 4.6 Cinematographic PLMS flow-visualization image sequence of the $r = 10$, $Re = 4800$ turbulent JFICF. Time-delay between images is 2.78 *ms*, which corresponds to every fifth frame acquired by the camera during this portion of the experiment. (a) Low-gravity (b) Normal-gravity

Figure 4.7 shows representative PLMS flow-visualization images taken at the lower imaging location for the $r = 11.5$, $Re = 5500$ JFICF case. The images in this sequence were cropped to the same dimensions as those in Figure 4.5 and 4.6.

These image sequences reveal a fore-aft asymmetry in the shear-layer vortices similar to that seen in previous two figures. However, this asymmetry is evident primarily in the fact that individual shear-layer vortices are only clearly distinguishable on the windward-side of these jets. On the leeward side, the shear-layer vortices are much less obvious in the images if they exist at all. The images in Figure 4.7 appear to show a more turbulent flow than those of the previous two figures.

The circled areas in frames 5 – 12 of Figure 4.7(b) show the expansion of a leeward side vortex with increasing downstream distance. The reduction in seed particle density associated with this expansion is particularly apparent in these frames. The expansion does not appear to exhibit the same elongated, loop-like structure seen in similar leeward-side vortex expansions noted in previous figures. This could be the result of the low-seed density of this vortex though. In any case, the asymmetric vortex expansion is seen in all three JFICF cases and appears to be a general characteristic of the flow under these conditions. As mentioned previously, this asymmetry is seen in flow-visualization of both (the present) JFICF and nonreacting JICF. As can be seen from the very low seed particle densities, in the case of the JFICF the phenomenon also appears to be affected by volumetric expansion associated with the asymmetric temperature profile (noted by previous researchers) caused by the heat-release of the flame.

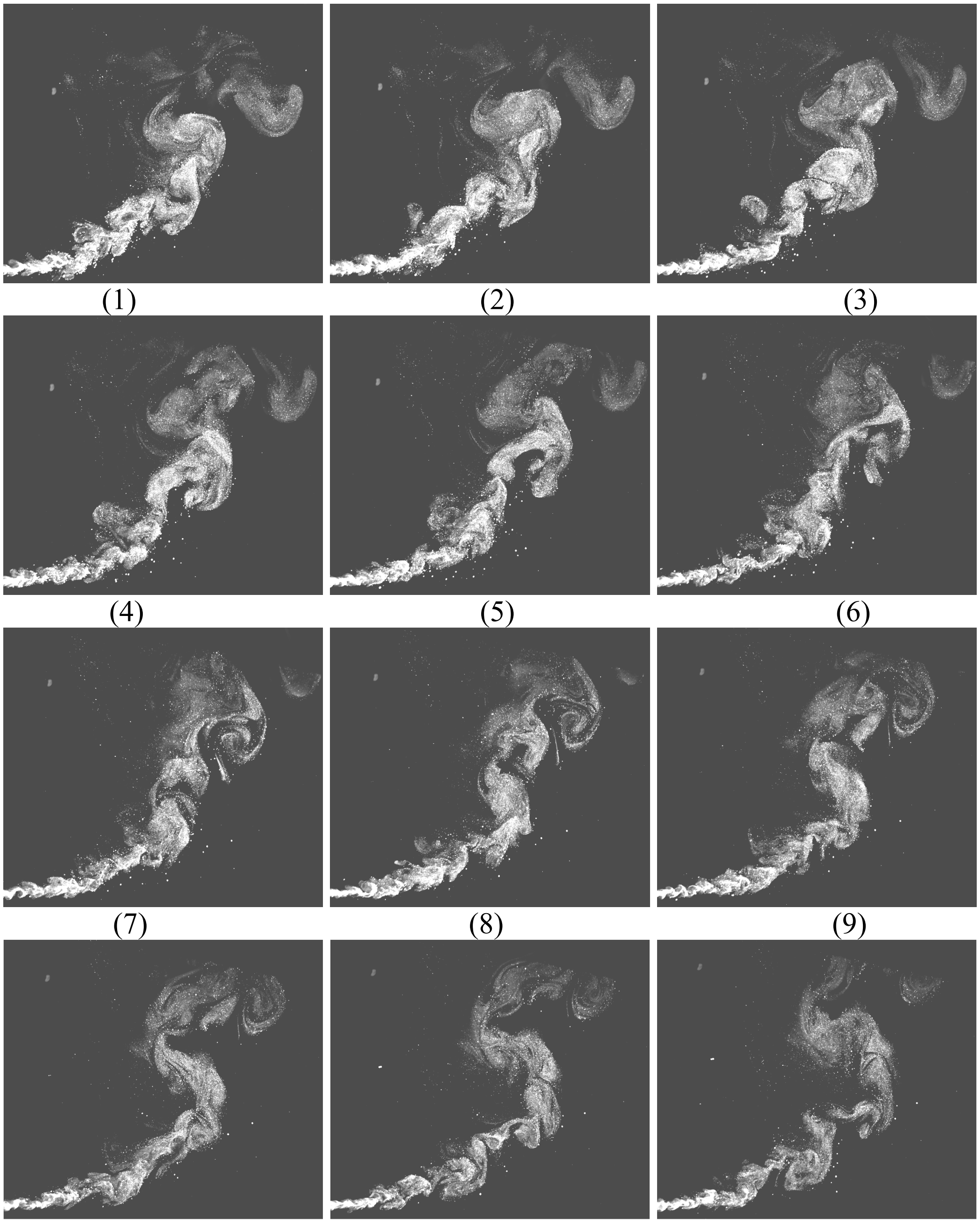

(1) (2) (3)

(4) (5) (6)

(7) (8) (9)

(10) (11) (12)

(a) See next page for caption

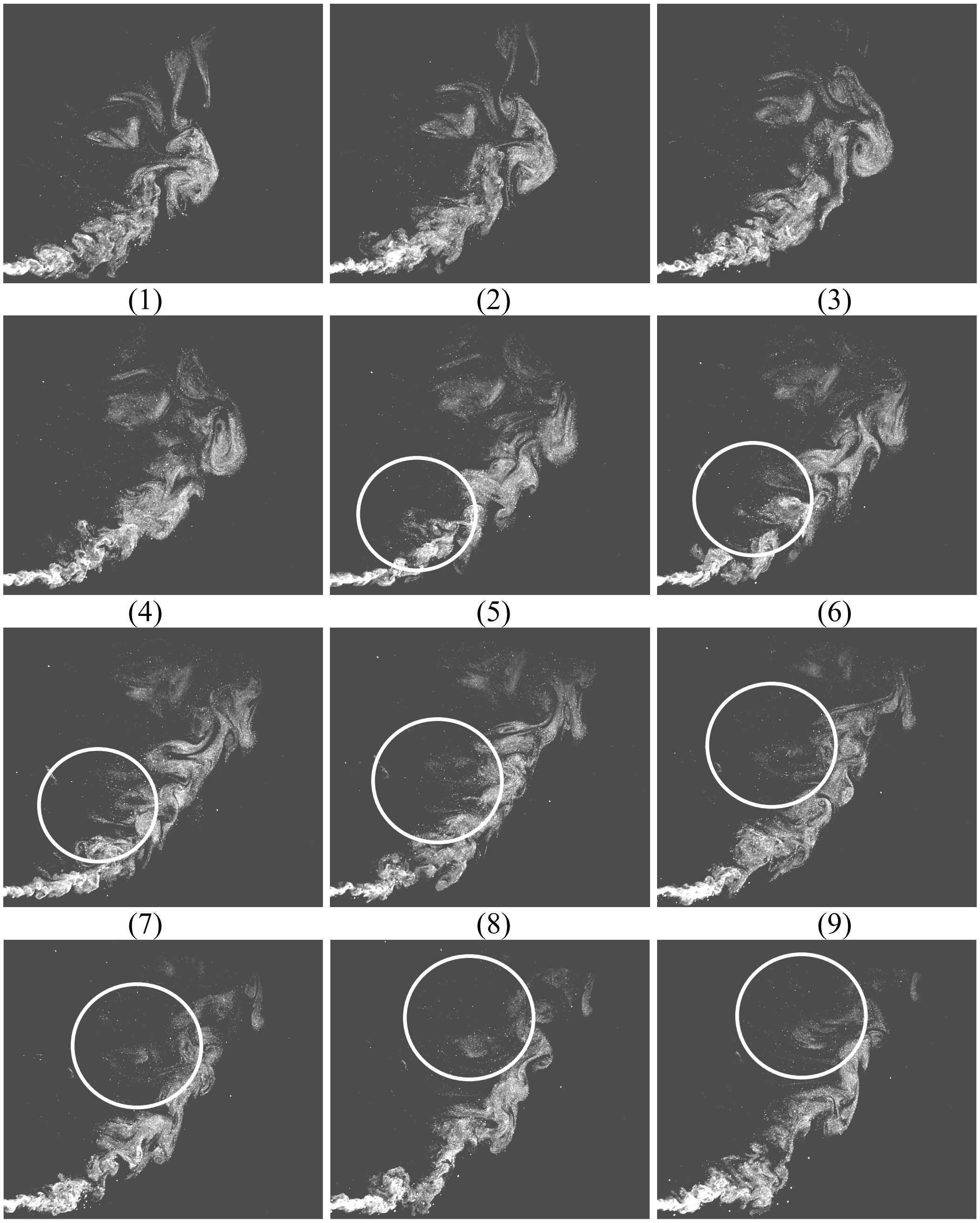

(1) (2) (3)

(4) (5) (6)

(7) (8) (9)

(10) (11) (12)

Figure 4.7 Cinematographic PLMS flow-visualization image sequence of the $r = 11.5$, $Re = 5500$ turbulent JFICF. Time-delay between images is 2.78 *ms*, which corresponds to every fifth frame acquired by the camera during this portion of the experiment. (a) Low-gravity (b) Normal-gravity

Upper Imaging Location

Figure 4.8 through Figure 4.10 show representative PLMS flow-visualization image-sequences taken at the upper imaging location for each of the three normal- and low-gravity JFICF studied.

Close inspection of image sequences (a) and (b) (low- and normal-gravity cases, respectively) of Figure 4.8 reveals several characteristic flow-features. The low-gravity image sequence shows a series of shear-layer vortices which appear relatively smooth and round in shape. These vortices (highlighted by arrows overlaid on the image sequences) are seen to maintain roughly the same shape as they convect downstream through the field of view. They do not appear to distort or elongate as they pass by. These structures may be described as reasonably coherent in nature. The normal-gravity image sequence predominantly shows longer, thinner vortices. As before, these vortex structures are highlighted by arrows overlaid on the image sequences. As noted previously, the primary elongation of these structures is in the vertical direction. The red arrows overlaid on frames 9 – 12 of Figure 4.8(b) capture one shear-layer vortex distortion very clearly as the structure convects through the field of view. Similar elongation and distortion of shear-layer structures occurred repeatedly throughout the PLMS flow-visualization movie sequences of all normal-gravity experiment runs for this case. Compared to the low-gravity case, the shear-layer vortices in this image sequence appear to exhibit significantly less coherence. Consistent with the images of normal-gravity JFICF luminosity shown in Chapter 3, the normal-gravity flame also appears to have a smaller overall jet-width.

Similar characteristics are visible in Figure 4.9, which corresponds to the $r = 10$, $Re = 4800$ case. Whereas the shear-layer vortices in the low-gravity images (sequence (a)) appear quite round and uniform in shape, the images of the normal-gravity flames show signs of elongation in the vertical direction. In this case though, the vortices show greater roundness and uniformity of shape in normal-gravity than they did for the $r = 7$ case. The images in (a) and (b) of Figure 4.9 also show a noticeably wider overall jet-width in low-gravity than in normal. This is consistent with the observations based on flame-luminosity described in Chapter 3.

Figure 4.10 shows images taken from the highest momentum-flux ratio ($r = 11.5$) case. As can be seen from the several representative shear-layer vortices highlighted with white arrows overlaid on the images, in low-gravity the shear-layer vortices appear relatively smooth and round in shape. They do not appear to distort significantly as they convect through the field of view. The image sequence for the normal-gravity flame (sequence (b)) reveals shear-layer vortex behavior that is more complex and difficult to interpret. For example, the large scale vortex structure (highlighted by the white arrows overlaid on the images) seen convecting up through Frames 1, 2 and 3 has a relatively uniform and round (almost circular) profile and appears to convect downstream without significant distortion in the vertical direction. Frames 4 – 8 show what appear to be the elongation and distortion in the vertical direction similar to that previously noted in the lower momentum cases. These structures are highlighted with yellow arrows. In the last three frames of the sequence one sees what appear to be more uniform, coherent shear-layer vortex structures. This image sequence was chosen for display in Figure 4.10 as it represents a general trend observed in the PLMS movie sequences for the normal-gravity, $r = 11.5$, $Re = 5500$ case. In the PLMS movie sequences for this case, the flame displayed characteristics previously associated with both the normal- and low-gravity JFICF. The movies showed the behavior of the large-scale flame structure oscillates between the uniformly round and coherent-looking vortices characteristic of low-gravity flames and the elongated and distorted vortices previously noted only in normal-gravity. Although difficult to measure quantitatively, manual inspection and interpretation of the movie sequences reveals that in this case the flame more often displays the more uniform, coherent structures characteristic of low-gravity (or rather, momentum-dominated) JFICF than the elongated, vertically distorted structures characteristic of the normal-gravity flames. The observation suggests that for $\xi_y \approx 3.1$, $r = 11.5$, $Re = 5500$, the large-scale structure of the turbulent JFICF is nearing but has not quite reached a momentum-dominated forced convection limit.

Frames 10 – 12 of Figure 4.10(a) illustrate a phenomenon alluded to earlier, wherein shear-layer vortex structures appear to show a greater tendency to distort in the cross-stream (*i.e.* approximately perpendicular to the direction of the local jet-centerline) direction. Such a cross-stream shear-layer vortex distortion is indicated by the red arrows overlaid on the image. This particular distortion appears to be related to the interaction of two shear-layer vortices, with a smaller diameter one pushing up into the upper one from below, causing it to distort in the cross-stream direction. As noted previously, although the large-scale shear-layer vortices are seen to distort and elongate in a manner similar in some ways to that of the normal-gravity JFICF, the distortion generally appears related to vortex coalescence. The elongation and distortion of the normal-gravity shear-layer structures in the vertical direction appear exclusively linked to buoyancy.

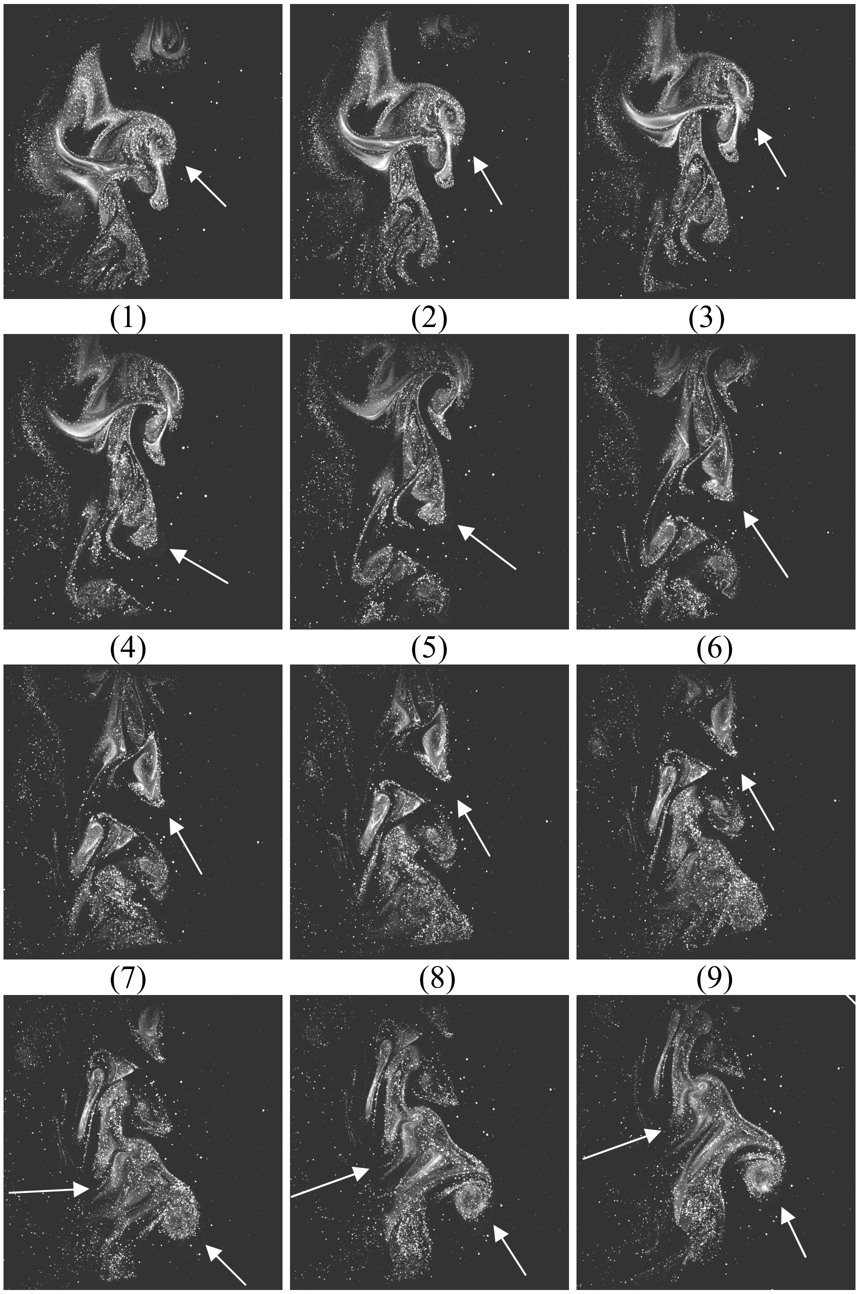

(1) (2) (3)

(4) (5) (6)

(7) (8) (9)

(10) (11) (12)

(a) See next page for caption

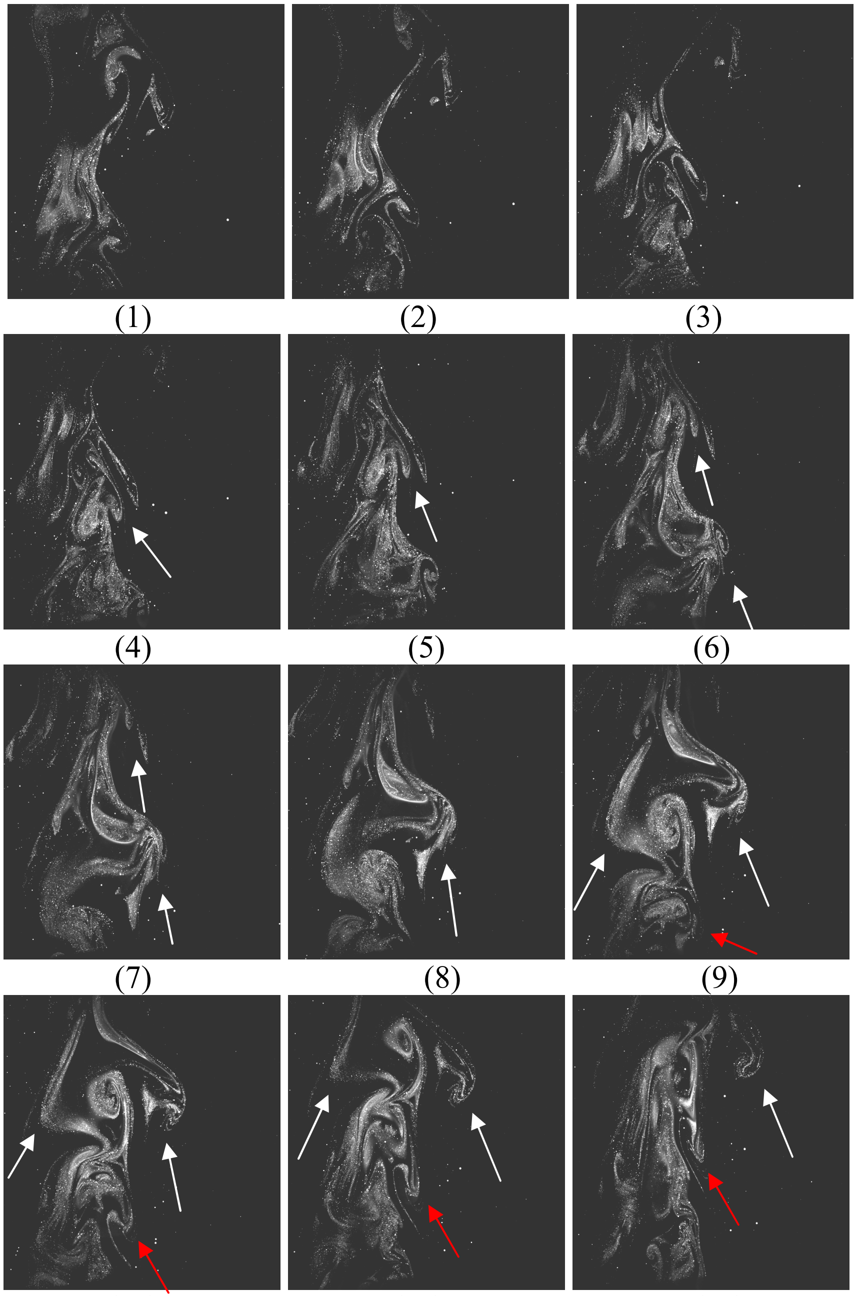
(1) (2) (3)

(4) (5) (6)

(7) (8) (9)

(10) (11) (12)

(b)

Figure 4.8 Cinematographic PLMS flow-visualization image sequence of the $r = 7$, $Re = 3350$ turbulent JFICF taken at the downstream imaging location. Time-delay between images is 5.56 *ms*, which corresponds to every tenth frame acquired by the camera during this portion of the experiment. (a) Low-gravity (b) Normal-gravity.

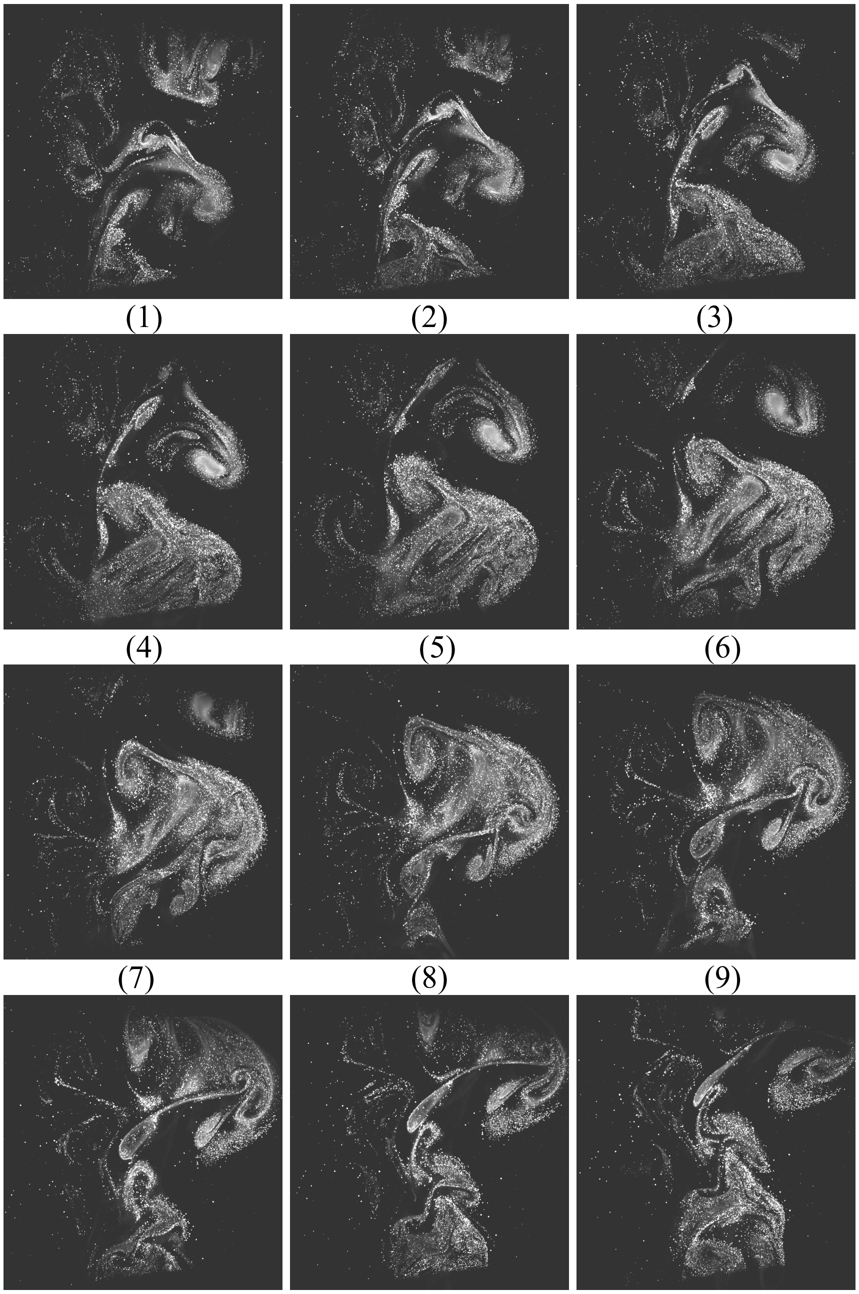

(1) (2) (3)

(4) (5) (6)

(7) (8) (9)

(10) (11) (12)

(a) See next page for caption

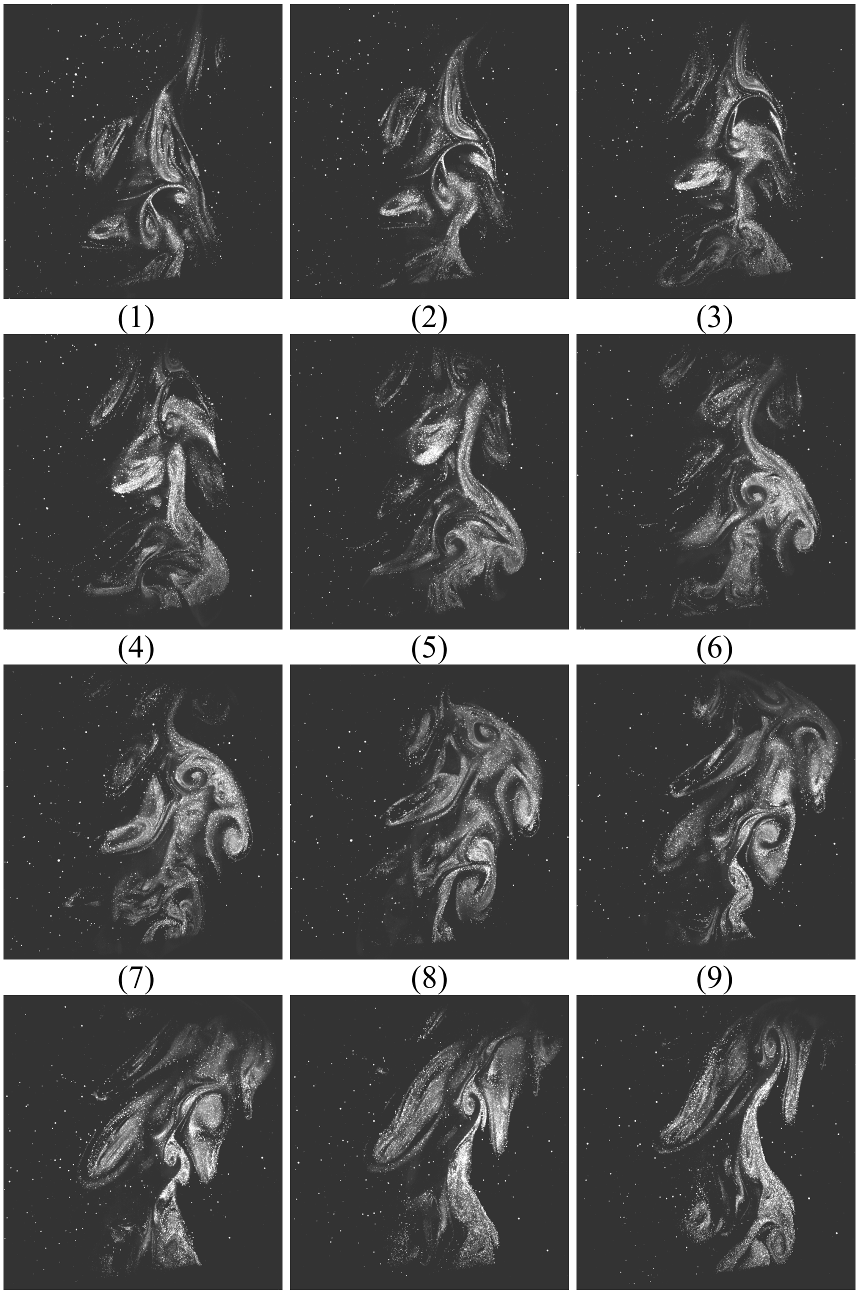

(1) (2) (3)

(4) (5) (6)

(7) (8) (9)

(10) (11) (12)

(b)

Figure 4.9 Cinematographic PLMS flow-visualization image sequence of a normal-gravity, $r = 10$, $Re = 4800$ turbulent JFICF taken at the downstream imaging location. Time-delay between images is 5.56 *ms*, which corresponds to every tenth frame acquired by the camera during this portion of the experiment.

(1) (2) (3)

(4) (5) (6)

(7) (8) (9)

(10) (11) (12)

(a) See next page for caption

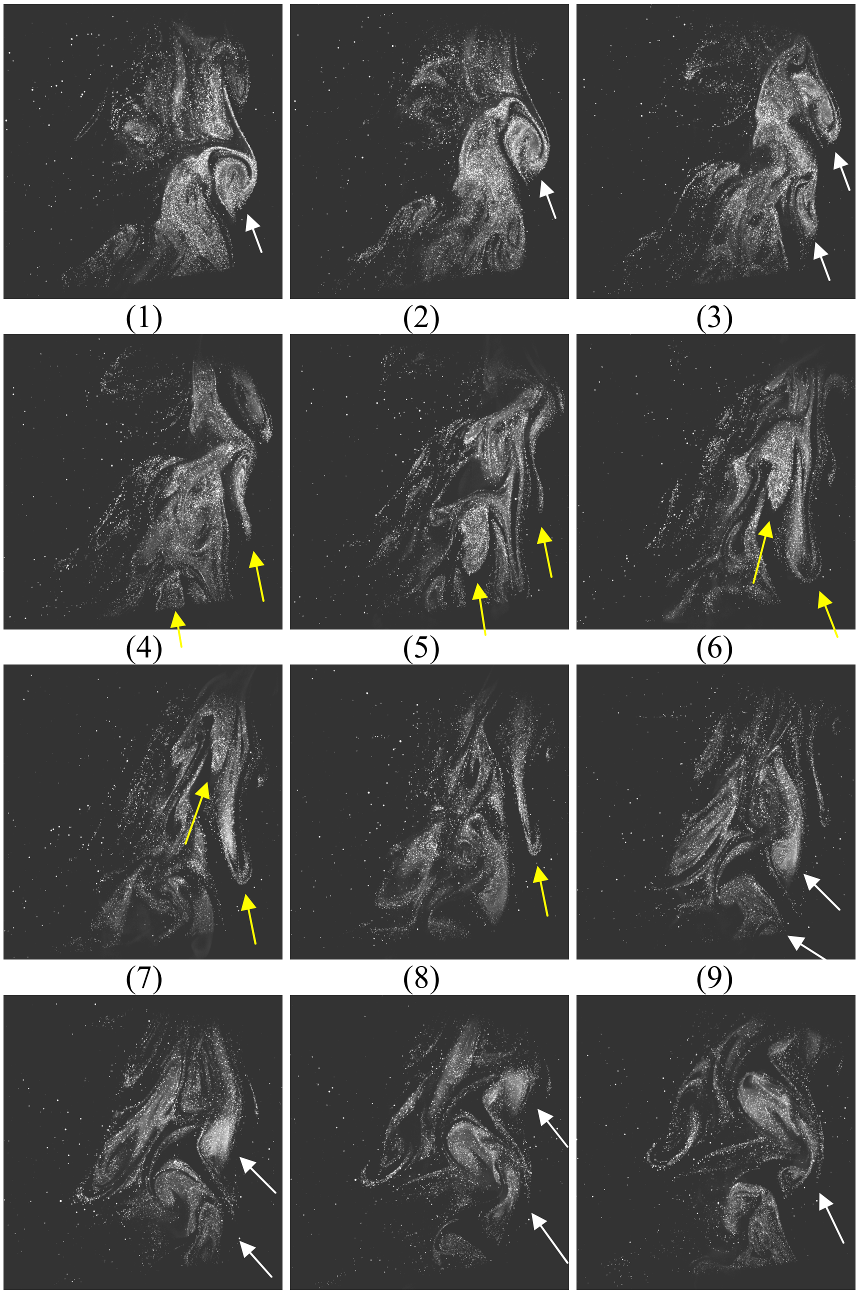

(1) (2) (3) (4) (5) (6) (7) (8) (9) (10) (11) (12)

(b)

Figure 4.10 Cinematographic PLMS flow-visualization image sequence of a normal-gravity, $r = 11.5$, $Re = 5500$ turbulent JFICF taken at the downstream imaging location. Time-delay between images is $5.56\,ms$, which corresponds to every tenth frame acquired by the camera during this portion of the experiment. (a) Low-gravity (b) Normal-gravity

STATISTICAL DATA ANALYSIS

Mie scattering from non-reactive tracer particles has been used successfully in previous studies to make both point (Ebrahami and Kleine, 1977) and planar (Lysaght *et al.*, 1982, Rehm and Clemens, 1999) measurements of the conserved scalar fields in turbulent jet-flames. The technique has also been successfully applied in the low-gravity environment of a drop-tower (Idicheria, 2003) to the study of the scalar-field in non-premixed hydrocarbon jet-flames. In this study, the methodology and simplifying assumptions of Ebrahimi and Kleine (1977) and Kennedy and Kent (1979) were used to deduce mixture fraction decay scaling along the centerline trajectory of the turbulent non-premixed JFICF. This methodology, its assumptions, simplifications and limitations will be outlined in greater detail in the upcoming paragraphs.

The intensity ("*I*") of the Mie scattering signal is linearly dependent upon the total number density of scattering particles present in the probe-volume. Assuming the seed particles are uniformly distributed and originate only within the jet fluid, the number density of seed particles in the probe volume is dependent upon the local mixture fraction of (seeded) jet fluid and the local fluid density. Normalized by jet-exit conditions, this may be expressed (Kennedy and Kent, 1979) mathematically as

$$\frac{I}{I_o} = \frac{\zeta\rho}{\rho_0} \tag{4.1}$$

where I and ρ are the local values of Mie scattering intensity and fluid density respectively, I_o and ρ_o are their values at the jet-exit and ζ is the local mixture fraction of jet fluid.

The mixture fraction of jet fluid in the probe volume is defined as

$$\zeta = \frac{\text{Mass of fluid in probe volume originating in jet}}{\text{Total mass of fluid in probe volume}} \tag{4.2}$$

The mixture fraction is related to the mole fraction as

$$\zeta = \frac{\chi M_0}{\chi M_0 + (1-\chi)M_\infty} \tag{4.3}$$

or alternatively

$$\zeta = \frac{1}{1+\left(\frac{1}{\chi}-1\right)\frac{M_\infty}{M_0}} \tag{4.4}$$

where χ is the local mole fraction of jet fluid and M_∞ and M_0 are the molecular masses of the ambient and jet-fluids respectively.

In the case of a non-reacting jet issuing into a fluid of equal temperature, Equation 4.1 simplifies to

$$\frac{I}{I_0} = \zeta \tag{4.5}$$

In the case of non-reacting jet issuing into a fluid of equal molecular mass (eg. air into air), it simplifies still further to

$$\frac{I}{I_0} = \chi \tag{4.6}$$

In the case of a flow with heat release though, certain assumptions must be made in order to account for the density ratio found in Equation 4.1. As mentioned above, the methodology of Kennedy and Kent (1979) was followed, which makes the assumption of equal diffusivities and equilibrium chemistry. This results in a monotonic relation between the normalized intensity ratio (I/I_0) of the Mie scattering signal and mixture fraction. With the assumption of equilibrium chemistry, the normalized intensity of the Mie scattering signal (I/I_0) was mapped to mixture fraction (ζ) as shown in Figure 4.11. The equilibrium chemistry solver STANJAN was used to generate this mapping. It should be noted that this correction is particularly sensitive at low values of intensity ratio and care should be taken in interpreting the computed results in these regions.

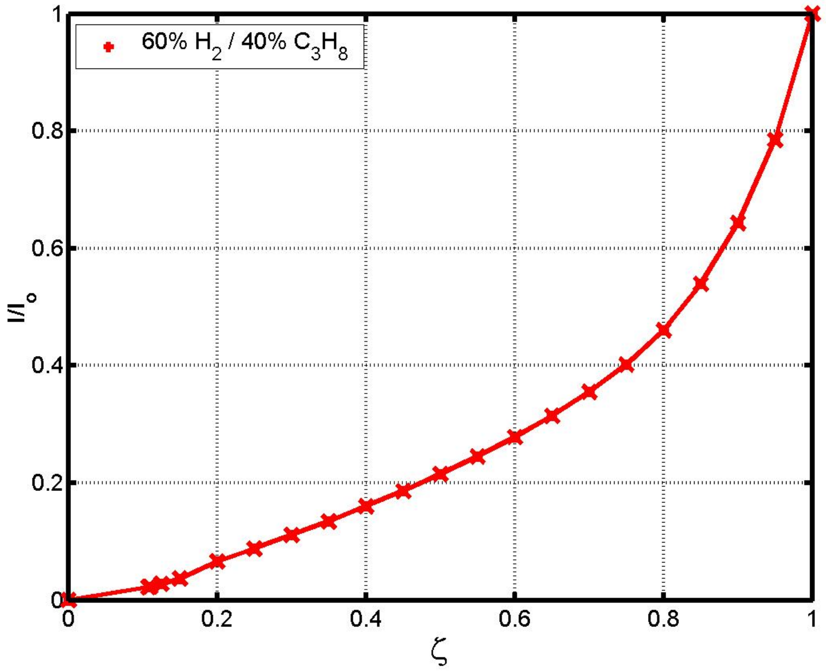

Figure 4.11 Relationship between jet-fluid mixture fraction and the normalized Mie Scattering signal.

In order for the alumina particles to be used as a marker of the jet-fluid, it is essential that they be able to accurately track both the mean and instantaneous fluctuations the fluid flow. The Stokes number provides a measure of how well a given particle tracks fluid motion. The Stokes number is defined as

$$St = \frac{\tau_p}{\tau_f} \tag{4.7}$$

where τ_p and τ_f are characteristic timescales for a tracer particle and the fluid flow, respectively. A direct numerical simulation study (Samimi and Lele, 1997) concluded that particles will accurately track the instantaneous fluid fluctuations provided their Stokes number is below 0.05.

The particle timescale, (inferred from Melling, 1997) is

$$\tau_p = \frac{\rho_p d_p^2}{18\mu}\left(1 + Kn\right) \tag{4.8}$$

where ρ_p is the density of the tracer particle material (3970kg/m^3 for Al_2O_3), μ is the dynamic viscosity, d_p is the particle diameter and Kn is the Knudsen number ($Kn = \lambda/d_p$, where λ is the mean free path). Previous work (Rehm, 1999, Hasselbrink, 1999) shows that while the alumina has a nominal particle diameter of 0.3 μm, particle agglomeration tends to generate an effective diameter closer to approximately 1 μm. As such, this larger effective diameter was used to calculate τ_p. It is assumed that the fluid at this downstream location may be approximated as being predominantly air, with a temperature of 1500 K. This gives a mean free path of $\lambda = 3.25\text{x}10^{-7} m$ and a Knudsen number of approximately 0.33. Consistent with the assumption above, the viscosity μ would be 5.40×10^{-5} $kg/m\text{-}s$. Thus the particle response time is found to be 5.4 μs.

The fluid timescale is defined as

$$\tau_f = \frac{\delta}{u_c} \tag{4.9}$$

where δ is a characteristic length-scale for the jet at that location and u_c is the centerline velocity. In the case of a straight jet, the appropriate length-scale for the definition above is the jet half-width. A more appropriate length-scale for the dual-lobed JFICF would appear to be $(A_{cs})^{1/2}$, where A_{cs} is the cross-sectional area of the jet. Rao and Brzustowski (1982) found the area of a turbulent propane JFICF scales as

$$\frac{A_{cs}}{(rd)^2} = 2.33\left(\frac{y}{rd}\right)^{1.15} \tag{4.10}$$

Using the relation above,

$$\tau_f = \frac{\left(2.33\,(rd)^2\left(\frac{y}{rd}\right)^{1.15}\right)^{1/2}}{u_c} \tag{4.11}$$

Using the scaling laws derived by Hasselbrink (1999) to estimate u_c for each case, τ_f was determined to be $\approx 3\times10^{-2}s$ at a downstream location of $y/d = 20$ (63.5 *mm* from injector). The Stokes number for the flow at this location thus lies between 1.75×10^{-4} and 1.8×10^{-4}, which surpasses the $St < 0.05$ requirement set forth by Samimi and Lele (1997).

Differential diffusion is also known to affect the accuracy of PLMS-based mixture fraction measurements. The issue of differential diffusion arises from the large difference in diffusivities of molecules and the (far larger) alumina particles. Using simultaneous Lorentz-Mie scattering from TiO_2 particles and planar laser-induced fluorescence of biacetyl vapor, Long *et al*. (1993) determined that molecular diffusion tends to smooth out the fine-scale structure of turbulent flows and softens species gradients around the interface of large-scale eddies and the surrounding fluid. That study found that differential diffusion results in PLMS over-predicting concentration gradients at the finest scales in a laboratory scale turbulent jet. With this in mind, the present study uses only ensemble-averages of many PLMS images to determine mixture fraction decay scaling. Thus the measurements are less sensitive to this effect. Instantaneous PLMS images are only used for visualization of the large-scale structures in the flow.

Sheet correction

As mentioned in a previous section, the laser sheet used in the PLMS experiments expands from right to left in the field of view of the camera. It is also varies (thins down) in the direction perpendicular to the imaging plane. As such, the laser fluence is spatially non-uniform and thus the scattering from seed particles becomes sensitive to their location in space. In order to relate the intensity of the PLMS images to the alumina seed-particle density at the corresponding location, it was necessary to perform a sheet-correction.

A sheet correction was generated as shown in Figure 4.12. With the optics in the final configuration and secured in place in the droprig, a theatrical fog generator machine was used to fill the test section of the flow facility with a thin cloud of glycol fog. The laser sheet was passed through the fog and the camera was manually triggered to gather 2000 images (200 sets of 10 images each, acquired at 2000 *fps*). Next, the test section was purged with air to rid it of fog. Then, with the laser sheet passing through the empty test section, a set of 500 background images (50 sets of 10 images each, acquired at 2000 *fps*) was acquired. To generate the sheet correction data, the background images were ensemble averaged to create a single background image. The average background image was then subtracted from each of the sheet-correction (fog-filled) images. These (background-corrected) images were then ensemble averaged to generate an image corresponding to the average intensity variation through the field of view. The PLMS images were corrected in a similar manner, by first subtracting the mean background image, then taking the ensemble average of the images and then normalizing it with the sheet-correction image.

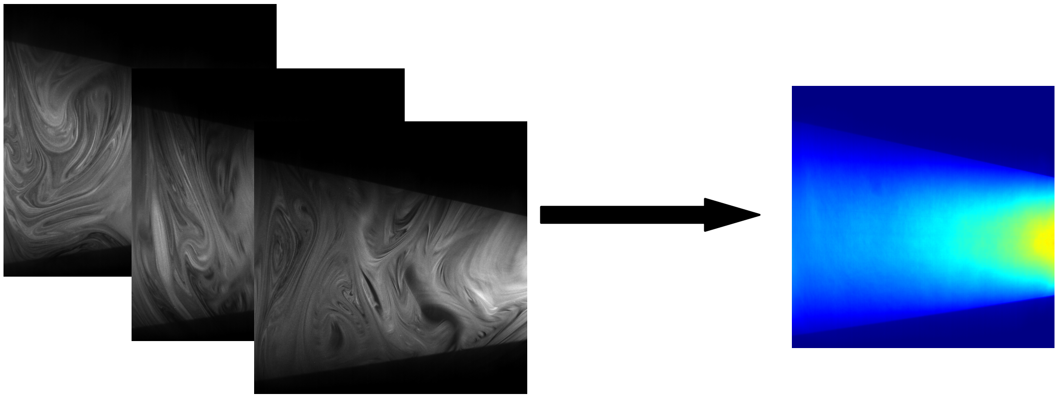

Figure 4.12 Sheet-correction technique. A set of 2000 images of a thin glycerol fog was ensemble-averaged to produce a sheet-correction image. A set of 500 background images were similarly averaged to correct for background scattering.

Mean Centerline Mixture Fraction Decay

In the technique outlined above, (for finding jet-centerline mixture fraction decay from PLMS images) it is necessary to normalize the (ensemble-average) pixel intensities of the (sheet-corrected) image with the intensity value at the jet-exit. In this study however, the field of view of the camera was offset from the wall by 12 *mm* (or approximately 3.8 *d*) due to excessive interference from laser reflection. As such, the jet-exit value was unavailable. In this study the technique was modified such that the (ensemble-average) pixel intensities were normalized with the highest jet-centerline value appearing in the ensemble-average PLMS image instead of the jet-exit value. The centerline intensity profiles thus normalized (and corrected for the aforementioned temperature effect) were plotted in log-log format and fit to the power-law relation

$$\frac{\mathrm{C}}{\mathrm{C}_0} = A\left(\frac{y}{rd}\right)^n \tag{4.12}$$

Taking the logarithm of the left and right hand side of the the power-law

$$\ln\left(\frac{C}{C_0}\right) = \ln\left(A\left(\frac{y}{rd}\right)^n\right) \tag{4.13}$$

one gets

$$\ln(C) - \ln(C_0) = \ln(A) + n\ln\left(\frac{y}{rd}\right) \tag{4.14}$$

Noting that both A and C_0 are constants it is clear that an incorrect value of C_0 will lead to an incorrect value of A. This will in turn appear as an offset in the log-log plot. It will not, however, change the value of the exponent n. The exponent n determines the slope of the decay curve in the log-log plot.

Only those images from the lower-imaging location were analyzed for mixture fraction decay scaling. This was due to the unexpectedly high levels of soot particle-density in the flame at the upper imaging location. Although the soot luminosity was effectively eliminated from the images through the combination of electronic shutter and Schott-glass filter, at the upper imaging location the flame frequently had sufficient soot density to cause substantial scattering of the laser-light. As the scattered light was at the same wavelength as that coming from the alumina particles, it was impossible to eliminate through filtering and electronic shuttering. This soot-scattering would introduce unacceptably high-levels of noise into the measurement. As such, the PLMS images acquired at the upper imaging location were used only for flow-visualization and in finding RMS intermittency, which are less sensitive to the soot-scattering effect. Significant levels of soot-scattering were not observed in images acquired at the lower imaging-location.

Multiple normal- and low-gravity experiment runs were performed for each JFICF case. The images in each run were checked manually and sections with anomalous events (such as occasional seeder or camera read-out malfunctions) were removed from the image sequences. The remaining images from each 0.9 *s* experiment were broken down to form up to three sub-blocks per run. Each sub-block contained between 500 and 675 PLMS images, corresponding to 0.278 *s* to 0.375 *s*, or approximately $10(\tau_f)_{y/d=20}$. These sub-blocks were then processed in the manner outlined above in order to extract the exponent in the mixture-fraction decay scaling power-law and the centerline-trajectory (based on the locus of maximum mixture-fraction).

Figure 4.13 shows the measured mixture-fraction decay curves for the normal- and low-gravity r = 7, *Re* = 3350 case. The curve-to-curve offset arises from the aforementioned intensity normalization. The measured mixture-fraction decay curves were filtered with a 5-point running average prior to finding the best-fit power-law. The best-fit power-law curves for mixture fraction decay are shown overlaid on the measured traces in Figure 4.13. Tests showed that the 5-point smoothing affected the numerical value of the power-law exponent only in the third decimal place and thus is not considered a major source of error in the experiment. The measured traces displayed in Figure 4.13 were cropped at the downstream location where low signal-to-noise ratio made the data unreliable. One should not interpret the data traces as representing the length of the flame but rather just that portion it was possible to measure in this study. Figure 4.14 and Figure 4.15 likewise show the measured and best-fit power-law mixture fraction-decay profiles for the r = 10 and r = 11.5 cases respectively. These traces were similarly smoothed with five-point running averages and cropped to the cut-off point in the best-fit power-law profile.

In all cases, the mixture fraction decay curves appear to show a continuously varying profile prior to taking on the power-law decay profile characteristic of JFICF. The length of this continuously varying region appears to shrink with increasing momentum flux ratio, extending to approximately 0.3 *rd* in the $r = 7$ case and 0.1 *rd* in the $r = 11.5$ case. The reason for this continuously varying profile is not known but is thought to be related to aforementioned intensity normalization issue. After this initial region of continuously variation in the decay profile, the curves all assume a linear profile (in the logarithmic scale).

It can be seen in Figure 4.13(a) that while the decay curves reasonably approximate the *rd* power-law scaling, they show a noticeable variation about it. As this variation is not the same in every curve in that case it is believed that the variation is due to noise in the measurement. A close inspection of the decay curves reveals similar though less pronounced variation in all cases. The magnitude of these variations appears less and less pronounced with increasing momentum flux ratio. The decay curves appear more linear with increasing jet-exit Reynolds number, suggesting that the flow is sensitive to that parameter in this region.

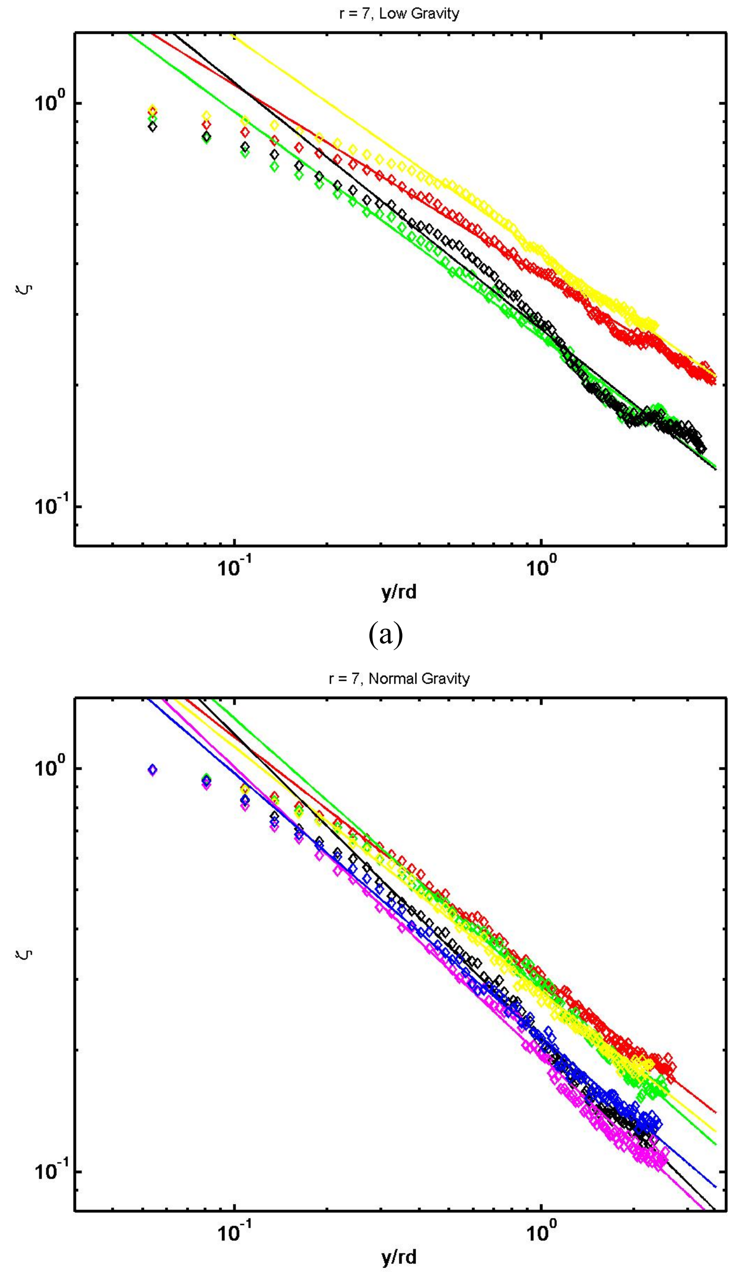

(a)

(b)

Figure 4.13 Mixture fraction decay curves for $r = 7$, $Re = 3350$ JFICF Case. Each trace represents the decay curve for a single sub-block of 500 - 675 images. Straight lines through each measured trace represent the best-fit power-law determined for a given sub-block. Data was smoothed with a five-point running average prior to plotting. (a) Low-gravity (b) Normal-Gravity.

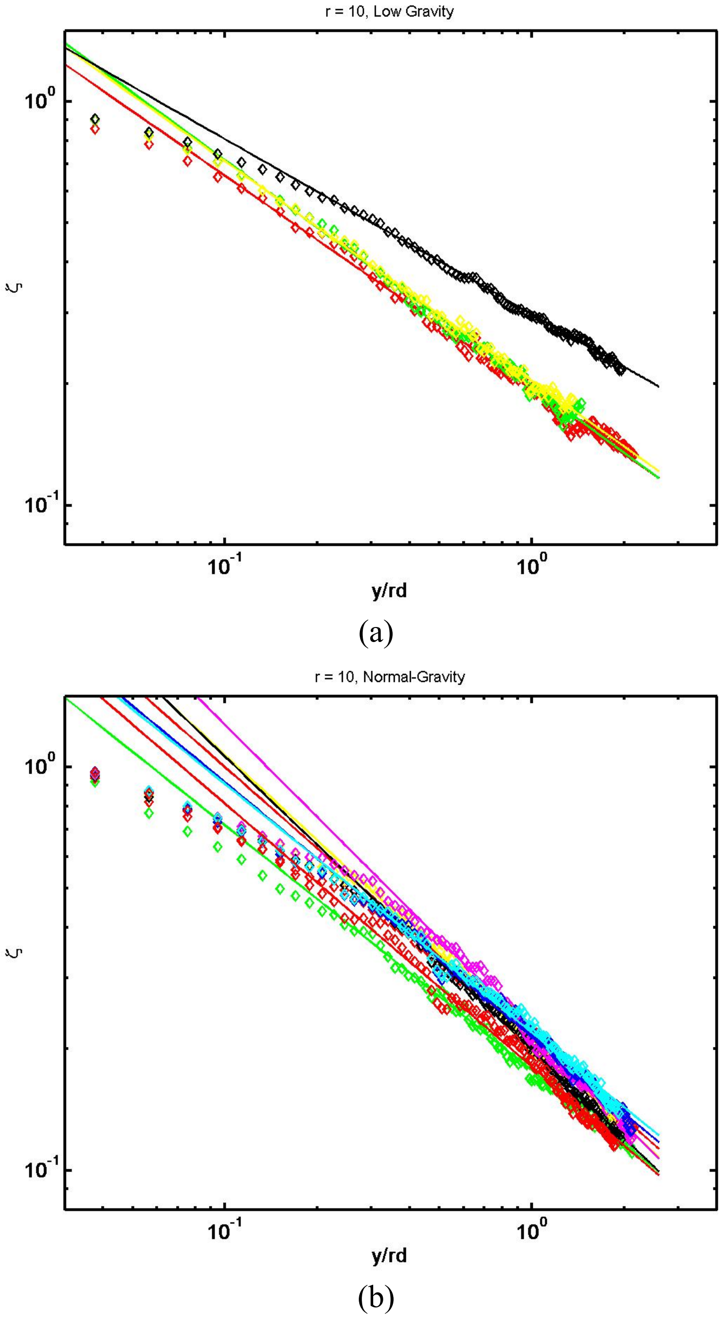

(a)

(b)

Figure 4.14 Mixture fraction decay curves for $r = 10$, $Re = 4800$ JFICF Case. Each trace represents the decay curve for a single sub-block of 500 - 675 images. Straight lines through each measured trace represent the best-fit power-law determined for a given sub-block. Data was smoothed with a five-point running average prior to plotting. (a) Low-gravity (b) Normal-Gravity.

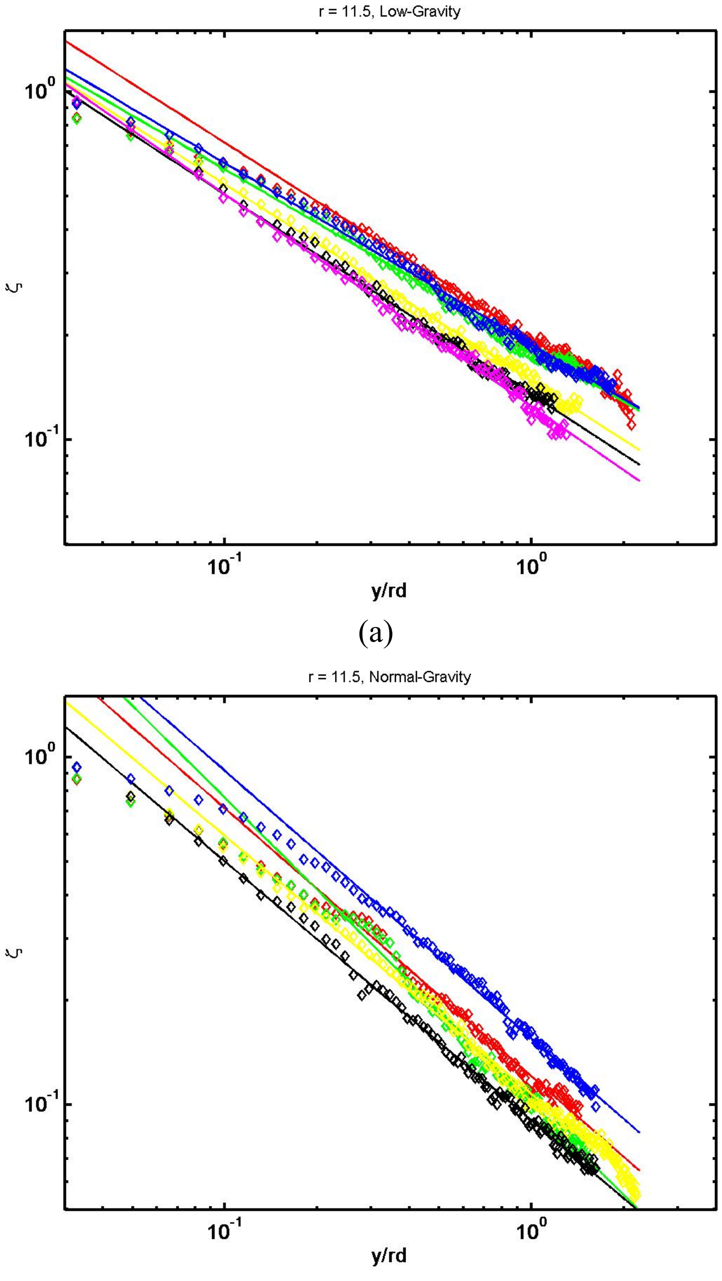

(a)

(b)

Figure 4.15 Mixture fraction decay curves for *r* = 11.5, *Re* = 5500 JFICF Case. Each trace represents the decay curve for a single sub-block of 500 - 675 images. Straight lines through each measured trace represent the best-fit power-law determined for a given sub-block. Data was smoothed with a five-point running average prior to plotting. (a) Low-gravity (b) Normal-Gravity.

r	n (1-g)	Uncertainty	n (low-g)	Uncertainty
7	- 0.67	0.09	- 0.54	0.09
10	- 0.67	0.05	- 0.52	0.09
11.5	- 0.78	0.07	- 0.56	0.04

Table 4.2 Best-fit mixture fraction power-law exponents

Table 4.2 lists the average power-law exponent *n* and 95% confidence level uncertainties for the best-fit curves plotted in each the figures above. The average *n* values listed in Table 4.2 are based on the *n* values determined for each individual sub-block of 500-675 images. Due to the relatively small number of curves used to determine the coefficient *n* for each case (4 – 8), the 95% confidence levels listed above assume a Student-t distribution.

Given the relatively large uncertainties associated with these measurements, the coefficients listed in Table 4.2 and the curves shown in the figures below reveal only subtle differences (if any) in the magnitudes of the normal- and low-gravity power-law exponent *n*. It appears in all cases, the low-gravity curves show a slightly less negative slope than their normal-gravity counterparts. However, as can be seen in Figure 4.16, these differences are of approximately the same magnitude as the uncertainty of the measurement. As such, a strong conclusion cannot be drawn about the seemingly different normal- and low-gravity values of *n*. Indeed, it is reasonable to conclude that given the small magnitude of the Becker and Yamazaki buoyancy parameter ($\xi_y < 1.4$ in normal-gravity, $\xi_y < 0.32$ in low-gravity) throughout the lower-imaging location, the lack of difference between normal and low-gravity *n* is representative of the physical reality. Put another way, in the lower imaging location, based on the magnitude of ξ_y, one would not expect to see major buoyancy-induced differences in the mixture fraction decay scaling and indeed, this appears to be the case.

The measured values of n show good agreement with those found in previous studies. The studies of Smith and Mungal (1998), Hasselbrink and Mungal (2001a) and Su and Mungal (2004) showed (experimentally and theoretically) that the mixture fraction decay scaling for the far-field (or "wake-like") region of the JICF follows a -2/3 power-law scaling. The data of Smith and Mungal (1998) (as reproduced in a figure from Hasselbrink and Mungal, 2001a) is shown in Figure 4.17. The data for this plot was acquired using planar laser-induced-fluorescence (PLIF) of acetone vapor seeded into a non-reacting, air-in-air JICF. In this plot, individual curves were collapsed into a single scaling by multiplying the measured scalar-concentration data by r. The data in this plot shows reasonably good agreement with a -2/3 power-law scaling, as do the data in the current study. It is instructive to note that the data shown in this plot shows significant variation in power-law behavior. In particular, the data for the $r = 10$ case (shown in the plot as squares) do not appear to follow the $rd^{-0.66}$ power law scaling at all. Given the scatter in these data it appears that a range of power law exponents could be fit to the experimental data.

The close agreement of the normal- and low-gravity values of n measured at the lower imaging location in this study suggests that buoyancy does not have a major influence upon the rate of mixture-fraction decay in this region. It appears that for $\xi_y < 1.5$ and $r = 7 – 11.5$, the entrainment characteristics of the JFICF can be considered momentum-dominated. As the measurement is limited by the imaging area, this value should not be taken as the upper limit of ξ_y where the entrainment characteristics are momentum-dominated. However it appears that below this value the entrainment characteristics of the JFICF can accurately be described as momentum-dominated.

The conclusion that the JFICF is momentum-dominated for $\xi_y < 1.5$ is consistent with previous studies performed on jet-flames in a crossflow and is also roughly consistent with studies of straight jet-flames. As mentioned in Chapter 3, Hasselbrink and Mungal (2001b) reported (what they concluded was) a buoyancy-induced bifurcation of the velocity decay profile of an $r = 10$, $\xi_y = 2.7$ methane JFICF ($Re = 6000$). They failed to detect a similar effect in an $r = 21$, $\xi_y = 1.8$ ($Re = 12{,}800$) methane JFICF. Although their study did not explicitly examine buoyancy effects in turbulent JFICF, the observation does appear to support the conclusion that buoyancy does not significantly affect the horizontal jet-flame issuing into a vertical crossflow for $\xi_y < 1.5$. The measurements made in the present study do have the subtle advantage of having directly compared flames with different ξ_y but the same Re and r.

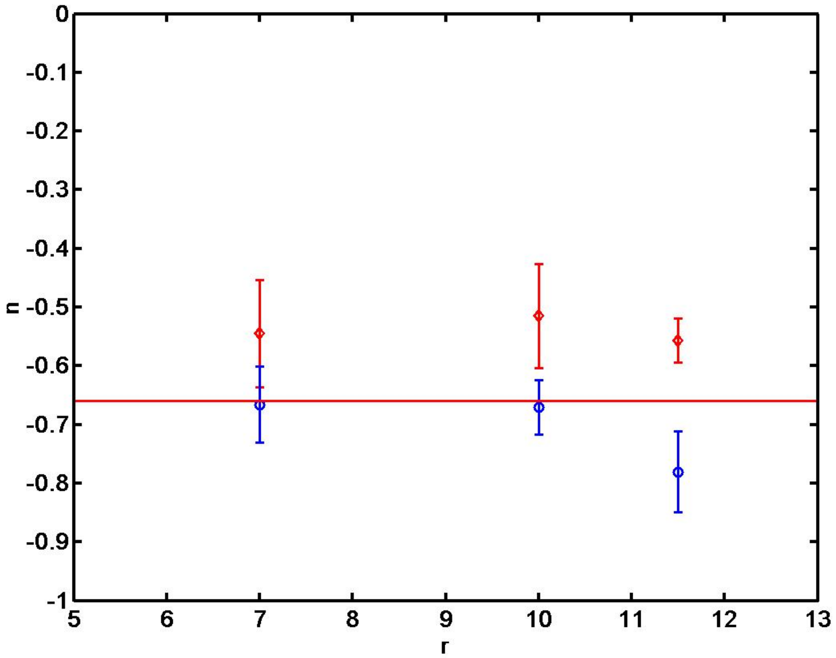

Figure 4.16 Best-fit power-law exponents for each case. Red diamonds correspond to low-gravity cases. Blue circles represent normal-gravity ones. The horizontal line corresponds to the *n* = -0.66 power-law exponent suggested by the scaling law of Hasselbrink and Mungal (2001a) and the experimental data of Smith and Mungal (1998) and Su and Mungal (2004).

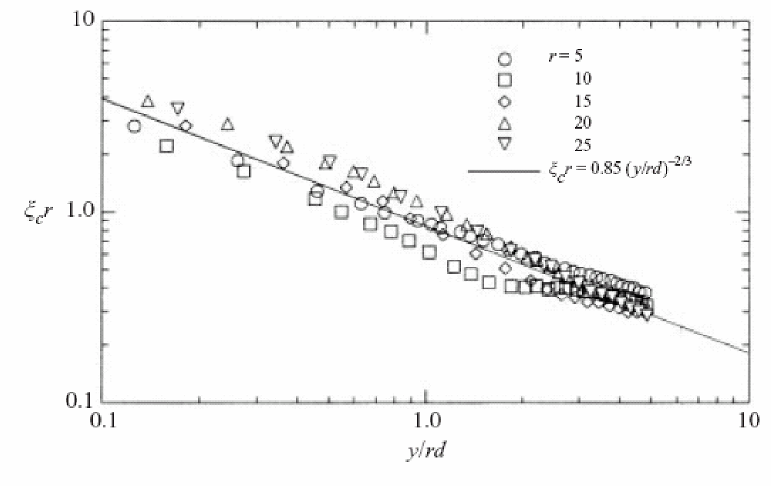

Figure 4.17 Previous Work: Scalar concentration decay curve for a non-reacting, air-in-air JICF of similar momentum flux ratio and jet-exit Reynolds number. The figure above is reproduced from Hasselbrink and Mungal (2001a) and is based on the acetone-PLIF measurements of Smith and Mungal (1998). The magnitude of the power-law exponent *n* measured in this study shows good agreement with that determined in previous studies.

Trajectories

Centerline-trajectories (based on the locus of maximum mixture fraction) were determined using the ensemble-average images in the lower imaging location. The trajectories are shown (normalized with *rd*) in Figure 4.18, plotted on both linear and logarithmic scales. The data shown in these plots were smoothed with a five-point running average. As was seen in the mixture-fraction decay scaling, this smoothing did not significantly affect the power-law coefficients shown in Table 4.3. Consistent with previous studies, the trajectory displayed power-law dependence on *rd*. The best-fit power-law curve for centerline trajectory is shown in each plot to illustrate how closely the trajectory follows the power-law scaling.

It is clear from these traces that at the high momentum flux ratios, the centerline trajectories of the normal- and low-gravity JFICF overlap almost exactly. In these cases buoyancy does not appear to significantly affect the trajectory. The lowest momentum-flux ratio ($r = 7$) case however does appear to show a small (up to ≈ 15%) difference in centerline trajectory penetration between normal and low-gravity, even at this low ξ_L value (≈ 1.4). The reason for this difference in penetration is not known. Given the relatively low jet-exit Reynolds number for the $r = 7$ case, it seems plausible that it could be a Reynolds number effect.

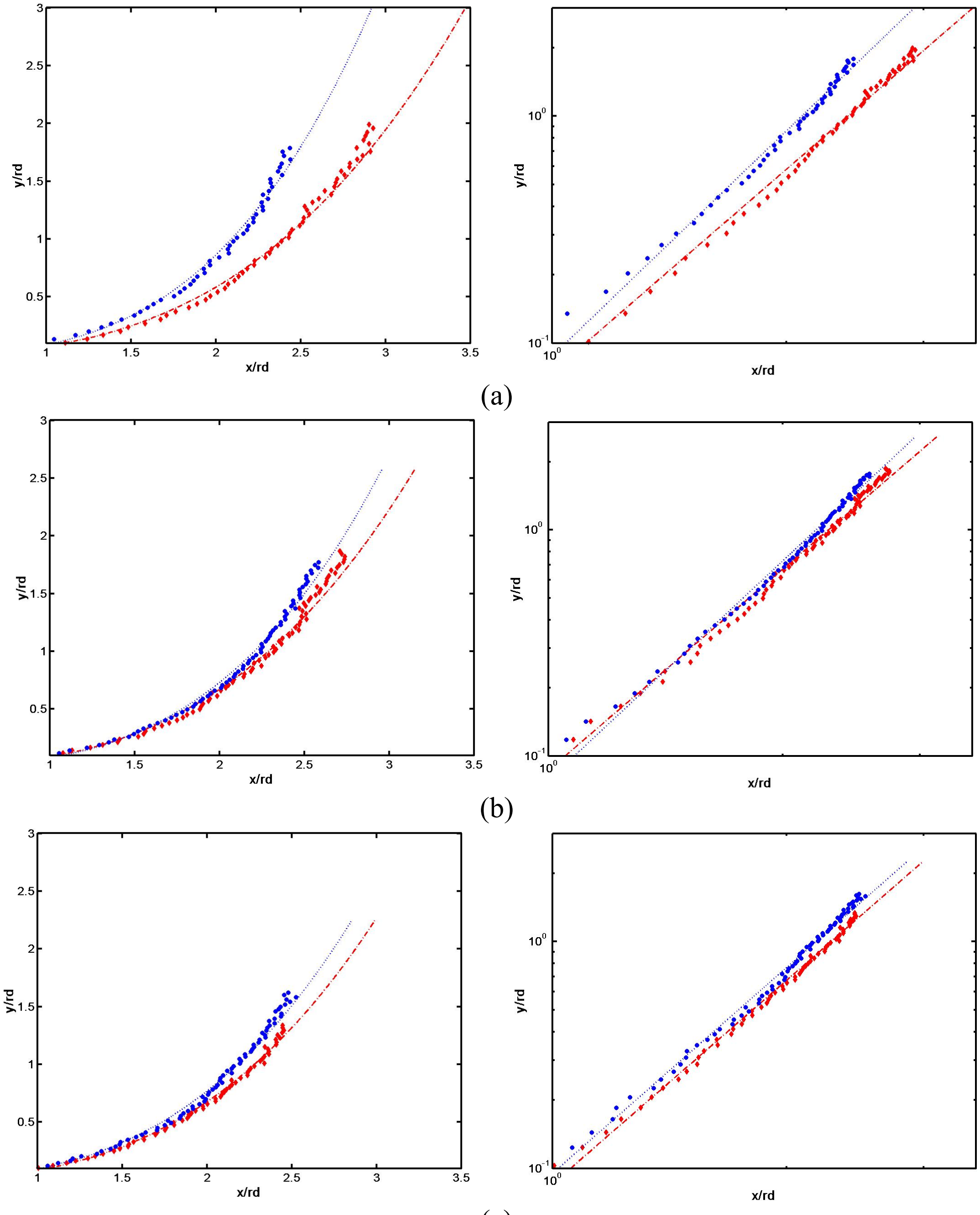

(a)

(b)

(c)

Figure 4.18 Centerline trajectories based on maximum mixture-fraction for normal- and low-gravity JFICF, overlaid with best-fit power-law trajectory (for near-exit region). The data is shown plotted in both linear and logarithmic scale in order to highlight both the similarity between normal- and low-gravity trajectories and how closely each approximates the *rd* power-law trajectory scaling. (Low-*g* = red, 1-*g* = blue) (a) $r = 7$ (b) $r = 10$ (c) $r = 11.5$

r	1 – *g*	Low-*g*
7	$(x/rd) = 2.09(y/rd)^{0.3}$	$(x/rd) = 2.39(y/rd)^{0.34}$
10	$(x/rd) = 2.21(y/rd)^{0.31}$	$(x/rd) = 2.29(y/rd)^{0.34}$
11.5	$(x/rd) = 2.25(y/rd)^{0.33}$	$(x/rd) = 2.18(y/rd)^{0.33}$

Table 4.3 Centerline Trajectories (based on maximum mixture fraction) of JFICF

It is noteworthy that while the trajectories do not appear to overlap exactly for this case (even in the near-exit region), the mixture-fraction decay power-law exponent *n* determined in the previous section does not appear to differ significantly between normal- and low-gravity. This observation may be interpreted in one of two ways. If the trajectories differ in near-exit region but maintain the same mixture fraction decay, one may conclude that buoyancy is acting to turn the jet towards the vertical while not significantly altering the entrainment characteristics. In this interpretation, momentum in the vertical direction is not conserved and the buoyant force is accelerating the jet upward without enhancing the entrainment. Another interpretation is that the mixture-fraction decay curve does in fact have a gravity-dependence at this location but the difference is within the uncertainty of the measurement and therefore not obvious. In any case, the trajectories of the normal- and low-gravity, *r* = 7 JFICF do appear to show a buoyancy-dependence whereas the higher-momentum jets do not.

Large-scale intermittency

The fluid intermittency in this system is defined as the probability that a given spatial location contains fluid originating from the jet. In this experiment it was easy to test for the presence of jet-fluid at a given location as it was seeded with alumina particles and the crossflow was not. RMS intermittency fields were computed for each JFICF case using the PLMS image sequences. The RMS intermittency field has proven a useful tool to characterize the large-scale turbulent fluctuations in straight turbulent jets and jet-flames (Van Cruyningen, 1990, Rehm, 1999, Idicheria, 2003). The RMS intermittency fields were computed as shown in Figure 4.19. First the raw, uncorrected PLMS images were smoothed with a Gaussian filter (kernel size 7 × 7, radius 4). The smoothed images were then converted to binary format by applying an intensity threshold equal to 2% of the maximum intensity level (1024 for the 10-bit images). The image thus generated marks the instantaneous spatial locations of the jet and crossflow fluids. The binary images were then used to compute the RMS intermittency field of the jet-fluid. As can be seen in Figure 4.19, this technique captures the instantaneous large-scale flow structure quite well.

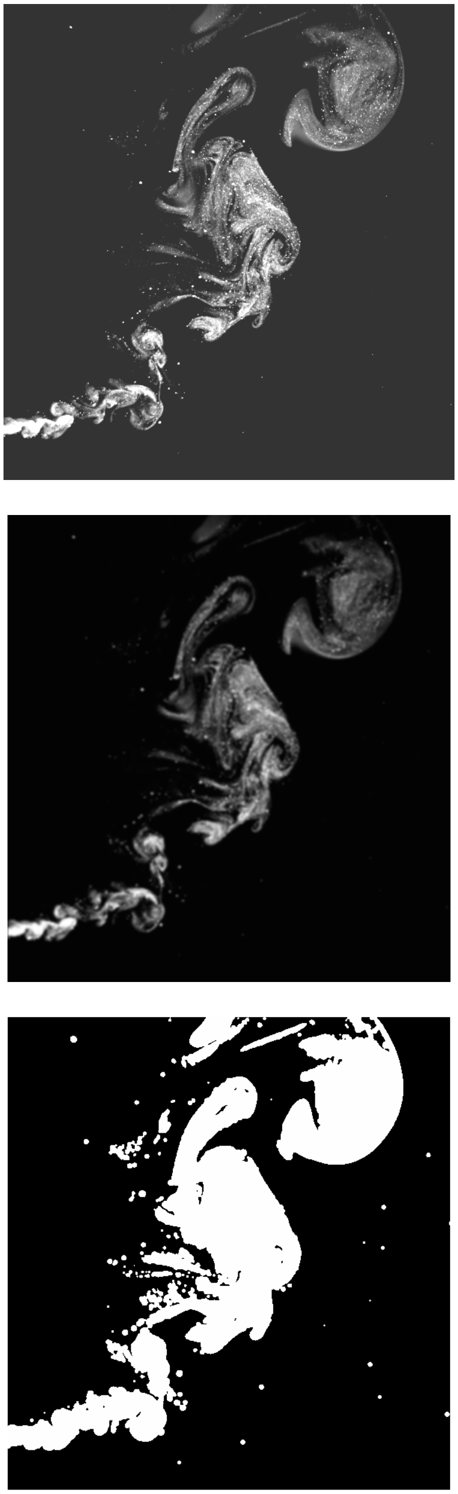

Figure 4.19 Method for computing fluid intermittency. (a) Raw PLMS (b) Smoothed PLMS image c) Binary image generated by thresholding the smoothed image

Figure 4.20 – Figure 4.22 show a series of sample RMS intermittency fields. Each image is overlaid in the middle with a dark band. This darkened region corresponds to the area in the overlapping fields of view where the intensity of the laser sheet dropped off such that the computed RMS intermittency fields became unreliable. The contour plots used slightly coarser resolution at the lower levels and finer resolution at the higher magnitudes. This was done to restrict the display of low-intensity RMS noise caused by the occasional drifting of extraneous particles through laser sheet in the test section but well away from the body of the jet. A few streaks of RMS intermittency noise (caused in this instance by several particles passing though the most intense region of the laser sheet) are observable toward the right-hand-side of the upper imaging location in Figure 4.20(a).

Several interesting features of the JFICF are apparent in the RMS intermittency fields displayed in Figure 4.20 – 4.22. As expected, in all cases the near-field of the JFICF is marked by a jet-like RMS intermittency field, wherein large-scale fluid intermittency is restricted to the edges of the jet. Unlike in a straight-jet though, it is apparent that as one moves downstream, the centerline RMS intermittency increases. In all but the lowest-momentum flux ratio ($r = 7$, $Re = 3350$) normal-gravity case, the JFICF show a dual-peak RMS intermittency field throughout the lower- and upper-imaging regions. In the low-momentum, normal-gravity case, the windward and leeward side peaks in RMS intermittency grow substantially and subsequently merge into a single-peaked profile whose maximum appears to lie on or close to the jet-centerline.

The difference in RMS intermittency appears consistent with the observations of flame-luminosity in Chapter 3. As noted in that chapter, the large-scale luminous flame structure for the $r = 7$ case displayed a noticeable tendency to stretch, elongate and oscillate from one side of the jet to the other in the far-field. It was concluded that this behavior was linked to the buoyancy-acceleration causing increased downstream convection velocities. Although flame-luminosity cannot be used as a direct proxy for the local fuel mixture fraction the single-peaked RMS intermittency profile appears consistent with the RMS luminosity field of the same case shown in Figure 3.13.

Beyond the low momentum-flux ratio case shown in Figure 4.20(b) with its single-peak RMS intermittency profile, the RMS intermittency fields do not appear to show clear variation with buoyancy over the region it was possible to image. There appears to be little discernable difference between the normal- and low-gravity RMS intermittency fields shown in Figure 4.21 and Figure 4.22. This is physically consistent with the flow-visualization images, wherein buoyancy was observed to have the largest impact upon the lower momentum JFICF but not as much on the higher momentum ones.

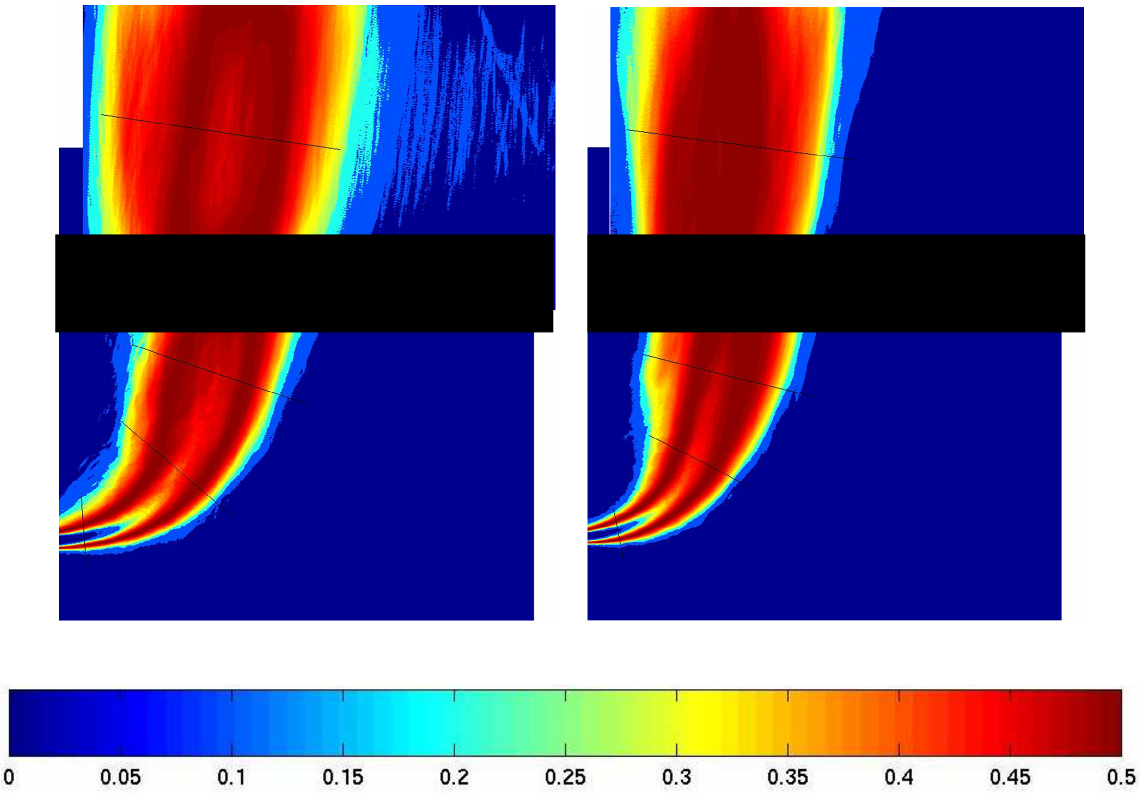

Figure 4.20 Sample RMS intermittency fields for $r = 7$, $Re = 3350$ JFICF (a) Low-Gravity and (b) Normal-gravity. The darkened band across the middle represents a region of the image corresponding to the tails of the laser sheets, where the reduced luminosity rendered the RMS unreliable.

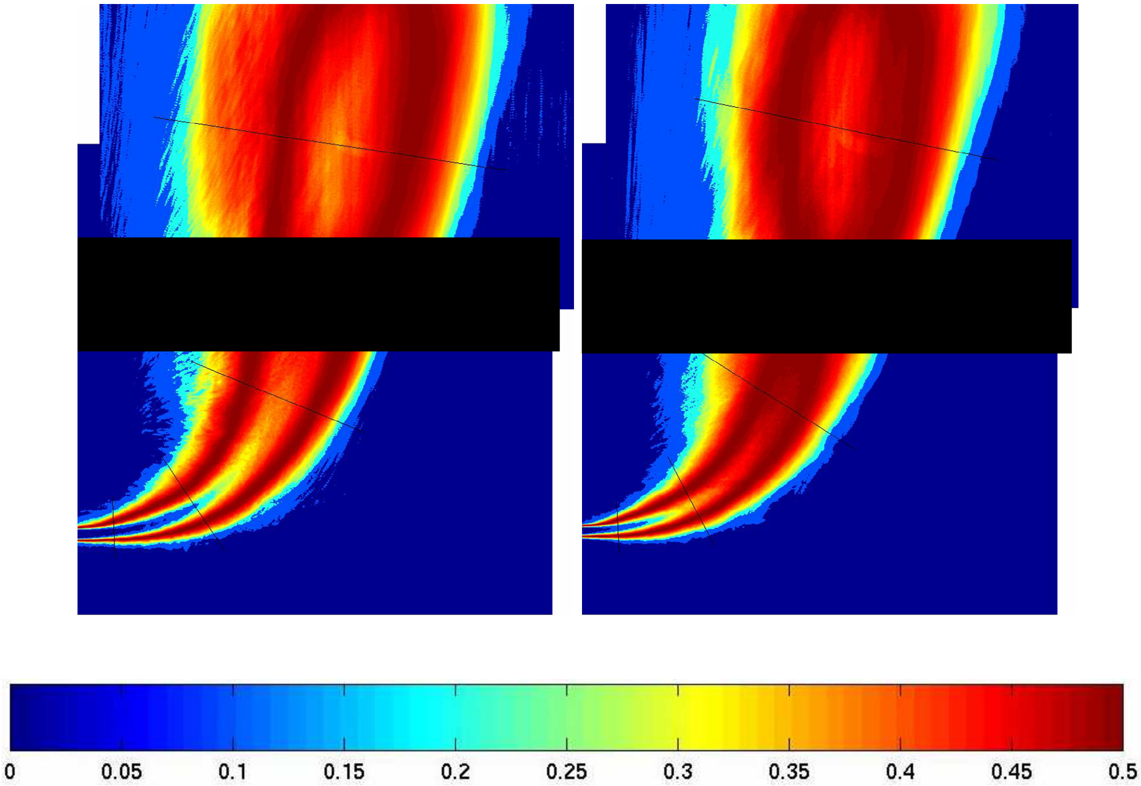

Figure 4.21 Sample RMS intermittency fields for r = 10, Re = 4800 JFICF (a) Low-Gravity and (b) Normal-gravity. The darkened band across the middle represents a region of the image corresponding to the tails of the laser sheets, where the reduced luminosity rendered the RMS unreliable.

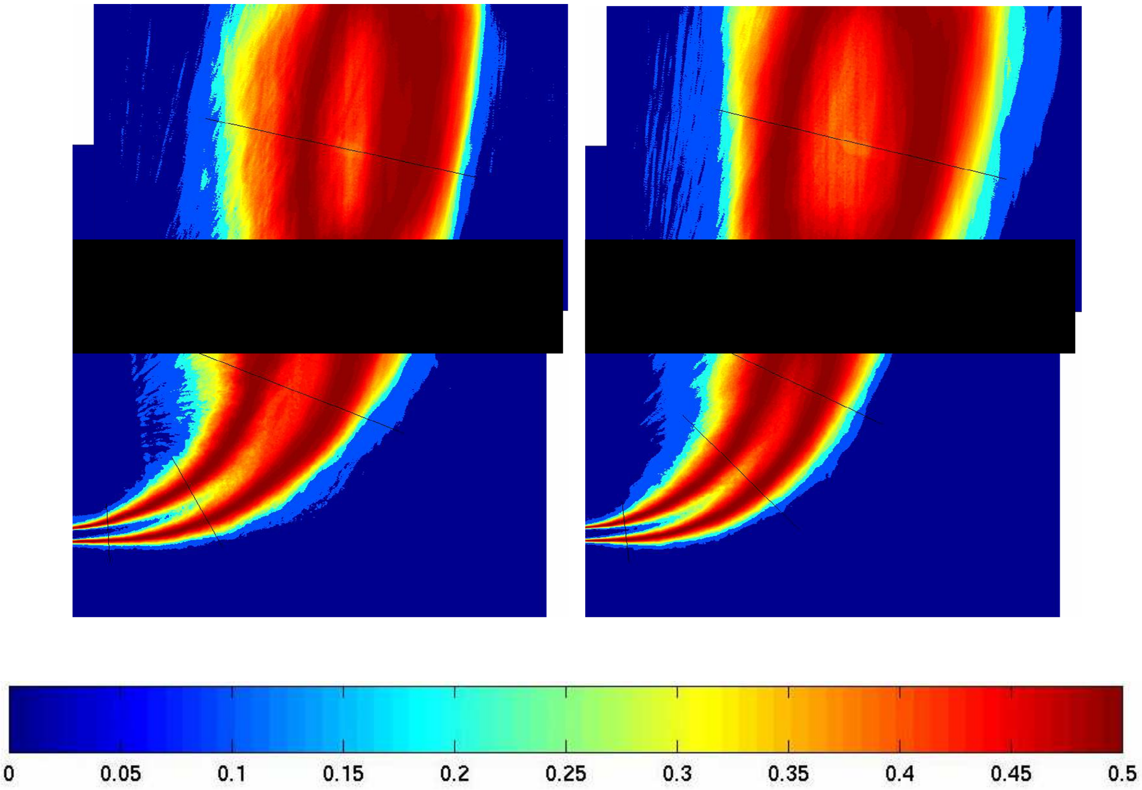

Figure 4.22 Sample RMS intermittency fields for r = 11.5, *Re* = 5500 JFICF (a) Low-Gravity and (b) Normal-gravity. The darkened band across the middle represents a region of the image corresponding to the tails of the laser sheets, where the reduced luminosity rendered the RMS unreliable.

Chapter 5: CONCLUSIONS

The aim of this study was to investigate the effect of buoyancy on turbulent JFICF and improve our fundamental understanding of this little-studied aspect of an important canonical flow. This goal was accomplished by comparing a series of hydrogen-diluted propane JFICF in normal-gravity with otherwise identical ones in low-gravity. Similarities and differences were examined using two different diagnostic techniques: high frame-rate digital cinematographic imaging and planar laser Mie scattering (PLMS). The advantage of this experimental technique is that it allows one to explicitly isolate and vary the buoyancy parameter ξ_L without the simultaneous alteration of other important flow-field parameters (such as momentum flux ratio r, jet-exit Reynolds number Re or jet-exit diameter d).

This study required extensive design and development of new experimental research facilities at the University of Texas at Austin and a new laser diagnostics system to instrument them. Chief among these new facilities was the University of Texas Drop Tower Facility. A multi-kHz frame-rate, fiber-optic coupled PIV/PLMS system was designed and developed for use in the drop-tower. This system constituted a major advance in the current state-of-the-art in microgravity combustion laser diagnostics systems. A new type of particle seeder was also developed for use in the low-gravity PLMS combustion experiments. This new seeder uses a counter-flow injection system to overcome the inherent column instability issue that prevents the use of fluidized bed particle seeders in low-gravity.

LUMINOSITY IMAGING EXPERIMENTS

High frame-rate digital imaging of flame-luminosity was used to study four turbulent, non-premixed (unpiloted) turbulent JFICF in normal- and low-gravity. The JFICF had momentum flux ratios ranging from 7 to 11.5 and jet-exit Reynolds numbers between 3350 and 5500. The jet-fluid was a composite fuel mixture containing 60 % hydrogen and 40 % propane (by volume). The JFICF used in this study had a top-hat velocity profile at the jet-exit and issued from an orifice mounted flush with the wall into a vertically cross-flowing stream of air. The value of ξ_L (based on the chord-length of the visible flame) for these flames ranged from 4.6 to 6.2 in normal-gravity and from 0.98 to 1.24 in low-gravity. By comparing normal- and low-gravity flames, it was possible to explicitly isolate and vary the level of buoyancy the JFICF felt relative to other flow-field parameters.

The flame-luminosity imaging revealed characteristics in the turbulent JFICF very similar to those seen in previous studies of straight nonpremixed turbulent jet-flames. In a manner reminiscent of that shown in Idicheria *et al.*, (2001, 2004) buoyancy was seen to disrupt the stability of the large-scale structure of the flame. In particular, the shear-layer vortex structures showed significant elongation and distortion in the vertical direction in the presence of buoyancy, a characteristic perhaps brought on by local strain caused by buoyant acceleration. The low-gravity flames were seen to maintain a much more uniform, coherent large-scale structure compared to their normal-gravity counterparts. The low-gravity flames also tended to maintain an instantaneous luminous flame-shape which kept approximately the same width throughout the far-field of the JFICF, whereas the normal-gravity flames tended to periodically thin down and elongate, causing a higher degree of non-uniformity in the instantaneous luminous flame width.

The buoyancy-induced elongation and distortion of the shear-layer vortices was seen to significantly alter the flametip burn-out and oscillation characteristics. Whereas flames in low-gravity tended to burn out uniformly across the width of the luminous flame zone, the normal-gravity flames tended to thin down and accelerate away from the luminous flame. The magnitude of flametip oscillations was seen to increase with ξ_L. Taken together, these observations suggest that buoyant acceleration of the large-scale shear-layer structures is fundamentally altering the nature of the flame-tip burnout.

Ensemble-average flame-luminosity images were used to compare mean flame-luminosity distribution, flame-lengths, flame-shapes and centerline trajectories of normal and low-gravity flames. The mean luminous flame-width was seen to increase with decreased buoyancy, a phenomenon commonly seen in straight jet-flames. This characteristic was attributed to the increased importance of molecular diffusion relative to the downstream convection in the absence of buoyant acceleration. Consistent with previous studies of turbulent non-premixed straight-jet flames (Idicheria *et al.*, 2004) the mean luminous flame-lengths showed little sensitivity to buoyancy.

The far-field jet-centerline trajectory (based on mean flame-luminosity) showed a measurable buoyancy-dependence. In all cases, the normal-gravity flames penetrated less deeply into the crossflow than their low-gravity counterparts. The differences in centerline-trajectory penetration appeared to scale with the difference in ξ_L (the Becker and Yamazaki buoyancy parameter). In all cases, the normal-gravity JFICF were seen to initially mimic the trajectory of the low-gravity JFICF but then at a certain point downstream turn upward to became "more vertical" and thus penetrate less deeply in crossflow with downstream distance than their low-gravity counterparts. The transition from one *rd* power-law scaling to another (in normal gravity) occurred at a downstream location corresponding to $\xi_C \approx 3$ (where subscript C refers to the flame chord-length). It was concluded that this point marks the end of the momentum-dominated forced convection limit in the JFICF and the beginning of a buoyancy-influenced flow regime.

PLMS IMAGING EXPERIMENTS

High frame-rate (1800 *fps*) planar laser Mie scattering was used to study three unpiloted turbulent, non-premixed JFICF. The flow parameters (*r, Re, d,* jet-fluid chemistry, etc.) for these flames were chosen such that they would replicate three of the four cases previously studied with high frame-rate luminosity-imaging. The ξ_y (based on downstream distance from the jet-exit and limited to sheet-illuminated imaging region) for these flames ranged from 3.1 to 4.3 in normal-gravity and 0.67 to 0.93 in low-gravity. The PLMS images were used both as fully time-resolved, planar flow-visualizations of the large-scale structure of the JFICF and also to determine the normal- and low-gravity values of the exponent *n* of the power-law scaling for mixture-fraction decay.

Consistent with previous studies of non-reacting JICF studies, the mixture-fraction of the JFICF showed a power-law decay profile that scaled as $(rd)^{-0.66}$. Consistent with the conclusion from Chapter 3 that the JFICF remains in the forced convection limit until $\xi_C > 3$, the power-law exponent showed little sensitivity to buoyancy for $\xi_C < 0.93$. It was not possible to determine the upper limit of this insensitivity to buoyancy however. Centerline trajectories based on the locus of maximum mixture fraction were also determined. It was seen that for $\xi_y < 1.5$ the centerline trajectory was highly insensitive to buoyancy, with normal- and low-gravity trajectories overlapping very closely. The low momentum-flux ratio flame ($r = 7$) was seen to turn toward the vertical noticeably sooner in normal-gravity ($\xi_y = 1.9$) than in low-gravity ($\xi_y = 0.4$) suggesting a transition from momentum-dominated trajectory-scaling to a buoyancy-influenced regime.

Comparisons of PLMS flow-visualization images revealed significant buoyancy-induced alteration of the large-scale shear-layer vortices in the flow. This alteration was most significant at the lower momentum flux ratio (r = 7) flames, where buoyancy was seen to induce significant elongation and distortion of the structures and lead to earlier break-down compared to their low-gravity counterparts. Consistent with Idicheria *et al.* (2004) who compared straight jet-flames in normal- and low-gravity, it was concluded that buoyancy acts to disrupt the hydrodynamic instability governing the large-scale shear-layer structures of the JFICF. The effect begins to become apparent at $\xi_y = 3.1$ and grows in influence to become a dominant flow-field characteristic approximately $\xi_y = 4.3$.

PLMS flow-visualization also yielded physical-insight into the nature of the fore-aft asymmetry of JFICF characteristics noted by previous researchers. It was observed that the windward-side shear-layer vortices tended to maintain smaller diameter and higher rates of rotation with downstream distance than those on the leeward side of the jet. The leeward-side vortices were seen expand far more rapidly with a corresponding decrease in seed-particle density.

CLOSING REMARKS

To summarize, this study developed a unique set of experimental tools and used them to thoroughly examine the large-scale flow-field characteristics of turbulent JFICF. Several buoyancy-related phenomena were identified and characterized, including the buoyancy-induced destabilization of large-scale shear-layer vortex structures, a buoyancy-induced alteration of jet centerline trajectory, flame-tip oscillation and burnout characteristics. Taken as a whole, these measurements lead to the conclusion that buoyancy acts to reduce the large-scale organization and coherence of the flow-field of turbulent JFICF, even at the relatively modest length-scales of these laboratory-scale flames.

This study also yielded significant physical insight into the previously observed fore-aft asymmetry of flow-field characteristics in turbulent JFICF. Observations relating to flame-luminosity and shear-layer vortex expansion in the JFICF support previous conclusions that mixing in the JFICF show a leeward-side bias. This leeward-side bias was seen to affect the mean and RMS luminosity distributions as well as the size, density and angular velocity of the shear-layer vortices in the JFICF.

FUTURE WORK

The present study revealed interesting trends and phenomena in the mean and instantaneous flow structure of the turbulent, nonpremixed JFICF. This study however is neither exhaustive nor definitive. Our understanding of the effects of buoyancy on JFICF would benefit from further research.

One of the major limitations of the present study is the range of jet-exit Reynolds numbers, momentum flux ratios and jet-exit diameters one could study in the highly compact flow-facility and drop-rig. The compact size of the rig also placed significant limitations upon placement of experimental equipment including the camera, the sheet-forming optics, the pressurized gas system and battery packs. Another limitation resulted from the short (≈ 1 *s*) run times possible in the UT-DTF, which made obtaining uniform particle seeding in low-gravity even more difficult. Conducting future experiments in a larger flow-facility flown aboard a parabolic trajectory aircraft would overcome the majority of these limitations. The larger flow-facility would increase the range of jet-exit diameter, momentum flux ratio and jet-exit Reynolds numbers one could study. The longer duration periods of low-gravity would help generate more uniform particle seeding. The larger available work-area afforded by a parabolic trajectory aircraft would also allow for more optimal placement of the camera, optics and other equipment.

This field of research would also benefit from the application of PIV to make quantitative measurement of velocity, vorticity, strain, dilatation and entrainment characteristics of normal and low-gravity JFICF. Such measurements would be particularly useful in determining the physical mechanism responsible for the observed elongation and distortion of the large-scale shear-layer vortices. They would also provide a measure of jet-centerline trajectory more easily compared to that of previous studies. It is possible to make such measurements using the fiber-optic based diagnostics system now available in the UT-DTF.

One particularly interesting extension of the present work would be to study the effect of increasing jet-exit Reynolds number in a turbulent JFICF while holding *rd* constant. This could be accomplished using the drop-rig in its present configuration simply by varying the jet-exit diameter and the jet-exit velocity. The advantage of performing such a study in low-gravity is the ability to generate momentum-dominated JFICF over a wide range of jet-exit Reynolds numbers.

Appendix A: CONTROL-VOLUME ANALYSIS FOR A HORIZONTAL, TURBULENT JET FLAME ISSUING INTO A VERTICAL CROSSFLOWING AIR-STREAM

As was mentioned in Chapter 1 there does not appear to be a single, universal scaling parameter with which to compare the relative importance of buoyancy in turbulent JFICF. A (highly simplified) control-volume analysis was conducted with the goal of determining the appropriate non-dimensional parameter with which to quantify buoyancy effects in JFICF. This analysis is presented below.

Figure A.1 shows a simplified diagram of the JFICF system examined in this study. The jet issues horizontally from a circular nozzle (of diameter *d*) mounted flush with the wall of the flow-facility. The jet is assumed to have a uniform velocity profile across its entire area. The vertical crossflow is similarly assumed to be of uniform velocity across its width. The outline of the control volume is shown by the red dashed line.

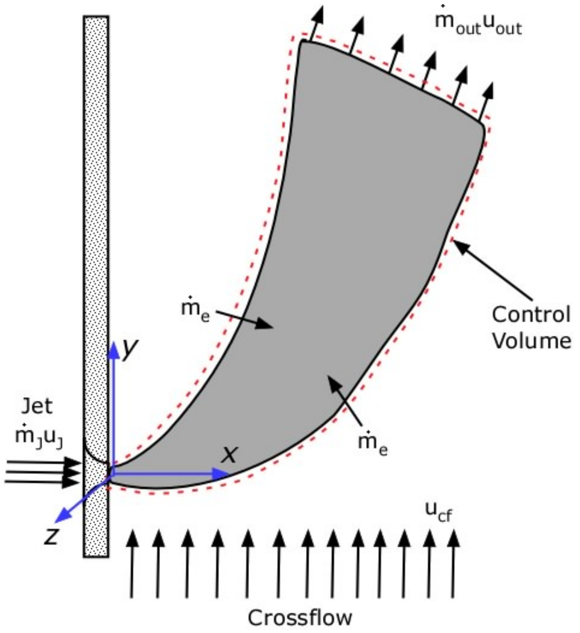

Figure A.1 Schematic diagram of the control volume used in this analysis.

Applying the mass balance relations to this control volume gives us

$$\sum \dot{m} = 0 \tag{A.1}$$

$$0 = \dot{m}_j + \dot{m}_e - \dot{m}_{out} \tag{A.2}$$

which gives,

$$\dot{m}_e = \dot{m}_{out} - \dot{m}_j \tag{A.3}$$

where $\dot{m}_j$ refers to the mass flowrate of the jet at the exit, $\dot{m}_e$ refers to mass of crossflow fluid entrained by the jet and $\dot{m}_{out}$ to the mass flowing out of the upper surface of the control volume (i.e. the one cutting perpendicularly across the jet). It is assumed the mass exits the control volume across the surface with a uniform velocity profile, u_{out}.

We will assume negligible forces in the x-direction. We then apply the momentum balance equation in the x-direction and get

$$\sum F_x = \sum M_x \tag{A.4}$$

$$0 = \dot{m}_j u_j - \dot{m}_{out} u_x \tag{A.5}$$

$$\dot{m}_{out} = \frac{\dot{m}_j u_j}{u_x} \tag{A.6}$$

where u_x denotes the x-component of velocity at the outflow surface of the control volume and M_x is the x-direction momentum-flux through the control volume.

Applying the momentum balance in the y-direction (corresponding to the vertical direction, the initial crossflow direction) to the control volume gives us

$$\sum F_y = \sum M_y \tag{A.7}$$

or

$$F_B = \dot{m}_{out} u_y - \dot{m}_e u_{cf} \tag{A.8}$$

where M_y and F_y represent the y-direction momentum flux and force in the y-direction respectively. F_B denotes the buoyant force acting on the fluid inside the control volume. u_y denotes the y-component of velocity at the outflow surface of the control volume. Using Equation A.3, we replace $\dot{m}_e$ as follows

$$F_B = \dot{m}_{out} u_y - \left(\dot{m}_{out} - \dot{m}_j\right) u_{cf} \tag{A.9}$$

$$= \dot{m}_{out}\left(u_y - u_{cf}\right) + \dot{m}_j u_{cf} \tag{A.10}$$

Rearranging the equation above gives

$$\dot{m}_{out}\left(u_y - u_{cf}\right) = F_B - \dot{m}_j u_{cf} \tag{A.11}$$

We can then use Equation A.6 to show that this becomes

$$\frac{\dot{m}_j u_j}{u_x}\left(u_y - u_{cf}\right) = F_B - \dot{m}_j u_{cf} \tag{A.12}$$

which simplifies to

$$\frac{\left(u_y - u_{cf}\right)}{u_x} = \frac{F_B}{\dot{m}_j u_j} - \frac{u_{cf}}{u_j} \tag{A.13}$$

Note that the left hand side of this equation is related to the slope of the jet trajectory with downstream distance. At this point however, we do not know the form of u_x, u_y or F_B.

In order to estimate the effect of buoyancy on the turbulent JFICF, let us model the jet as being conical in shape. We'll assume a base diameter equal to the local jet-width δ (at the location of the outflow surface of the control volume) and the height equal to the curvilinear distance (S) from there to the jet exit, i.e., that its volume may be described by

$$V = \left(\frac{\pi\ \delta^2}{4}\right)\frac{S}{3} \tag{A.14}$$

Furthermore, let us assume the jet-fluid is of a uniform density throughout. With these assumptions, the buoyancy force term in the trajectory-slope equation may be described as

$$\frac{F_B}{\dot{m}_j u_j} = \frac{g\left(\rho_{cf} - \bar{\rho}_j\right)V}{\dot{m}_j u_j} \tag{A.15}$$

$$\approx \frac{g\left(\rho_{cf} - \bar{\rho}_j\right)\left(\dfrac{\pi\,\delta^2}{4}\right)\dfrac{S}{3}}{\left(\rho_j u_j\left(\dfrac{\pi\,d^2}{4}\right)\right)u_j} \tag{A.16}$$

where ρ_j denotes the fluid density at the jet-exit and ρ_{cf} the crossflow density. $\bar{\rho}_j$ denotes a characteristic global fluid density for jet. The equation above simplifies to

$$\frac{F_B}{\dot{m}_j u_j} \approx \frac{g\left(\rho_{cf} - \bar{\rho}_j\right)\,\delta^2\,\dfrac{S}{3}}{\left(\rho_j d^2\right)u_j^2} \tag{A.17}$$

$$\approx \frac{g}{3}\left(\frac{\rho_{cf} - \bar{\rho}_j}{\rho_j}\right)\left(\frac{\delta^2 S}{d^2}\right)\frac{1}{u_j^2} \tag{A.18}$$

If we further assume the characteristic global density $\bar{\rho}_j$ is small compared to the crossflow density and that δ varies as a linear function of S, the relation above simplifies as follows,

$$\frac{F_B}{\dot{m}_j u_j} \approx \frac{g\left(\rho_{cf} - \bar{\rho}_j\right)\,\delta^2\,\dfrac{S}{3}}{\left(\rho_j d^2\right)u_j^2} \tag{A.19}$$

$$\approx \frac{g}{3}\left(\frac{\rho_{cf}}{\rho_j}\right)\left(\frac{1}{d^2}\right)\frac{\alpha^2 S^2 S}{u_j^2} \tag{A.20}$$

$$\approx \frac{g\alpha^2}{3}\left(\frac{\rho_{cf}}{\rho_j}\right)\left(\frac{1}{d^2}\right)\frac{S^3}{u_j^2} \tag{A.21}$$

where α represents a multiplicative constant relating δ and S. Noting that $D_s = d\,(\rho_j / \rho_{cf})^{1/2}$, and thus that $(1/D_s^2) = (1/d^2)(\rho_{cf}/\rho_j)$, the relation above simplifies to

$$\frac{F_B}{\dot{m}_j u_j} \approx \frac{g\alpha^2}{3}\left(\frac{1}{D_s^2}\right)\frac{S^3}{u_j^2} \tag{A.22}$$

and finally, by multiplying the top and bottom by D_s^3 and rearranging terms, we get

$$\frac{F_B}{\dot{m}_j u_j} \approx \frac{\alpha^2}{3}\left(\frac{g\,D_s}{u_j^2}\right)\left(\frac{S^3}{D_s^3}\right) \tag{A.23}$$

which in turn simplifies to

$$\frac{F_B}{\dot{m}_j u_j} \approx \frac{\alpha^2}{3}\xi_S^3 \tag{A.24}$$

where ξ_s is the Becker and Yamazaki (1978) buoyancy parameter based on centerline distance from the jet-exit. Thus Equation A.13 becomes

$$\frac{\left(u_y - u_{cf}\right)}{u_x} \approx \frac{\alpha^2}{3}\xi_S^3 - \frac{u_{cf}}{u_j} \tag{A.25}$$

Although based on a highly idealized and simplified model, the equation above shows that the relative importance of buoyancy in a turbulent JFICF of the configuration used in this study is dependent on the Becker and Yamazaki (1978) buoyancy parameter. The equation above provides a basis for systematic comparison between buoyant and non-buoyant horizontal, turbulent jet-flames issuing into vertical crossflowing airstreams.

References

Andreopoulos, J. 1985. “On the structure of jets in a crossflow”, J. Fluid Mechanics. **157:** 163-197.

Bahadori, M.Y., Stocker, D.P., Vaughan, D.F., Zhou, L. and Edelman, R.B. 1993. “Effects of Buoyancy on Laminar, Transitional and Turbulent Gas Jet Diffusion Flames” Modern Developments in Energy, Combustion and Spectroscopy, Pergamon Press, 49-66.

Bandaru, R.V., Turns, S.R. 2000. “Turbulent jet flames in a crossflow: Effects of some jet, crossflow, and pilot-flame parameters on emissions”, Combustion and Flame, **121:**137-151.

Becker, H.A., Yamazaki, S. 1978. “Entrainment, momentum flux and temperature in vertical free turbulent diffusion flames”, Combustion and Flame, **33:**123-149.

Becker, H.A., Liang, D., Downey, C.I. 1981. “Effect of burner orientation and ambient airflow on geometry of turbulent free diffusion flames”, Eighteenth Symposium (International) on Combustion, 1061-1071.

Birch, A.D., Brown, D.R., Fairweather, M, Hargrave, G.K. 1989. “An experimental study of a turbulent natural gas jet in a cross-flow”, Combustion Sci. and Tech.. **66:**217-232.

Bosanquet, C.H., Pearson, J.L. 1936. “The spread of smoke and gases from chimneys”. Transactions of the Faraday Society, **32(**1).

Botros, P.E., Brzustowski, T.A. 1979. “An experimental and theoretical study of the turbulent diffusion flame in cross-flow”, Seventeenth Intl. Symposium on Combustion. The Combustion Institute.

Boxx, I.G., Idicheria, C.A., Clemens, N.T. 2003. “An exploratory study of the effects of buoyancy on turbulent nonpremixed jet flames in crossflow”, AIAA-2003-1151.

Boxx, I.G., Idicheria, C.A., Clemens, N.T. 2004. “Kilohertz PIV/PLMS of low-gravity turbulent flames in a drop tower”. 12th International Symposium on Application of Laser Techniques to Fluid Mechanics. Lisbon, Portugal

Broadwell, J.E., Breidenthal, R.E. 1983. “Structure and mixing of a transverse jet in incompressible crossflow”, J. Fluid Mechanics, **148:**405-412.

Brown, G.L., Roshko, A. 1974. “On density effects and large structure in turbulent mixing layers”. J. Fluid Mechanics. **64:**775 – 816.

Brzustowski, T.A. 1976. “Flaring in the energy industry”, Progress in Energy Combustion Science, **2:**129-141.

Brzustowski, T.A. 1977. “Hydrocarbon turbulent diffusion flame in subsonic cross flow”, AIAA 77-22. AIAA 15th Aerospace Sciences Meeting.

Brzustowski, T.A., Gollahalli, S.R., Sullivan, H.F. 1975. “The turbulent hydrogen diffusion flame in a cross-wind”, Combustion Science and Technology, **11:**29-33.

Chigier, N.A., Strokin, V. 1974. “Mixing processes in a free turbulent diffusion flame”, Combustion Sci. and Tech. **9:**111-118.

Choudhuri, A.R., Gollahalli, S.R. 2000. “Effects of ambient pressure and burner scaling on the flame geometry and structure of hydrogen jet flames in cross-flow”. International Journal of Hydrogen Energy, **25:**1107-1118.

Choudhuri, A.R., Gollahalli, S.R. 2003. “Characteristics of hydrogen-hydrocarbon composite fuel turbulent jet flames”. International Journal of Hydrogen Energy, **28:**445-454.

Cimbala, J.M., Nagib, H.M., Roshko, A. 1988. “Large structure in the far wakes of two-dimensional bluff bodies”. J. Fluid Mechanics. **190:**265-298.

Clemens, N.T., Paul, P.H. 1995. “Effects of heat release on the near field flow structure of hydrogen jet diffusion flames”, Combustion and Flame, **102:**271-284.

Coelho, S.L.V., Hunt, J.C.R. 1989. “The dynamics of the near field of strong jets in crossflows”, J. Fluid Mechanics, **200:**95-120.

Dahm, W.J.A., Dimotakis, P.E. 1985. “Measurements of entrainment and Mixing turbulent jets”, AIAA Journal, **25(**9):1216-1223.

Ebrahimi, I., Kleine, R. 1976. “The nozzle fluid concentration fluctuation field in round turbulent free jets and jet diffusion flames”. Sixteen Symposium (International) on Combustion, The Combustion Institute, Pittsburgh, 1711-1723.

Ellzey, J.L., Oran, E.S. 1995. “Effects of heat release and gravity on an unsteady diffusion flame”, Twenty-Third Symposium (International) on Combustion. The Combustion Institute. 1635-1640.

Fairweather, M., Jones, W.P., Lindstedt, R.P., Marquis, A.J. 1991. “Predictions of a turbulent reacting jet in a cross-flow”, Combustion and Flame. **84:**361-375.

Fric, T.F., Roshko, A. 1994. “Vortical structure in the wake of a transverse jet”, J. Fluid Mechanics, **279**, 1-47.

Goh, S.F., Gollahalli, S.R. 2002, "Pilot flame effects on gas jet flames in crossflow", J. Propulsion and Power. **18**(5):1068-1075.

Greenberg, P.S, Wernet, M.P., Yanis, W., Urban, D.L., Sunderland, P.B. 2003. “Development of PIV for microgravity diffusion flames”. Seventh International Workshop on Microgravity Combustion and Chemically Reacting Systems. NASA/CP-2003-212376.

Hama, F.R., 1962. “Streaklines in a perturbed shear flow”, Physics of Fluids. **5(**6):644-650.

Han, D., Mungal, M.G. 2001. “Direct measurement of entrainment in reacting/ nonreacting turbulent jets”. Combustion and Flame. **124:**370-386.

Hasselbrink, C.F. 1999. “Transverse jets and jet flames: Structure, scaling, and effects of heat release”, Technical Report TSD-121. Thermosciences Division - Department of Mechanical Engineering, Stanford University.

Hasselbrink, E.F., Mungal, M.G. 2001a. “Transverse jets and jet flames. Part 1. Scaling laws for strong transverse jets”, J. Fluid Mech. **443:**1-25.

Hasselbrink, E.F., Mungal, M.G. 2001b. “Transverse jets and jet flames. Part 2. Velocity and OH field imaging”. J. Fluid Mech. **443:**27-68.

Haynes, B.S., Wagner, H.G. 1981. “Soot formation”, Progress in Energy Combustion and Science. **7:**229-273.

Hegde, U., Zhou, L, Bahadori, M.Y. 1994. “The transition to turbulence of microgravity gas jet diffusion flames”. Combustion Science and Technology. **102:**95-113.

Hegde, U., Yuan, Z.G., Stocker, D.P., Bahadori, M.Y. 1999. “Characteristics of non-premixed turbulent flames in microgravity”. Proceedings of the Fifth International Microgravity Combustion Workshop.

Hermanson, J.C., Johari, H., Stocker, D.P., Hegde, U.G. 2004. “Buoyancy effects in strongly pulsed turbulent diffusion flames”. Combustion and Flame, **139:**61-76.

Huang, R.F., Chang, J.M. 1994. “The stability and visualized flame and flow structures of a combusting jet in cross flow”, Combustion and Flame, **98:** 267-278.

Ibrahim, S.M.A., El-Mahallawy, F.M. 1985. “The structure of turbulent free diffusion flames”, Combustion and Flame, **60:**141-155.

Idicheria, C.A., Boxx, I.G., Clemens, N.T. 2001. “Large-scale flow structure in turbulent nonpremixed flames under normal- and low-gravity conditions”, AIAA Paper 2001-0628.

Idicheria, C.A.. 2003. “Investigation of buoyancy effects on turbulent nonpremixed jet flames by using normal and low-gravity conditions”, Ph.D. Dissertation. The University of Texas at Austin.

Idicheria, C.A., Boxx, I.G., Clemens, N.T. 2004. “Characteristics of turbulent nonpremixed jet flames under normal- and low-gravity conditions”. Combustion and Flame, **138:**384-400.

Kadota, T., Wang, J.X., Kawaoka, T. 1990. “Structure of propane jet diffusion flame in a cross flow”, JSME International Journal. **33**(3):575-581.

Kalghatgi, G.T. 1983. “The visible size and shape of a turbulent hydrocarbon jet diffusion flame in a cross-wind”. Combustion and Flame. **52:**91-106.

Kamotani, T., Greber, I. 1972. “Experiments on a turbulent jet in a cross flow”, AIAA Journal, **10**(11):1425-1429.

Karagozian, A.R. 1986. "An analytical model for the vorticity associated with a transverse jet", AIAA Journal. **24**(3):429-436.

Karagozian, A.R., Nguyen, T.T. 1986. “Effects of heat release and flame distortion in the transverse fuel jet”, Twenty-first Symposium (Intl) on Combustion. The Combustion Institute. 1271-1279.

Katta, V.R., Roquemore, W.M. 1993. “Role of inner and outer structures in transitional jet flame”. Combustion and Flame. **92:**274-282.

Keffer, J.F., Baines, W.D. 1963. “The round turbulent jet in a cross-wind”, J. Fluid Mechanics, **15**(4): 481-496.

Kelso, R. M., Lim, T.T., Perry, A.E. 1996. "An experimental study of round jets in cross-flow", J. Fluid Mechanics. **306:**111-144.

Kelso, R. M., Smits, A.J. 1995. "Horseshoe vortex systems resulting from the interaction between a laminar boundary layer and a transverse jet", Phys. Fluids. **7** (1):1995.

Kennedy, I.M., Kent, J.H. 1979. “Measurements of a conserved scalar in turbulent jet diffusion flames” Seventeeth Symposium (International) on Combustion, The Combustion Institute, Pittsburgh, 279-286.

Kuo, K.K. 1986. “Principles of Combustion”. John Wiley & Sons Inc. New York, USA.

Lee, J.H.W., Chu, V.H. 2003. “Turbulent jets and plumes, A Lagrangian approach”. Kluwer Academic Publishers. Norwell, Ma. USA.

LeGrives, E. 1978. "Mixing process induced by the vorticity associated with the penetration of a jet into a cross flow", J. Engineering for Power. **100:** 465-475.

Lim, T. T., New, T. H., Luo, S. C. 2001. "On the development of large-scale structures of a jet normal to a cross flow", Phys. Fluids. **12**(3):770 - 775.

Long, M.B., Starner, S.H., Bilger, R.W. 1993. “Differential diffusion in jets using joint PLIF and Lorenz-Mie imaging”, Combustion Science and Tech. **92:**209 – 224.

Lysaght, A.J.R., Bilger, R.W., Kent, J.H. 1982. “Visualization of mixing in turbulent diffusion flames”. Combustion and Flame, **46:**105-108.

Margason, R.J. 1968. “The path of a jet directed at large angles to a subsonic free stream”, NASA TN D-4919.

Margason, R.J. 1993. “Fifty years of jet in crossflow research”, AGARD Conference Proceedings 534.

Melling, A. 1997. “Tracer particles and seeding for particle image velocimetry”, Measurement Science and Technology, **8:**1406-1416.

McMahon, H.M., Hester, D.D., Palfery, J.G. 1971. “Vortex shedding from a turbulent jet in a cross-wind”, J. Fluid Mechanics. **48:**73-80.

Moussa, Z.M., Trishka, J.W., Eskinazi, S. 1977. “The near field in the mixing of a round jet with a cross-stream”, J. Fluid Mechanics, **80:**49-80.

Mungal, M.G., Karasso, P.S., Lozano, A. 1991. "The visible structure of turbulent jet diffusion flames: Large-scale organization and flame tip oscillation", Comb. Sci and Tech. **76:**165-185.

Mungal, M.G., O’Neil, J.M. 1989. “Visual observations of a turbulent diffusion flame”, Combustion and Flame. **78:**377-389.

Muniz, L., Mungal, M.G. 2001. “Effects of heat release and buoyancy on flow structure and entrainment in turbulent nonpremixed flames”, Combustion and Flame. **126:**1402-1420.

Pratte, B.D., Baines, D. 1967. “Profiles of the round turbulent jet in a cross flow”, Journal of the Hydraulics Division, Proceedings of the American Society of Civil Engineers. **HY 6:**53-64.

Rehm, J. 1999. "The effects of heat release on turbulent nonpremixed planar jet flames". Ph.D. Dissertation. The University of Texas at Austin.

Rehm, J., Clemens, N.T. 1999. "The large-scale turbulent structure of nonpremixed planar jet-flames". Combustion and Flame, **116:**615-626.

Rao, V.K., Brzustowski, T.A. 1982. "Tracer studies of jets and diffusion flames in cross-flow", Combustion Sci. and Tech. **27:**229-230.

Riccou, F.P., Spalding, D.B. 1961. "Measurements of entrainment by axisymmetrical turbulent jets". J. Fluid Mech., **11:**21-32.

Roshko, A. 1976. "Structure of turbulent shear flows: A new look". AIAA Journal, **14**(10):1349-1357.

Samimi, M., Lele, S.K. 1991. "Motion of particles with inertia in a compressible free shear layer". Phys. Fluids A **3** (8):1915-1923.

Savas, O., Gollahalli, S.R. 1986. "Flow structure in near-nozzle region of gas jet flames". AIAA Journal. **24**(7):1137-1140.

Savas, O., Huang, R.F., Gollahalli, S.R. 1997. "Structure of the flow field of a nonpremixed gas jet flame in cross-flow", J. Energy Resources Technology, **119:**137-144.

Schluter, J.U., Schonfeld, T. 2000. "LES of jets in cross flow and its application to a gas turbine burner", Flow, Turbulence and Combustion. **65:**177-203.

Smith, S.H., Mungal, M.G. 1998. "Mixing, structure and scaling of the jet in crossflow", J. Fluid Mechanics, **357:**83-122.

Su, L.K., Mungal, M.G. 2004. "Simultaneous measurements of scalar and velocity field evolution in turbulent crossflowing jets". J. Fluid Mechanics. **513:**1 - 45.

Sykes, R. I., Lewellen, W.S., Parker, S.F. 1986. "On the vorticity dynamics of a turbulent jet in a crossflow", J. Fluid Mechanics. **168:**393-413.

Tacina, K.M., Dahm, W.J.A. 2000. "Effects of heat release on turbulent shear flows. Part 1. A general equivalence principle for non-buoyant flows and its application to turbulent jet flames". J. Fluid Mechanics. **415:**23-44.

Takagi, T., Shin, H.D., Ishio, A. 1980. "Local laminarization in turbulent diffusion flames", Combustion and Flame, **37:**163-170.

Takagi, T., Shin, H.D., Ishio, A. 1981. "Properties of turbulence in turbulent diffusion flames", Combustion and Flame, **40:**121-140.

Thring, M.W., Newby, M.P. 1953. "Combustion length of enclosed turbulent jet flames". Forth Symposium (International) on Combustion, The Standing Committee on Combustion, pp. 789-796.

Tsue, M., Kadota, T., Kono, M. 2000. "Detailed measurements of the structure of a jet diffusion flame in a cross flow". Proceedings of the Combustion Institute, **28:**295-301.

Tsue, M., Kadota, T., Kono, M. 2002. "Temperature and velocity fluctuations of a jet diffusion flame in a cross-flow", Proceedings of the Combustion Institute, **29:**1937-1942.

Van Cruyningen, I. 1990. "Quantitative imaging of turbulent gaseous jets using planar laser-induced fluorescence", Ph.D. Dissertation, Stanford University, HTGL Report No. T-267

Yuan, L.L., Street, R.L., Ferziger, J.H. 1999. "Large-eddy simulations of a round jet in crossflow", J. Fluid Mechanics. **379:**71-104.

Vita

Isaac G. Boxx was born in Mt. Pleasant, Michigan on October 2, 1976, son of Jesse and Julia Boxx. He and his family moved to Australia in 1977, where he lived until 1995. Living on an isolated ranch in rural Australia, Isaac was home-schooled through most of elementary and high-school. In 1995, he was awarded a full scholarship to attend Princeton University. He graduated in 1999 with a Bachelor of Science in Engineering from the Department of Mechanical and Aerospace Engineering. In the fall of 1999, he began his studies at the University of Texas at Austin in pursuit of a doctoral degree in aerospace engineering. During his time at UT, he was employed as a research assistant, teaching assistant and laboratory development coordinator.

Permanent address: P.O. Box 687
Mudgee, NSW 2850
Australia

This dissertation was typed by the author.